Multi-scale model of a valve-regulated lead-acid battery with electromotive force characterization to investigate irreversible sulphation

Angelique Janse van Rensburg

20160135

Thesis submitted for the degree *Doctor Philosophiae*

in Computer and Electronic Engineering

at the Potchefstroom Campus of the North-West University

Promoter: Prof. G van Schoor

Co-promoter: Prof. PA van Vuuren

May 2016

SUMMARY

Valve-regulated lead-acid (VRLA) batteries are commonly used for energy storage because they are inexpensive and easy to use. Combined with an immobile electrolyte, a VRLA battery has almost no risk of an acid spill. The use of VRLA batteries is expected to grow even though, in renewable energy systems, more than a third fail prematurely due to incorrect or abusive operation. A major cause of premature capacity loss in lead-acid batteries is a damage mechanism called irreversible sulphation (IS). This damage mechanism occurs on a microscopic scale in the electrical double-layer (EDL) during unobservable processes. On the observable macroscopic scale, measurable quantities during operation are used to calculate the battery's state-of-charge (SOC). Charge controllers use the SOC in an attempt to avoid the well-known operating modes resulting in IS, yet many batteries still fail. An improved understanding between microscopic processes in the EDL and observed macroscopic phenomena is necessary. The primary research contribution of this study is a multi-scale electrochemical model of a VRLA battery with an immobile electrolyte and its analysis. The model's input parameters are subjected to elementary effects analysis and a reduced set of the most influential parameters are used in variance-based model sensitivity analysis. The time and complexity associated with parameter estimation are reduced by electromotive force (EMF) characterization. The EMF of the battery is characterized using an accurate concentration-based method presented in this thesis as a secondary contribution. The validated multi-scale model is then used to simulate an operating mode that leads to IS while changes in the active surface area of the electrodes are observed. It was found that the available active surface area suffers irreversible decreases due to minor errors in SOC indication. Additionally, the internal resistance during the initial voltage drop increases from one discharge to the next. It was concluded that IS cannot be prevented satisfactorily using SOC information because SOC is not indicative of a specific damage mechanism. The curve of EMF versus electrolyte concentration resulting from EMF characterization is more descriptive of the battery's internal state than the SOC. Future work should include the development and application of a health-conscious charge control algorithm using the EMF curve because it requires very basic measurement data. With a thorough understanding of premature failure due to irreversible sulphation in VRLA batteries, charge controllers can be improved. This will ensure that the end-user has no opportunity for incorrect or abusive operation of the battery. Contributions to the mature field of lead-acid batteries are, in essence, advances in energy storage technology. As such, this study is part of a global effort towards a sustainable energy future.

Keywords: valve-regulated lead-acid battery, irreversible sulphation, state-of-charge, multi-scale model, parametric analysis, electromotive force characterization

This thesis is dedicated to my aunt, Esmé Combrinck.

But still try, for who knows what is possible...

- Michael Faraday, with whom I share the birthday of 22 September.

ACKNOWLEDGEMENTS

I would like to thank God for blessing me throughout my entire life with opportunity and ability. A doctoral study is a solitary journey and I believe that certain individuals were hand-picked to enrich my experience.

I am humbled by the support and understanding from my husband, Jan. He is more than I ever could have hoped for in a spouse and I would not have survived those last few months without him.

My sincerest gratitude to my promoters, Prof. George van Schoor and Prof. Pieter van Vuuren, for their patience and encouragement during my doctoral study. They gave me the freedom to explore my own ideas and the necessary guidance to improve on those ideas.

A special thank-you to my parents and the rest of my family – even with no expertise in the subject matter, they supported me with enthusiasm.

All my friends at the office, many of which were fellow postgraduate students, also deserve my gratitude. I truly appreciated the general companionship which included numerous coffee-break discussions and, sometimes, a minor remark that could spark a major breakthrough.

I would also like to thank my friends outside of the office for periodically dragging me away from my computer and reminding me that life is about so much more than work.

My appreciation to Prof. Dr.-Ing. Klaus-Dieter Haim at the Hochschule Zittau/Görlitz in Germany for his part in the success of my experimental work.

I would also like to thank *HySA Infrastructure* for their financial support over the past five years.

CONTENTS

LIST OF FIGURES

LIST OF TABLES

LIST OF SYMBOLS

Symbol	*Description*	*Unit*
$\mathbf{A},\mathbf{B}$	Left and right part of a matrix **M** with quasi-random numbers	
$\mathbf{A}_{\mathbf{B}}^{(i)}$	Matrix with all columns from **A** except the *i*-th column which is from **B**	
a_{ji}, b_{ji}	Elements in *j*-th rows and *i*-th columns of matrices **A** and **B**	
$a_{\max}$	Maximum active surface area	$\mathrm{cm}^2/\mathrm{cm}^3$
$\mathbf{B}^*$	Orientation matrix in Morris method with size $(k+1)\times k$	
C_{dl}	Double-layer capacitance	$\mathrm{F/cm}^2$
c_{ref}	Reference concentration	$\mathrm{mol/cm}^3$
D	Acid diffusion coefficient	cm^2/s
d_i	Elementary effect of input parameter *i*	
E_{A}	Activation energy	J/mol
$\mathrm{E}_{X_i}(\cdot)$	Mean of argument taken over X_i	
$\mathrm{E}_{\mathbf{X}_{\sim i}}(\cdot)$	Mean of argument taken over all parameters but X_i	
$\mathbf{e}_i$	Vector of zeros except for *i*-th componen, which is 1	
ex	Tortuosity correction in liquid phase	
exm	Tortuosity correction in solid phase	
h	Height of plate	mm
$i_{0,\mathrm{ref}}$	Transfer current density	$\mathrm{A/cm}^2$
k	Number of model input parameters, dimennsions of input space	
l	Width of region	mm
$\mathbf{M}$	Matrix of size $(N_{\mathrm{MC}}, 2k)$ used to obtain **A** and **B** in VBSA	
$\mathrm{MW}_{\mathrm{Pb}}$	Molecular weight of Pb	g/mol
$\mathrm{MW}_{\mathrm{PbO_2}}$	Molecular weight of $\mathrm{PbO_2}$	g/mol
$\mathrm{MW}_{\mathrm{PbSO_4}}$	Molecular weight of $\mathrm{PbSO_4}$	g/mol

Symbol	*Description*	*Unit*
N	Number of model evaluations	
N_{MC}	Number of Monte Carlo simulations	
N_{plates}	Total number of plates per cell	
n	Number of electrons involved	mol
p	Number of levels in Morris method	
r	Number of sample trajectories in Ω for Morris method	
S_i	First-order effect of parameter X_i in VBSA	
S_{Ti}	Total effect of parameter X_i in VBSA	
T_{ref}	Reference temperature (25 °C)	K
t_+^{o}	Transference number of H^+	
v	Cell voltage (V)	
$\bar{V}_{\mathrm{e}}$	Partial molar volume of $\mathrm{H_2SO_4}$	$\mathrm{cm^3/mol}$
$\bar{V}_{\mathrm{o}}$	Partial molar volume of $\mathrm{H_2O}$	$\mathrm{cm^3/mol}$
$\mathrm{var}_{X_i}(\cdot)$	Variance of argument taken over parameter X_i	
$\mathrm{var}_{\mathbf{X}_{\sim i}}(\cdot)$	Variance of argument taken over all parameters but X_i	
$\mathbf{X}$	Model input parameters with elements $X_1, X_2, \ldots, X_k$	
$\mathbf{X}_{\sim i}$	All input parameters except X_i	
X_i	Input parameter with *i* in the set $\{1, 2, \ldots, k\}$	
$\mathbf{x}$	Sample point of $\mathbf{X}$ with elements $x_1, x_2, \ldots, x_k$	
$\mathbf{x}^*$	Base value of $\mathbf{X}$ randomly sampled from Ω in Morris method	
$\mathbf{x}^{(l)}$	Random independent sample point *l* of $\mathbf{X}$ with elements $x_1, x_2, \ldots, x_k$	
x_i	Value of parameter X_i in the sample point $\mathbf{x}$	
w	Plate width	mm
α_{a}	Anodic transfer coefficient	
α_{c}	Cathodic transfer coefficient	
Δ	Constant step magnitude in Morris method	

Symbol	*Description*	*Unit*
ε_0	Porosity at zero charge	
$\varepsilon_{\max}$	Porosity at full charge	
$\varepsilon_{\mathrm{SEP}}$	Porosity of separator	
γ	Reaction order	
κ	Electrolyte conductivity	S/cm
μ	Mean of elementary effects of a single parameter, overall effect of parameter X_i	
μ^*	Absolute value of μ	
Ω	Region of experimentation, $\{0,1/(p-1),2/(p-1),\ldots,1\}$	
ρ_{Pb}	Density of Pb	g/cm^3
$\rho_{\mathrm{PbO_2}}$	Density of PbO_2	g/cm^3
$\rho_{\mathrm{PbSO_4}}$	Density of $PbSO_4$	g/cm^3
σ	Standard deviation of elementary effects of a single parameter	
σ_{M}	Conductivity of material M	S/cm
Υ	Model output of interest in VBSA	
ζ	Morphology parameter	

LIST OF ABBREVIATIONS

AGM	Absorbed glass mat
ANOVA	Analysis-of-variance
BMS	Battery management system
CC	Coulomb-counting
COV	Cut-off voltage
CV	Constant voltage
DOE	Department of Energy
EDL	Electrical double-layer
EEA	Elementary effects analysis
EES	Electrical energy storage
EIS	Electrochemical impedance spectroscopy
EMF	Electromotive force
EU	European Union
FEM	Finite element method
FTA	Fault tree analysis
GOF	Goodness-of-fit
IS	Irreversible sulphation
LAB	Lead-acid battery
MH	Macro-homogeneous
OCV	Open-circuit voltage
OFAT	One-Factor-At-a-Time
PDE	Partial differential equations
PSOC	Partial state-of-charge

QR	Quasi-random
RNL	Riso National Laboratory
SG	Specific gravity
SHE	Standard hydrogen electrode
SNL	Sandia National Laboratories
SOC	State-of-charge
VBSA	Variance-based sensitivity analysis
VRLA	Valve-regulated lead-acid

1 INTRODUCTION

The global energy crisis is one of the biggest challenges humankind has ever had to face. Efforts to solve this problem have to be made however and wherever possible – even on the smallest scale. Research objectives of this study include validating an electrochemical model of a valve-regulated lead-acid battery. This introductory chapter explains why research contributions to the relatively mature field of lead-acid battery technology are relevant to a sustainable energy future.

1.1 Energy storage systems

Our planet's global population and its energy demands are increasing at an alarming rate. Fossil fuel sources are concentrated in a restricted number of countries, which can make it difficult for other nations to ensure energy security. These issues and the associated environmental pollution are some of the driving factors behind research and development in sustainable energy technologies [1], [2].

Research in sustainable energy includes research in renewable energy (RE) systems. Renewable energy is said to originate from an inexhaustible source. Apart from being much cleaner than energy from fossil fuels, it is also considered to be globally available [3].

A key challenge in a RE system is the variable and intermittent nature of the energy source [1], [4]. The sun does not always shine and wind speed fluctuates. Load requirements might not always be met or grid stability can be compromised [5]. A reliable supply of energy can be ensured by integrating some means of energy storage into the RE system [6]. By choosing the most appropriate energy storage method and sizing it correctly for the application under consideration, backup energy can always be available [3].

In general, an energy source can only be deemed useful if the harvested energy is stored for later use. Selecting an energy storage system is no trivial matter – various factors as well as the intended application must be considered. Ibrahim, Ilinca and Perron [6] provide an in-depth review of the most prominent energy storage methods. These methods include, among others, compressed air, pumped hydro, fuel cells, flywheels, super-capacitors and batteries. The authors compare the different methods according to various characteristics such as capacity, reliability, efficiency, cost, availability and environmental impact [6].

Battery energy storage is well-known and easy to use when compared to other energy storage methods [5]. Batteries are capable of high energy densities and do not depend on geographic location. A battery can consist of a single cell or multiple cells which ensures availability in various sizes. As such, battery energy storage is currently the preferred energy storage method in renewable energy systems and electric vehicle technology [1], [3], [7]–[9].

Batteries are also used for backup power supply in telecommunications stations, electric utility centres and computer systems. Of the existing chemistries, the following are widely used in practice as rechargeable batteries: lead-acid, nickel-cadmium, nickel-metal-hydride and lithium-ion [2], [10].

1.2 Lead-acid battery technology

A lead-acid battery (LAB) is commonly known as a car battery and for good reason – every car uses one for starting, lighting and ignition purposes. Apart from this existing automotive market wherein consumers have to replace old batteries every few years, lead-acid battery technology is also a popular choice in other applications. These applications include backup power, motive power in forklift trucks and mining equipment, and renewable energy storage [2], [10]–[12].

With many alternatives in battery technology, there have to be additional reasons why the LAB industry accounts for almost 70% of secondary battery sales and generates vast amounts in annual revenue [2]. Lead-acid batteries are inexpensive and easy to recycle in comparison with other rechargeable battery types [13]. They have lower self-discharge rates than nickel- or lithium-based batteries and do not require overvoltage protection circuitry [14].

Valve-regulated lead-acid (VRLA) batteries are the most popular choice of LAB in a wide variety of applications because the risk of an acid spill is insignificant [14]. These features make LAB technology safe and readily available to the consumer.

The use of advanced VRLA batteries is only expected to increase [2], [15]. This upward trend is despite the fact that, in RE applications, more than a third of VRLA batteries fail prematurely due to incorrect or abusive operation [16], [17]. Having to replace the battery often amounts to unnecessary and high operating costs [18].

Figure 1-1 is a visual summary of the route followed to reach the focus on VRLA batteries. The figure clearly shows that research contributions in this area are, in essence, improvements to energy storage systems. To contribute within the focus of this study, it is necessary to investigate why so many VRLA batteries have a service life shorter than their intended design life.

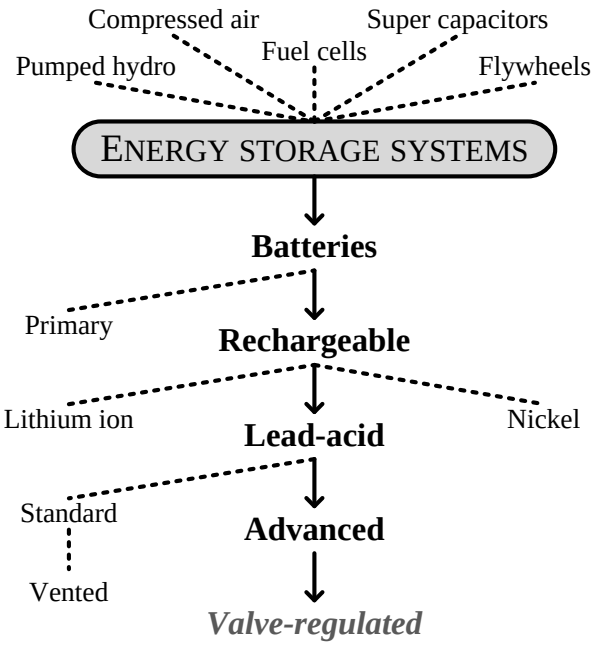

Figure 1-1: The focus of this study from an energy storage perspective

A lead-acid cell is an electrochemical energy source consisting of two lead-based electrodes immersed in an electrolyte, sulphuric acid (H_2SO_4). The positive terminal is attached to a porous lead-dioxide (PbO_2) plate whereas the negative terminal is attached to a spongy lead (Pb) plate. The cell is rechargeable which means that the discharge reaction can be reversed during the charging stage. A basic diagram of a single lead-acid cell is illustrated in Figure 1-2.

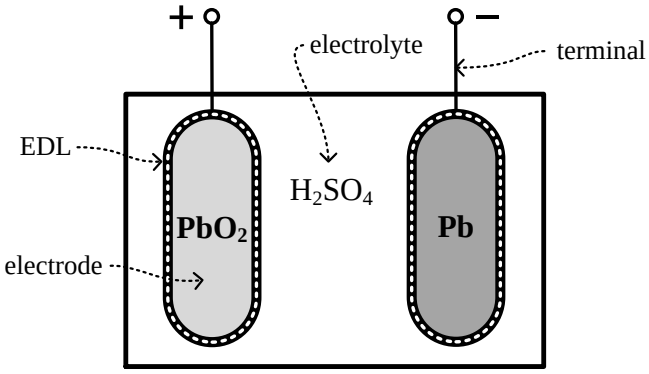

Figure 1-2: A basic diagram of a lead-acid cell with the electrical double layer (EDL)

The EDL region in Figure 1-2 is known as the electrical double-layer and represents the contact interface between the electrolyte and an electrode. This microscopic layer is responsible for complex processes which determine the cell's performance. The microscopic processes in the EDL include diffusion, crystallization and dissolution [10].

1.3 Damage mechanisms and battery failure

Battery damage occurs during microscopic processes whereas battery failure happens on a macroscopic scale. In this study, the term *multi-scale* refers to both the observable and unobservable realms of the lead-acid cell under investigation.

A premature decrease in capacity can occur with damage to either the electrodes or the electrolyte. A major contributor to premature capacity loss is irreversible sulphation. As such, it will be the damage mechanism under investigation in this study [13], [19]–[21]. Sulphation is a microscopic process in the EDL and it cannot be avoided because it is an inherent part of the lead-acid chemistry. Irreversible sulphation occurs when the lead-sulphate $(PbSO_4)$ crystals have time to harden and cannot be dissolved by subsequent charging. These crystals reduce the available active surface area of an electrode and decrease overall capacity [20].

Irreversible sulphation is an excellent example of an unobservable microscopic process with an observable macroscopic effect. Consider Figure 1-3 which visually explains this link between the macroscopic and microscopic scales. In the macroscopic realm on the left, the observable information during operation typically consists of measurable quantities such as voltage, current, temperature and time. These quantities are used to calculate the state-of-charge (SOC) and this SOC indicates available battery capacity.

Two modes of operation are illustrated by Figure 1-3 in green: long periods at a low SOC and cycling with a partial SOC (PSOC). These are the modes which cause irreversible sulphation and both depend on SOC indication [20]. It should be clear at this point that irreversible sulphation can be avoided by a battery management system (BMS) or a more simple charge controller with accurate SOC indication. Yet so many LABs still fail prematurely. Assuming a faultless controller, the suspicion shifts to the accuracy of SOC indication and its involvement in battery damage by irreversible sulphation.

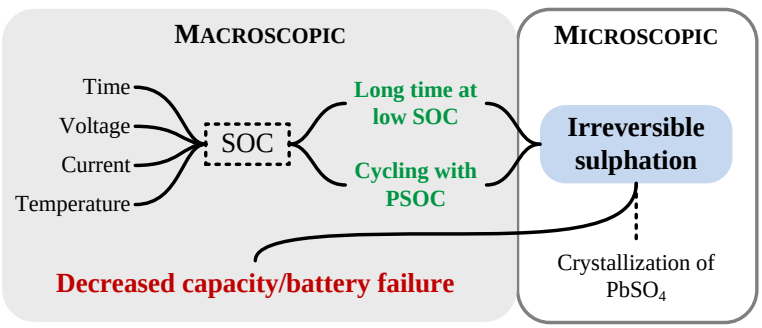

Figure 1-3: The link between microscopic processes and macroscopic effects used in this study

An improved understanding between microscopic processes in the EDL and observed macroscopic phenomena in lead-acid batteries seems necessary. The obvious route is to disassemble the battery and subject the electrodes to microscopic investigation. This is impractical for a VRLA battery because it has to remain sealed when in use for a realistic demonstration of its behaviour [22]. These difficulties might be why processes in the EDL remain active research areas [1], [23].

For these reasons, the nature of this study leans more toward a non-destructive investigation wherein the most information is collected from the observable realm. Modelling and simulation have long been the preferred tools used to understand complex systems and will also be used in this study [24]. [23]

1.4 Electrochemical modelling

The purpose of a mathematical battery model is to predict battery behaviour based on given information. Lead-acid battery models can be divided into three categories: electrochemical, equivalent circuit and stochastic. Electrochemical models are based on the physical processes inside the battery and usually include chemical, electrical and thermal characteristics. These models can be analytical or numerical depending on the application under consideration. Even though electrochemical models can be very complex, they are more accurate than any other modelling approach [25].

Electrochemical models of lead-acid cells are plentiful in literature, but only the most comprehensive versions are considered here. A comprehensive cell model typically simulates the current density, electric potentials and electrolyte concentration in both time and space. Changes in the porosity and active surface area of the electrodes are also included. Table 1-1 presents a summary of comprehensive modelling efforts in lead-acid battery technology. Features are listed in the first column and the model's source reference in the first row.

The letters D, E, M and C in Table 1-1 are used to indicate which terms are included in the model's material balance equation: D for diffusion, E for electrode reaction, M for migration and C for convection. Convection in the electrolyte of the separator depends on ion velocity and is a phenomenon which most models of a vented LAB include [26]. An electrochemical model of a VRLA battery with an immobile electrolyte that includes convection in the separator's electrolyte has not been found in the relevant literature. As such, mass transport by convection in the separator electrolyte of a VRLA battery is included in Table 1-1 using the following label: C *in separator if VRLA*.

The two features *Constant temperature* and *Varying temperature* are used to distinguish between models that regard the cell as isothermal and those that take temperature effects into account. An isothermal model can still account for a temperature different to a reference temperature but the temperature is considered to be constant over time.

Table 1-1: A comparison between comprehensive electrochemical models of a lead-acid battery

		[27]	[28]	[29]	[30]	[26]	[31]	[32]	[33]	[34]	[35]	[36]	[37]	[38]	[39]	[40]	[41]	[42]	[43]	[44]
Electrodes	D*, E		✓	✓																✓
	D, E, M	✓						✓	✓	✓	✓	✓		✓	✓	✓	✓	✓	✓	
	D, E, M, C				✓	✓	✓						✓							
Separator	D	✓	✓	✓	✓			✓	✓	✓	✓	✓	✓	✓	✓	✓	✓	✓	✓	✓
	D, C					✓	✓													
C *in separator if VRLA*																				
VRLA		✓	✓		✓			✓	✓	✓	✓		✓	✓	✓	✓	✓	✓	✓	
Electrical double-layer		✓			✓	✓					✓									
Constant temperature		✓	✓	✓	✓	✓	✓	✓	✓	✓	✓	✓		✓	✓		✓	✓		✓
Varying temperature													✓			✓			✓	
Gases		✓						✓	✓		✓		✓	✓			✓		✓	
Irreversible sulphation																	✓			
Corrosion				✓			✓													
Validated		✓	✓	✓	✓	✓**		✓	✓	✓	✓			✓	✓	✓	✓	✓	✓	✓

*** D – diffusion, E – electrode reaction, M – migration, C – convection**

**** A grey check mark indicates if a model feature is uncertain or partial inclusion of that feature.**

The *Gases* feature is used to indicate models that account for gas evolution and/or recombination in some way. VRLA designs with an immobile electrolyte have less risk of acid stratification and water loss than corrosion and sulphation [45]. As such, the battery damage mechanisms of corrosion and sulphation are included in Table 1-1. Finally, the *Validated* feature considers models that have been validated for, at least, a single discharge rate using experimental data.

A lead-acid battery is a complex nonlinear coupled system. It is understandable that no model yet includes every aspect of its behaviour. Many existing models suffer from oversimplifying assumptions such as a constant environmental temperature or a standard electrolyte. A serious lack of modelling for short and long term operation can also be observed from the relevant literature.

Previous electrochemical models, even some of the most comprehensive efforts, are not validated with experimental data from a realistic range of operating conditions. The selection of appropriate values for some model input parameters – a step required for experimental validation – is an ill-defined procedure fraught with difficulty [42]. Without some sort of guarantee in the model's accuracy usually obtained from the validation step, reliable conclusions cannot be made from the behaviour predicted by it [46].

1.5 Research problem

Even though LAB technology is the most mature battery technology, it continues to present substantial challenges [47]. The aim of this study, in a general sense, is to explore the relationship between macroscopic quantities and microscopic processes in the EDL and how they affect overall battery health.

It is well-known how to avoid irreversible sulphation but this damage mechanism remains a chronic challenge. It is entirely possible that the SOC cannot be used to avoid irreversible sulphation simply because it is incapable of providing detailed information on the condition of the electrode surfaces.

The objective of this study is to develop and validate a multi-scale electrochemical model of a VRLA battery with which to simulate electrode surfaces and modes of operation contributing to irreversible sulphation. This model will then be used to investigate the usefulness of SOC indication in preventing irreversible sulphation.

1.6 Methodology

The research methodology of this study is presented in Figure 1-4 along with each step's associated thesis chapter. The steps of the methodology are labelled A to D in the order of their execution. Step A of this study will consist of developing a multi-scale electrochemical model of a VRLA battery. The macroscopic treatment of a porous electrode, wherein variables are considered as volume-averaged quantities over a specified domain, will be used.

Step B will consist of collecting all the available information from VRLA batteries in operation. Multiple batteries will be charged and discharged repeatedly using different rates while sampling the terminal voltage, current and temperature. Since the ability of the SOC as an indication of a battery's internal condition is being questioned in this study, the electromotive force (EMF) will be used as an alternative [48]. With the experimental data at hand, the EMF will be characterized using a concentration-based method to obtain a curve of EMF against estimated molality.

The results from steps A and B will be used in step C during a parametric analysis of the multi-scale model. The characterized EMF curve will be used to fix concentration-dependent model input parameters.

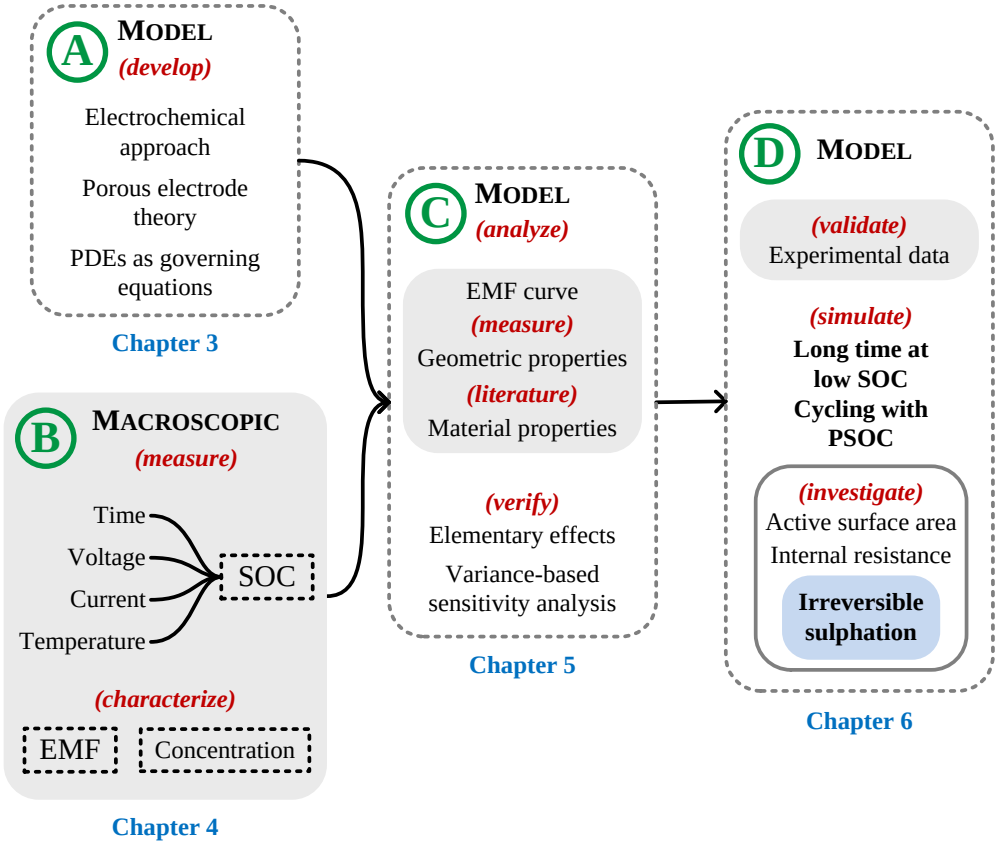

Figure 1-4: Research methodology and associated thesis chapters

Readily available geometric and material properties will be used for an elementary effects analysis of the model input parameters. The parametric analysis will conclude with a variance-based sensitivity analysis using the most influential model input parameters. Step D will start with experimental validation of the multi-scale model from step A. The modes of operation which cause irreversible sulphation will then be simulated using the validated model. The simulation results of electrode active surface area and internal resistance will be used to investigate irreversible sulphation.

1.7 Contributions

The main contribution of this study is a multi-scale electrochemical model of a VRLA battery and its analysis. The secondary contributions include:

- An improved EMF characterization method for lead-acid batteries.
- Quantitative sensitivity results of the parameters defining electrode kinetics.
- New insights into battery damage by irreversible sulphation.

These contributions can be used to ensure that the end-user has no opportunity for incorrect or abusive operation of the battery. With an improved understanding of the complex microscopic processes occurring inside a lead-acid cell, new battery designs with higher energy densities might be possible.

1.8 Thesis overview

Chapter 2: Literature review

The fundamental principles of lead-acid battery technology are presented in this chapter. A fault tree analysis (FTA) of battery damage mechanisms is presented and irreversible sulphation explained. The relationship between state-of-charge (SOC) and electromotive force (EMF) is discussed in detail. The chapter concludes with an overview of electrochemical modelling.

Chapter 3: Multi-scale electrochemical model of a lead-acid battery

This chapter starts with an overview of the approach used to develop a multi-scale model of a lead-acid battery. The fundamental principles are discussed and the governing equations for charge, discharge and rest are explained. The boundary conditions for a lead-acid cell are also presented and the choice of reference electrode for the overpotential is explained. A discussion of the improvements on previous modelling efforts concludes the chapter.

Chapter 4: Electromotive force characterization of a lead-acid cell

A brief overview of the existing methods for electromotive force (EMF) characterization starts this chapter. The inspiration behind an alternative concentration-based method is presented and its implementation is explained. The proposed method for EMF characterization is applied to experimental data from VRLA cells and its performance is compared to existing methods. The validation results indicate a significant improvement in accuracy and applicability over linear interpolation and linear extrapolation. As such, the concentration-based method for EMF characterization presented here is a secondary contribution of this study. The end result is a curve of the lead-acid cell's EMF against estimated electrolyte molality.

Chapter 5: Parametric analysis of the multi-scale model

The multi-scale model's input parameters are subjected to analysis in this chapter. The initial set of parameters is discussed and details of the numerical solution are presented. The most uncertain parameters are used in elementary effects analysis by the Morris method to determine their rank in the multi-scale model. A final set of the most influential parameters is subjected to variance-based sensitivity analysis using a Monte Carlo experiment. Each parameter's first order and total sensitivity coefficients with respect to both the simulated cell voltage and the model error are obtained. The chapter is concluded with a summary of the qualitative and quantitative results that will be used for parameter estimation during model validation in the next chapter.

Chapter 6: Model validation and investigation of irreversible sulphation

This chapter starts by explaining how the multi-scale model from Chapter 3 was validated using the results from the parameteric analysis in Chapter 5 in combination with experimental data. With an acceptably validated model, the active surface area of the electrodes are simulated in partial state-of-charge (PSOC) conditions to investigate irreversible sulphation. The cell's internal resistance during the initial voltage drop from one discharge to the next is also used as an indicator of sulphation.

Chapter 7: Conclusions

This final chapter concludes with a summary of the findings from the various thesis chapters. The research contributions are explained and recommendations for future work are provided.

2 LITERATURE REVIEW

To appreciate the challenges associated with lead-acid battery technology, the fundamental principles of a lead-acid cell are presented first. A fault tree analysis (FTA) of battery damage mechanisms is discussed and irreversible sulphation explained. The relationship between state-of-charge (SOC) and electromotive force (EMF) is discussed in detail. The chapter concludes with a substantiation of electrochemical modelling and parametric analysis techniques.

2.1 A lead-acid cell

Lead-acid batteries are generally of two types: vented or valve-regulated. A vented LAB can be opened for maintenance, such as adding water. A valve-regulated LAB is sealed to ensure that no gases can escape but instead recombine to form water. These sealed batteries require very little maintenance but are more sensitive to high environmental temperatures when compared to vented designs.

Valve-regulated lead-acid (VRLA) batteries can have a liquid or an immobile electrolyte. An immobile electrolyte consists of an acid-soaked material as the separator between two electrodes. The separator is made of either gel or glass fibres – a so-called absorbed glass mat (AGM). A valve-regulated cell design with such an immobile electrolyte has almost no risk of an electrolyte spill, which makes it considerably safer than the conventional vented design [49].

Regardless of the cell design or type of electrolyte, the operating principles and main reactions remain the same and will be presented using a valve-regulated desing with an immobile electrolyte.

2.1.1 Basic operating principles

A lead-acid cell within a VRLA battery consists of two porous electrodes and a separator as shown in Figure 2-1. The electrodes are fabricated by mechanically pasting the active material onto lead grids. After curing, the plates are immersed in the electrolyte and the process of formation turns the positive electrode material into porous lead-dioxide (PbO_2) whereas the negative electrode material is turned into spongy Pb. The electrolyte is a sulphuric acid (H_2SO_4) solution [10].

The process of manufacturing a lead-acid battery, vented or sealed, is more complex than described in this thesis. Various considerations are involved during grid design, paste preparation and assembly. It is worth mentioning that the terminal polarity never changes, even though an electrode can be either anode or cathode depending on the direction of the electrons i.e. whether charging or discharging [50].

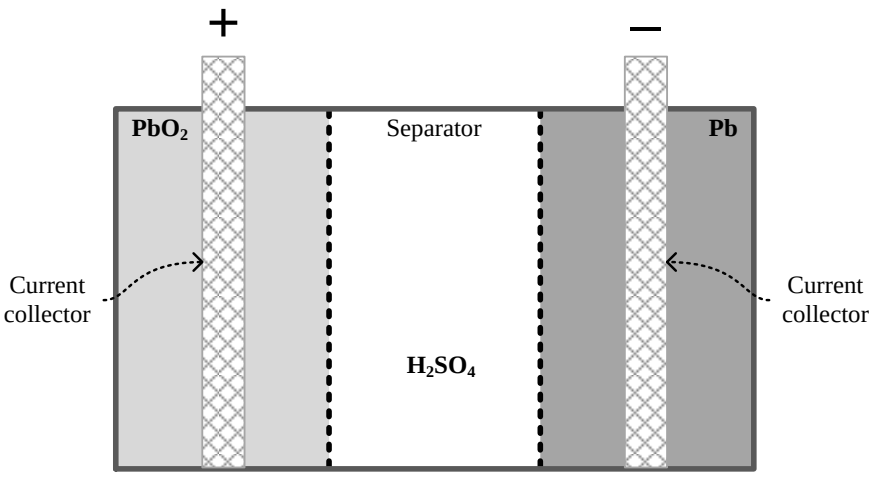

Figure 2-1: Illustration of a lead-acid cell with its separator sandwiched between two electrodes (in a VRLA battery with immobile electrolyte)

The cell can now be used to convert chemical energy and supply electrical energy according to typical reduction-oxidation (REDOX) reactions [50]. At the positive (PbO_2) electrode, the primary REDOX reaction is given by:

$$PbO_2(s) + HSO_4^-(aq) + 3H^+(aq) + 2e^- \underset{\text{charge}}{\overset{\text{discharge}}{\rightleftarrows}} PbSO_4(s) + 2H_2O(l) \tag{2.1}$$

The primary REDOX reaction at the negative (Pb) electrode is written as:

$$Pb(s) + HSO_4^-(aq) \underset{\text{charge}}{\overset{\text{discharge}}{\rightleftarrows}} PbSO_4(s) + H^+(aq) + 2e^- \tag{2.2}$$

During discharge, the electrons flow from the negative terminal to the positive terminal. The forward reaction in (2.1) explains how two electrons reduce lead from Pb^{4+} to Pb^{2+} and oxygen ions are released. The reduced lead ions bond with sulphate to form lead-sulphate ($PbSO_4$) at the cathode. Water is also produced because the oxygen ions bond with the hydrogen ions in the solution [10].

In the discharge reaction of (2.2), the charged hydrogen (H^+) and sulphate (SO_4^{2-}) ions have migrated toward the electrode due to diffusion or drift. Oxidized lead ions combine with sulphate ions and lead-sulphate precipitates on the lead surface. The anode's oxidation releases two electrons into the conductive band of the negative electrode [45].

The complete lead-acid cell reaction is the addition of the two half-cell reactions in (2.1) and (2.2) to result in:

$$Pb(s) + PbO_2(s) + 2H_2SO_4(aq) \underset{\text{charge}}{\overset{\text{discharge}}{\rightleftarrows}} 2PbSO_4(s) + 2H_2O(l) \tag{2.3}$$

The complete reaction shows clearly that lead-sulphate and water are produced while acid and electrode active materials are consumed during discharge. This overall reaction proceeds in the backward direction when a charging current is applied to the cell [10].

Electrons in the conductive band of an electrode flow in response to an electric field whereas ion movement in the electrolyte occurs due to three transport effects:

- Migration in response to an electric field.
- Diffusion due to concentration gradients in the electrolyte.
- Convection from bulk fluid motion, which can be natural or forced.

The electrochemical system in a lead-acid cell is considered thermodynamically unstable because its potential is higher than that of water electrolysis. When the cell is at open-circuit, self-discharge reactions proceed. The reactions have a natural tendency to proceed in the forward direction, though slowly, and discharge the cell [10].

In summary, electrochemical reactions involving electron transfer between electrode surfaces and ions from the electrolyte cause a potential difference between the two electrodes.

2.1.2 Electromotive force and electrolyte concentration

The electromotive force (EMF) of an electrochemical cell is an indication of the maximum work it can perform [51]. During discharge, the cell's free energy content changes with the EMF (E) according to:

$$\Delta G = -nFE \tag{2.4}$$

The number of electrons transferred is denoted by n with F the Faraday constant of 96,485 $\mathrm{C \cdot mol^{-1}}$ and the product (nF) is the quantity of electric charge transferred from anode to cathode.

With the standard convention of a positive sign for an increase in the energy of the surrounding environment, the maximum electric work $(w_{\max})$ that can be done by the cell is calculated as:

$$w_{\max} = nFE \tag{2.5}$$

This maximum work is the same as ΔG from (2.4) but with opposite sign [51].

The water produced during discharge dilutes the electrolyte and lowers the acid concentration and density. The different species of the electrolyte solution becomes less active and the cell's EMF decreases. The relationship between the cell's EMF and electrolyte concentration is expressed by the Nernst equation as:

$$E = E^{\circ} - \left(\frac{RT}{nF}\right)\ln Q \tag{2.6}$$

with $E°$ (V) the cell's potential in standard conditions, R the universal gas constant of 8.3144 $\mathrm{J}\cdot(\mathrm{mol}\cdot\mathrm{K})^{-1}$, T the absolute temperature in K and Q the reaction quotient [10]. The reaction quotient (Q) is a function of the different species concentrations given in [51] as:

$$Q = \frac{\overset{\text{product concentrations}}{[\mathrm{C}]^c[\mathrm{D}]^d}}{\underset{\text{reactant concentrations}}{[\mathrm{A}]^a[\mathrm{B}]^b}} \tag{2.7}$$

The species are denoted according to a typical REDOX reaction expressed as:

$$a\mathrm{A} + b\mathrm{B} \rightleftarrows c\mathrm{C} + d\mathrm{D} \tag{2.8}$$

The molar concentration of a species, $[\bullet]$ in (2.7), has units of $\mathrm{mol}\cdot\mathrm{L}^{-1}$ and differs from the molal concentration, with units of $\mathrm{mol}\cdot\mathrm{kg}^{-1}$. The molal concentration of a species is also known as its molality (m) and is related to the species acitivity (a_i) by $a_i = \gamma_i \cdot m$ with γ_i the activity coefficient of the relevant species [52].

For a lead-acid cell, the relationship between electrolyte molality and the ratio of species activities is shown in Figure 2-2 at a reference temperature of $T_{\mathrm{ref}} = 298.15\ \mathrm{K}\ (25\ °\mathrm{C})$. The values of the species activities that were used are the values reported for various molalities by Pavlov [10].

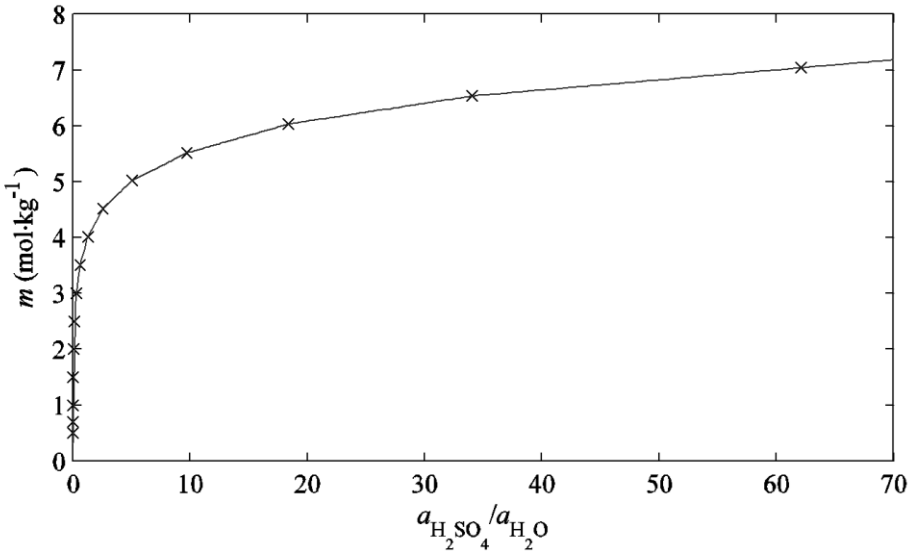

Figure 2-2: Reported electrolyte molality against the ratio of species activities at 25 °C

Without detailed information of the electrolyte concentration, the EMF of a cell can also be calculated when applying a current (I) using:

$$E = V - I \cdot R_{\mathrm{int}} \tag{2.9}$$

where V is the terminal voltage and R_{int} the cell's internal resistance. The applied current (I) is positive for charge and negative for discharge [50].

The voltage drop observed at the beginning of discharge differs in magnitude from one cycle to the next. Consecutive increases in this initial voltage drop is a sign of increasing internal resistance and is also considered an indication of irreversible sulphation [53].

The decrease in the energy content of the cell during discharge can be replaced by a subsequent charge because the lead-acid cell reaction is reversible. The cell's electrodes or electrolyte degrade during its lifetime and the available energy content decreases. How quickly the cell degrades and sustains permanent decreases in capacity depends on various stress factors and their associated damage mechanisms [21].

2.1.3 Fault-tree analysis of battery damage

An electrochemical cell completes a full cycle when it is discharged and then recharged. Battery lifetime is usually defined in terms of these cycles and depends mainly on how it is used. Degradation in a lead-acid battery can be described by several different damage mechanisms: corrosion of the positive grid, irreversible sulphation, water loss, active material degradation and electrolyte stratification [21].

A fault tree analysis (FTA) is used to relate stress factors, battery damage mechanisms and the associated decreases in capacity. Stress factors, due to incorrect or abusive operation, are of special interest when trying to maximise battery life [21]. Typical stress factors include high discharge rates, prolonged periods at a low SOC and partial cycling, and are quantities derived from the voltage, current and temperature history of the battery [49].

Consider Figure 2-3 which is the result of a fault tree analysis of decreases in capacity for a VRLA battery. Stress factors are indicated in grey text and may lead to secondary events, which are outlined with dashes. Damage mechanisms are also secondary events even though they are shaded in grey for emphasis. These secondary events eventually cause electrode and/or electrolyte damage which result in a permanent decrease in capacity [54]. If a battery's capacity decreases past a threshold specified by the manufacturer, it is called a battery failure.

Valve-regulated designs with an immobile electrolyte have minimal risk of water loss or electrolyte stratification. Corrosion usually occurs due to the presence of air inside the cell and since a VRLA battery is a sealed unit, this type of damage is easily prevented. Active material degradation is a natural process over the lifetime of a LAB in operation but can be accelerated by gassing [55].

As explained in Section 1.3, irreversible sulphation is a major contributor to premature capacity loss in lead-acid batteries [13], [19]–[21]. As such, it is the damage mechanism of interest in this study.

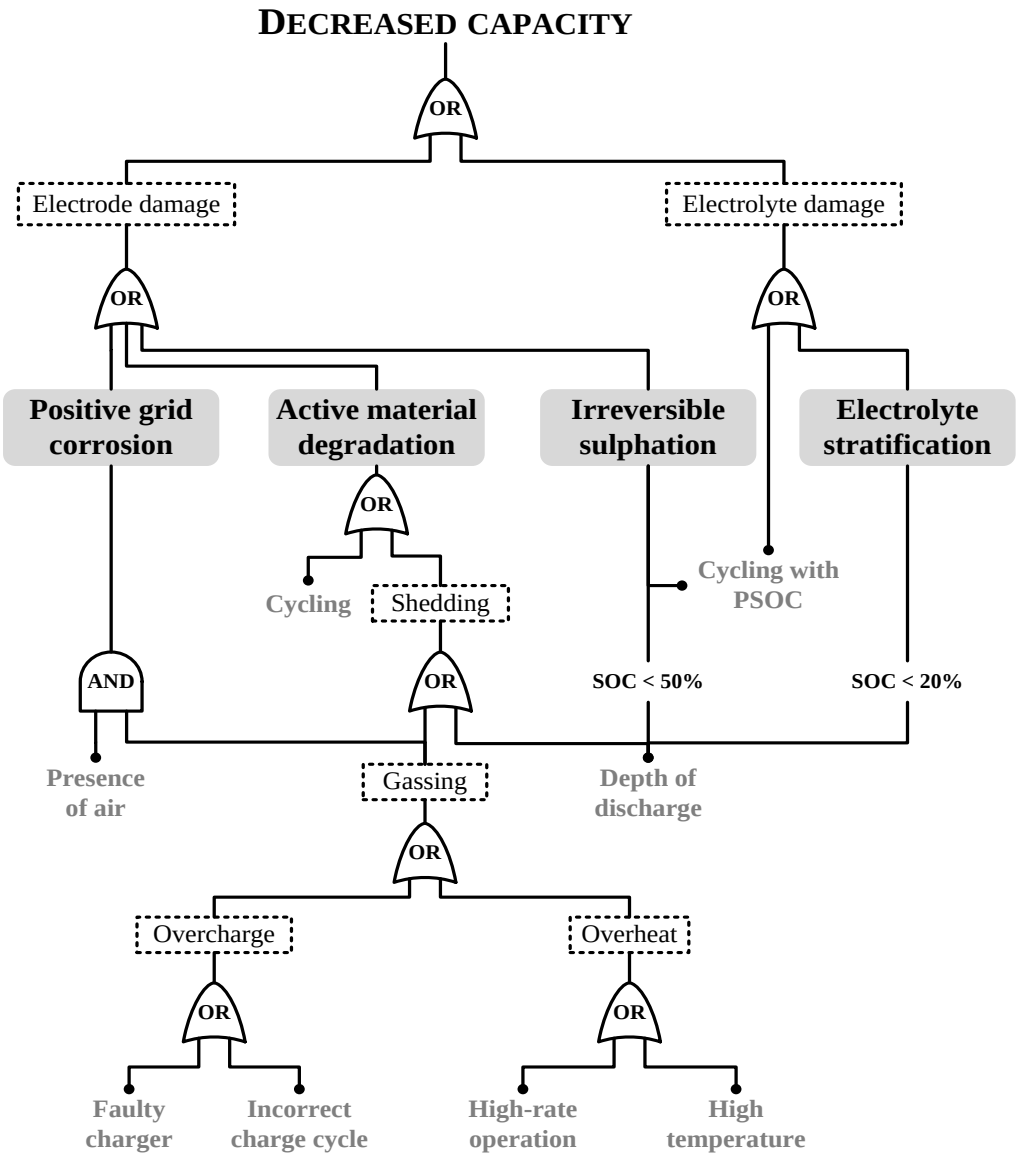

Figure 2-3: Fault tree analysis of decreased capacity in a VRLA battery

The resulting diagram from the FTA clearly shows that online SOC indication plays a major part in preventing irreversible sulphation. More specifically, prolonged periods at a low SOC and cycling with a PSOC should be avoided to prevent hardened sulphate crystals on the electrode surfaces [56].

2.1.4 Irreversible sulphation

Two complex systems are always at work in a lead-acid cell: the electrode system and the electrolyte system. Between these two systems, especially in the EDL, many different processes are happening at varying rates. It makes no matter whether the battery is charging, discharging or at rest – something is always happening in the EDL. These interfacial processes between the electrode and the electrolyte are still not completely understood and remain active research areas [1], [23].

Consider Figure 2-4 which depicts the microscopic processes at the contact interface between the electrode and the electrolyte during sulphation [57]. During discharge, Pb^{2+} ions are produced via electrolytic dissolution and react with sulphate ions during chemical crystallization to form $PbSO_4$ on the electrode's surface. These $PbSO_4$ crystals, if left to harden, are the cause of irreversible sulphation. The opposite occurs during charge wherein $PbSO_4$ dissolves via chemical dissolution into Pb^{2+} and sulphate ions. The Pb^{2+} ions are available for electrolytic crystallization whereas the sulphate ions diffuse back into the electrolyte [55].

A phenomenon worth mentioning is called Ostwald ripening. Initial $PbSO_4$ crystals have rough surfaces with high porosity which makes it easy for the electrolye to saturate the crystal layer. Some lead ions from these $PbSO_4$ crystals can dissolve and then recrystallize. The recrystallized $PbSO_4$ crystals have much finer surfaces with low porosity and the electrolyte cannot soak into the crystal layer as well as before. With a reaction area that has been reduced, these denser crystals are tough to dissolve during a subsequent charge [20].

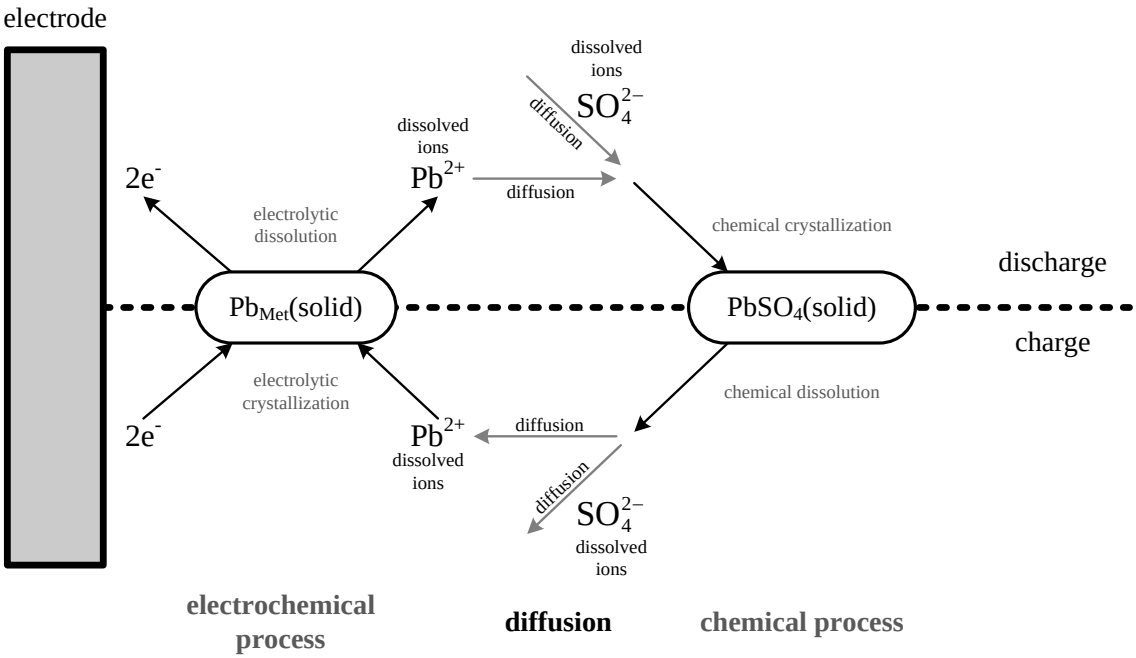

Figure 2-4: Microscopic processes in the EDL during sulphation in a lead-acid cell

The fundamental principles of lead-acid battery technology have now been presented and the reader is referred to the seminal text by Pavlov [10] for further information. If information specific to VRLA batteries is desired, the text by Rand, Moseley, Garche and Parker [45] can be consulted.

2.2 Battery capacity

In this study, the issue with state-of-charge (SOC) is not with the quantity itself but with its usefulness in preventing irreversible sulphation. A battery or cell's SOC is usually expressed as a percentage and can be a useful indication of remaining capacity. The standard practice for SOC calculation consists of summing the charge going in and coming out of the cell and dividing by the cell's rated capacity [48].

This calculation to obtain the SOC is known as Coulomb-counting (CC). At the start of discharge (t_0) the cell is full and the SOC at time instant t_d is given by:

$$\mathrm{SOC}(t_d) = 100\% + \frac{1}{Q_d}\int_{t_0}^{t_0+t_d} i_d(\tau)\,d\tau \tag{2.10}$$

where i_d is the applied discharge current and Q_d the available charge capacity. Similarly, the SOC during charge time instant t_c is calculated using:

$$\mathrm{SOC}(t_c) = 0\% + \frac{1}{Q_c}\int_{t_r}^{t_r+t_c} i_c(\tau)\,d\tau \tag{2.11}$$

where t_r is a time instant after a full discharge, i_c is the applied discharge current and Q_c the maximum capacity accepted by the cell during charge.

2.2.1 Challenges in SOC indication

When a discharge starts, Q_d is not known yet. The same holds true for Q_c at the beginning of a charge. These quantities are only available once the discharge or charge has ended. A battery management system (BMS) or charge controller faces significant difficulty to accurately determine the SOC without these two reference capacities. The rated capacity (Q_R) from the manufacturer's datasheet can be used for either Q_d or Q_c but serious errors result because the actual capacity changes over time [58].

The calculations in (2.10) and (2.11) contain integration operators which means that any error in the current measurement will be amplified [59]. Another issue is that of the energy lost to side reactions, such as gassing. Measurements would indicate that the current has gone into the cell but, in reality, it is not available for a subsequent discharge [58]. As a result, the SOC begins to drift over time. This error is sometimes accounted for by linking a charge efficiency to the SOC calculations as a reflection of charge acceptance [60].

To avoid drift complications and other errors, the SOC can be recalibrated periodically using open-circuit voltage (OCV) measurements [61]. This OCV is regarded as the cell's EMF under certain conditions and the EMF has an associated SOC that can be used to correct the estimated SOC [59].

An EMF curve depicting this EMF-SOC relationship can be obtained from the manufacturer's datasheet, but it does not account for variations in manufacturing [62]. The alternative is an initial offline characterization to obtain a more accurate approximation of the EMF-SOC relationship [59].

The advantage of an offline EMF characterization is that the quantities Q_d or Q_c are available for use in calculations of the SOC. Unfortunately, the resulting EMF-SOC curve will only be valid for a limited number of cycles because the cell's EMF also changes over the its lifetime. The EMF-SOC curve will therefore require updating or re-characterization to ensure continued accuracy.

It seems pertinent at this point to mention that no attempt is made to review the state-of-the-art in online SOC indication. The only aim here is to highlight general challenges with SOC calculation and their impact on the accuracy of the estimated SOC. As formulated in this study's research problem, the usefulness of the SOC in preventing irreversible sulphation is under investigation. Therefore, any significant inaccuracy in the SOC will render it impractical to avoid the operating modes that cause irreversible sulphation.

Since two cells with the same SOC can still have significantly different internal states, the SOC might not be indicative enough of a specific damage mechanism [63]. The challenges with SOC information, as presented thus far, motivated the search for an alternative quantity descriptive enough of a lead-acid cell's actual capacity.

2.2.2 Electromotive force characterization

The difference in potential energy of electrons at two electrodes results in the force required to move the electrons through the external circuit. This potential difference is the cell's EMF and is considered to be its internal driving force for electric work. As such, the EMF is of significant importance when the behaviour of the cell is under investigation and a characterization method is required.

An OCV measurement is taken as the cell's EMF if it was allowed to rest for a sufficiently long period. During this rest period, the measured voltage relaxes and converges towards the EMF [10]. The required rest period varies between chemistries and operating conditions, but it is usually in the order of several hours [64]. As a result, existing offline characterization methods are extremely time-consuming [59].

These existing methods for EMF characterization, which include voltage relaxation, linear interpolation and linear extrapolation, are explained and applied in Chapter 3 [48].

Another significant shortcoming of existing methods for EMF characterization is their result of an EMF curve versus SOC. The aim here is to move away from the SOC and use an alternative for capacity indication.

As explained earlier, a lead-acid cell's EMF changes with its electrolyte concentration. The concentration is used to calculate the electrolyte's specific gravity which is considered to be a reasonable indication of available capacity [58]. For this reason, Chapter 4 also explains the details of a concentration-based method for EMF characterization.

Regardless of the chosen method, the aim of EMF characterization remains the same: to obtain a curve, with the EMF on the *y*-axis, which represents the behaviour of a specific cell or battery. This characteristic curve can be especially useful in experimental model validation [65].

2.3 Modelling a lead-acid cell

The purpose of this section is to provide context to battery modelling and demonstrate the importance of further development in lead-acid battery models. Details regarding the multi-scale nature of the electrochemical model to be developed later, are also presented.

2.3.1 Research priorities for battery technology

The European Union (EU) led an international benchmarking project on hybrid energy systems in 2005. Part of this project was conducted by Riso National Laboratory (RNL) to investigate the lifetime modelling of lead-acid batteries [49]. Based on the findings of this project and the work of Sauer and Wenzl [66], researchers at the US Department of Energy (DOE) and Sandia National Laboratories (SNL) determined that battery energy modelling had to improve [67].

In 2007, the US DOE outlined the basic research needs for electrical energy storage (EES) in a report. In this report, priority research directions and cross-cutting issues were identified for battery energy storage. The following areas were identified as critical to meet future energy technology needs [1]:

- Microscopic processes which determine performance.
- Innovative design in electrodes and electrolytes.
- Improvements in theory and modelling.
- Increased energy density with stable electrode-electrolyte interface.

The US DOE and SNL also performed a study in 2009 on the current research status of energy storage and photovoltaic (PV) systems. They were convinced that advanced battery management will reduce costs and increase efficiency in PV energy systems [67].

The Commonwealth Scientific and Industrial Research Organisation (CSIRO) in Australia recently developed the UltraBattery by combining a lead-acid battery with a supercapacitor for fast charging applications. Gridtenital Energy, Inc. are actively working on advanced lead-acid batteries that make use of a silicon-based technology to replace the conventional metal grids.

Energy Power Systems (EPS) already sell an advanced lead-acid battery, called the PLM Battery, based on a proprietary technology and claims to offer more cycles at higher power than a standard AGM battery. It is clear that research and development in lead-acid battery technoglogy is ongoing and considered a priority by institutions around the world. In agreement with these findings, it makes sense to improve on our current understanding of the lead-acid battery's complex nature.

As mentioned earlier, modelling and simulation will be used in this study to investigate the internal processes of a lead-acid cell. The comparison between comprehensive electrochemical models of a lead-acid battery presented in Table 1-1 highlighted multiple areas for a research contribution. The conclusions from this comparison are as follow:

- Many models are oversimplified for computational efficiency therefore lack accuracy.
- Validated numerical models offer the best accuracy and insight into battery operation.
- Modelling of microscopic effects can improve our understanding of cell behaviour.
- A realistic model should include structural changes such as sulphation and corrosion.
- There is a serious lack of modelling for short and long term operation.
- Many models incorrectly assume isothermal conditions.

From the brief overview presented up to this point, it should be clear that there is definite opportunity for improvement in lead-acid battery modelling.

2.3.2 Types of battery models

Equivalent circuit models use electrical elements such as capacitors and resistors to represent different aspects of the battery. These models are much simpler than electrochemical models but also less accurate. To configure the circuit parameters, a considerable amount of experimental data is required making this a less attractive modelling approach. These parameters often lack physical meaning which complicates estimation of their initial values [25]. Since equivalent circuit models are generally empirical, little insight into the operation of the cell can be obtained [68].

Stochastic models rely on probability distributions in terms of parameters which represent physical properties of the battery. These models make use of fuzzy logic, neural networks and Markov chains and as such, are considered black-box models [69]. Stochastic models, like equivalent circuit models, lack the ability to provide a better understanding of the microscopic processes occurring inside an electrochemical cell [70].

Analytical electrochemical models are lumped-element models usually based on a thermodynamic approach. Mass transport, current distribution and electrode kinetics equations form the foundation of numerical electrochemical models, which are distributed-parameter models [52].

The electrochemical model type will be utilized in this study because the nonlinear processes in a lead-acid cell are governed by laws from various fields including electrochemistry, physics and corrosion science [10]. Furthermore, it is best to use a comprehensive model when the aim is to compare it with experimental tests over a broad range of operating conditions [33].

2.3.3 Macro-homogeneous approach

The macro-homogeneous (MH) approach is named as such because it considers the different regions of a cell as homogeneous on the macroscopic scale. In a one-dimensional application of the MH approach, the entities have distributed quantities in the direction perpendicular to the electrode grid. Volume-averaging is employed to obtain the distributed quantities, which are continuous in time and space [71].

The aim of the MH approach is to account for the significant features of a porous electrode without considering precise geometric detail. A representative volume element (REV) in an electrode consists of a solid matrix and electrolyte filling its pores. The REV is large with respect to the pore structure and small compared to the overall dimensions of the cell. This superposition of two continua, solid and solution, represent the active material of the porous electrode [72].

Electrochemical reactions are always heterogeneous [73]. It should be noted that even though the term *homogeneous* is used in the MH approach, it does not refer to an assumption about the reactions [74]. The MH approach still considers reactions at the electrode-electrolyte interface to be heterogeneous. To reduce this confusion, the MH approach is sometimes referred to as the macroscopic treatment of a porous electrode [52].

If the MH approach neglects precise geometric detail, can it account for microscopic phenomena? The active surface area between the electrode and electrolyte depends on electrode morphology and the dynamic behaviour of this contact interface [75]. As such, inclusion of the active surface area in a model based on the MH approach is vital to modelling the electrochemical reactions at the electrode-electrolyte interface. Detailed geometric information disregarded during the volume-averaging process is then restored according to Wang, Gu and Liaw [76]. Further partial differential equations describing electrode porosity variations add to the model's ability in simulating microscopic phenomena [77].

Since electrochemical phenomena take place over a wide range of length and time scales, a multi-scale approach was determined the most suitable to model a lead-acid cell in this study [78]. The MH approach, with the inclusion of active surface area and porosity components, ensures the coupling between the microscopic and macroscopic scales required for simulation of the electrode surfaces [79].

For detailed explanations of porous electrode theory, the reader is referred to the work by Newman and Tiedemann [80].

Details of concentrated electrolyte theory are reported by Onsager [81] and volume-averaging by Whitaker [82]. Recent modelling efforts based on the MH approach with microscopic considerations are by Esfahanian, Ansari and Torabi [83] as well as Ecker, Käbitz, Laresgoiti and Sauer [84].

The multi-scale electrochemical model used in this study is developed and explained in Chapter 3. The major challenge with a detailed electrochemical model resides in appropriate values for the large number of model input parameters [63].

2.4 Analysis of model input parameters

A significant part of experimental model validation consists of estimating input parameter values that result in a model output closely resembling the experimental data. It will be seen during the development of the multi-scale model in Chapter 3 that several input parameters appear in complex combinations with the model variables and each other.

Parameter estimation of models based on the MH approach is an ill-defined process mainly because it is extremely challenging. Values are recycled from literature, obtained from the manufacturer or measured if possible, or selected arbitrarily [32], [83], [85]. Using parameter values from previous research adds some uncertainty to the challenge because the values might have been determined for a different electrode composition or cell configuration. For this reason, parameter value estimation using experimental data from the cell or battery under investigation is necessary [37].

2.4.1 Input parameter screening

A significant number of model input parameters do not require estimation because their values are regarded as standard. The remaining parameters should be screened to determine those parameters that have the most substantial effect on the model output. The parameter set is then reduced by removing the insignificant parameters to obtain a subset for further analysis [86].

Most screening methods result in a qualitative impression of parameter importance rather than an exact quantification of the model's sensitivity to parameter values. Screening is a preliminary means of parameteric analysis with low computational cost because only a small number of model evaluations are necessary. The model output from these evaluations are processed using statistical calculations such as the mean and standard deviation [87].

Popular statistical methods for parameter screening include the One-Factor-At-a-Time (OFAT) design and elementary effects analysis with a Morris design. Of these two, the Morris method ensures the most complete exploration of the input space and will be used in Chapter 5 during parameteric analysis of the multi-scale model [88].

2.4.2 Model sensitivity analysis

Once a subset of the most influential input parameters has been obtained, it can be subjected to an in-depth analysis. The aim of model sensitivity analysis in this study is to obtain a quantitative description of parameter effects and their interaction. An added advantage of measuring the effects of parameters when they vary over their input range is that the model behaviour is also examined. Methods that achieve parameter effects analysis and examination of model behaviour are called variance-based sensitivity analysis (VBSA) methods [86].

A challenge associated with VBSA consists of sampling of the input parameter space to ensure that it is sufficiently explored using a reasonable number of model evaluations [89]. Sampling methods for sensitivity analysis include fixed sampling, Latin hypercube (LHS) sampling, quasi-random (QR) sampling and the method of Sobol' [90]. These methods are discussed in great detail by Saltelli, Tarantola, Campolongo and Ratto [87].

The model output over variation of the parameter values is then decomposed to analyze the sources of variance in the output. This decomposition is achieved by analysis-of-variance (ANOVA) methods and importance measures known as sensitivity indices are obtained for the input parameters. More specifically, each parameter's first-order and total sensitivity coefficients are calculated [91].

The results from VBSA can be used to determine the parameters that should be given priority above others during parameter estimation. Their first-order and total effects on the model prediction error can be calculated and used to examine why the model output differs from experimental data [87].

With a thorough understanding of the model's behaviour and input parameter effects, parameter estimation during model validation can be less challenging.

2.5 Conclusions

The literature review presented in this chapter provided context and substantiation to the research problem in Chapter 1. The challenges regarding lead-acid battery technology and capacity loss due to irreversible sulphation were discussed. The relationship between SOC, EMF and the electrolyte concentration was explained and an alternative method to avoid irreversible sulphation was motivated.

The chapter continued with a brief overview of lead-acid battery model types and approaches. The MH approach was demonstrated as suitable to develop a multi-scale electrochemical model for a lead-acid cell. The chapter concluded with details of parameter estimation for models based on the MH approach. Specifically, the lack of a thorough parameter estimation process was highlighted and statistical methods toward parametric analysis were discussed. Development of the multi-scale model that will be used later to investigate irreversible sulphation in a lead-acid battery, will now be presented.

3 MULTI-SCALE ELECTROCHEMICAL MODEL OF A LEAD-ACID BATTERY

This chapter starts with an overview of the approach used to develop a multi-scale model of a lead-acid battery. The fundamental principles are discussed and the governing equations for charge, discharge and rest are explained. The boundary conditions for a lead-acid cell are also presented and the choice of reference electrode for the overpotential is explained. A discussion of the improvements on previous modelling efforts concludes the chapter.

3.1 Unit cell

The complete reaction of a lead-acid cell is repeated here for ease of reference as:

$$Pb(s) + PbO_2(s) + 2H_2SO_4(aq) \underset{\text{charge}}{\overset{\text{discharge}}{\rightleftarrows}} 2PbSO_4(s) + 2H_2O(l) \tag{3.1}$$

with PbO_2 the positive electrode material and Pb the negative electrode material. The type of lead-acid battery considered in this study is a valve-regulated lead-acid (VRLA) battery composed of a single cell with an absorbed glass mat (AGM) separator. Consider Figure 3-1 which depicts the separator sandwiched between the electrodes as well as the grids of the current collectors. The current collectors feed the current to the battery's respective terminals.

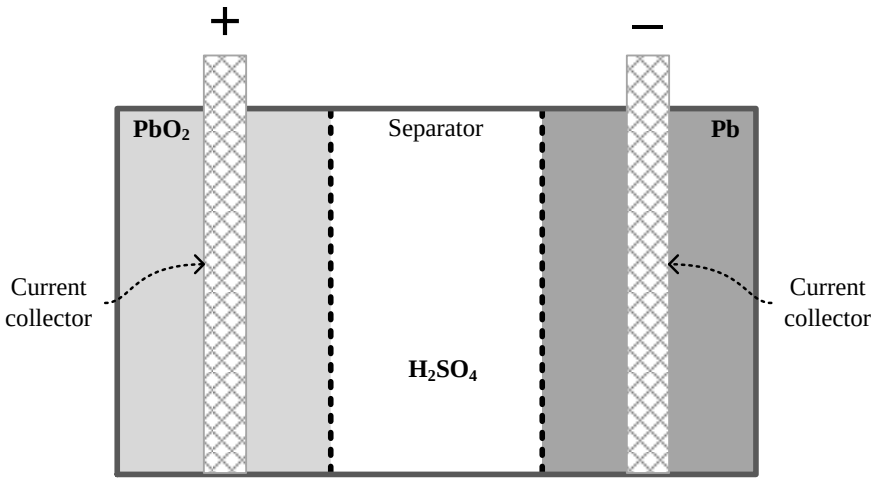

Figure 3-1: Illustration of a lead-acid cell with its separator sandwiched between the electrodes

The electrolyte, H_2SO_4, is contained in the separator which means that no isolated electrolyte reservoir is considered in this study. This exclusion is the accepted practice when modelling a LAB with an immobile electrolyte [34].

Consider now Figure 3-2 which contains the same sandwiched configuration of Figure 3-1 but with a unit cell indicated by an external boundary. The unit cell is named as such because it is the smallest repeatable unit within the electrochemical system of the lead-acid cell. It is typically repeated to form a stack of cells in an actual battery.

The current collectors are positioned in the centre of each electrode and enable a plane of symmetry in the electrodes. By exploiting symmetry within the lead-acid cell and considering only the unit cell during modelling, the model size as well as computational requirements are reduced.

The unit cell is composed of a positive electrode domain (d_1), a separator domain (d_2) and a negative electrode domain (d_3). The applied current density (i_{app}) in A/cm^2 is in the direction of the *x*-axis and perpendicular to the grids of the current collectors.

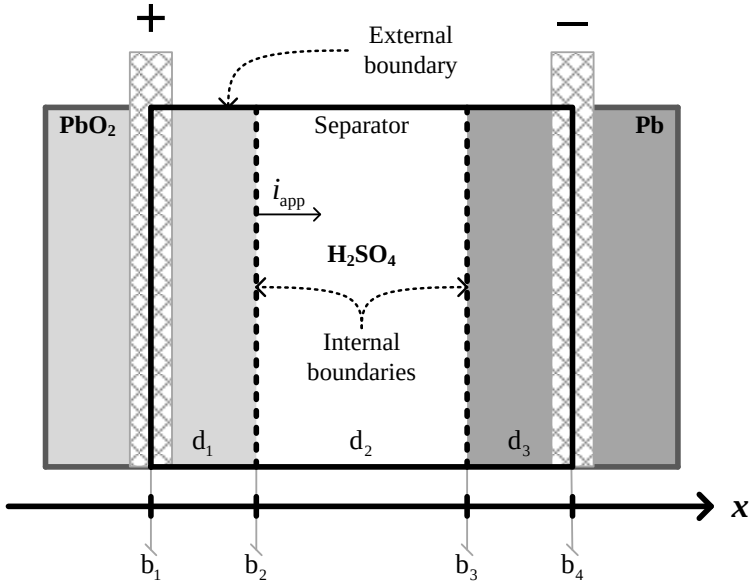

Figure 3-2: Illustration of the unit cell under consideration in 1D

The parts of the external boundary in parallel with the *x*-axis are not labelled because they only become relevant when modelling in more than a single dimension. The domains in the unit cell have internal and/or external boundaries.

The governing equations for each domain, which will be presented shortly, consist of partial differential equations (PDEs). As explained later, the sets of PDEs are solved using the finite element method (FEM) in COMSOL Multiphysics®.

The internal boundaries, b_2 and b_3, are situated at the electrode-electrolyte interfaces whereas b_1 and b_4 are situated at the centres of the electrodes as shown in Figure 3-3.

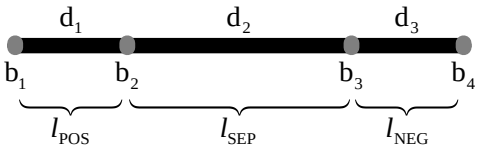

Figure 3-3: Illustration of the domains and boundaries in a single dimension

For a single dimension, each domain is represented by a line element and a boundary is represented by a point element in Figure 3-3. Adding the domain lengths results in the total length of the unit cell as $l_{\text{UNIT}} = l_{\text{POS}} + l_{\text{SEP}} + l_{\text{NEG}}$ in cm. The concept of a unit cell has now been defined and the focus shifts to the macroscopic treatment of a porous electrode.

3.2 Macroscopic treatment of a porous electrode

The macroscopic treatment of a porous electrode regards the electrode as a solid matrix with concentrated electrolyte filling the pores. The solid matrix includes non-conducting reactive materials and electrical conductors [52].

As shown in Figure 3-4, the pores of the positive electrode are filled with H_2SO_4 and the insulating $PbSO_4$ crystals are present at the electrode-electrolyte interface. The positive active material, PbO_2, is an electrical conductor. The pore-filling electrolyte is considered to be a binary electrolyte which dissociates fully into its respective ions, H^+ and HSO_4^- [80].

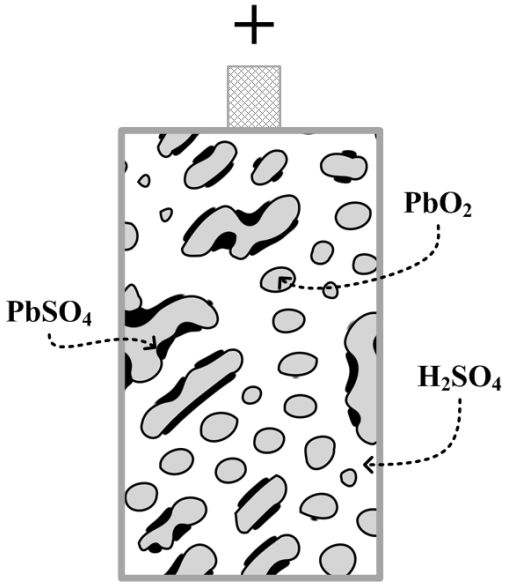

Figure 3-4: Illustration of the positive electrode with a pore-filling electrolyte and $PbSO_4$ layers

The different domains within the cell are taken to be homogeneous macroscopic entities with distributed quantities in the direction of the *x*-axis. The volume-averaged quantities are assumed to be continuous in both time and space. This macro-homogenous approach still considers the electrochemical reaction at the microscopic electrode-electrolyte interface to be heterogeneous [52]. For a full discussion of the multi-scale nature of the model developed in this chapter, refer to Section 2.3.3.

Throughout this thesis, *i* will be used to refer to current density in $\mathrm{A/cm^2}$ and *j* to current per unit volume in $\mathrm{A/cm^3}$. The variable I_{app} will simply be the applied current in A. Within the macroscopic treatment of a porous electrode, the solid matrix conducts a current with density i_1 and the pore-filling electrolyte a current with density of i_2.

Due to the assumption of electroneutrality between the phases within an electrode, a conservation of charge is applicable and given by:

$$\frac{\partial i_1}{\partial x} + \frac{\partial i_2}{\partial x} = 0 \tag{3.2}$$

All of the current is in the current collector at $\mathrm{b_1}$ and therefore, $i_2 = 0.$ At the first interface boundary, $\mathrm{b_2}$, all of the current is in the electrolyte because no active solid phase is present and $i_1 = 0.$ Either of these boundary conditions can be used to integrate (3.2) and results in:

$$i_{\mathrm{app}} = i_1 + i_2 \tag{3.3}$$

with i_{app} representing the applied current density referred to the projected electrode area denoted by A_{plate} $(\mathrm{cm^2})$. Equation (3.3) states that the sum of the current density in both the solid and liquid phases must equal the total current density in the unit cell. This conservation of charge is applicable at every location in the unit cell. With physical dimensions of the electrode plates, the applied current density can be calculated as: $i_{\mathrm{app}} = I_{\mathrm{app}} / (A_{\mathrm{plate}})$.

The solid matrix has an electric potential, ϕ_1, and the pore-filling electrolyte an electrolyte potential, ϕ_2. Each electrode has an associated porosity or void volume fraction of ε and the electrolyte has a concentration of c in $\mathrm{mol/cm^3}$. At this point in the model development, there are five unknown variables in each of the three domains: ε, c, ϕ_1, ϕ_2 and i_2 with the subscript 1 for the solid phase and the subscript 2 for the liquid phase.

Throughout this whole study, the cell is assumed to be a constant-volume closed system and the ambient temperature is allowed to vary.

The governing equations, which follow shortly, are based on derivations that are not repeated in this thesis simply because it would not be original work. These derivations are explained exceptionally well in the respective works of Newman and Thomas-Alyea [52] and Nguyen [92].

3.3 Stoichiometry in an electrochemical reaction

Newman's notation for an electrochemical reaction is used throughout the development of the multi-scale model presented in this thesis and is given as:

$$\sum_g s_g M_g^{z_g} \rightleftarrows ne^- \tag{3.4}$$

with s_g the stoichiometric coefficient of species *g*, M_g the chemical formula of species *g* with valence number z_g and *n* the number of electrons transferred during the reaction [52]. The species is given by $g = +, -, \text{o}$ for either cation, anion or solvent.

For the positive electrode reaction in (3.5), the coefficient values are listed in Table 3-1 according to the convention in (3.4).

$$\text{PbO}_2(\text{s}) + \text{HSO}_4^-(\text{aq}) + 3\text{H}^+(\text{aq}) + 2\text{e}^- \underset{\text{charge}}{\overset{\text{discharge}}{\rightleftarrows}} \text{PbSO}_4(\text{s}) + 2\text{H}_2\text{O}(\text{l}) \tag{3.5}$$

The coefficient values for the negative electrode reaction in (3.6) are also given in Table 3-1 using the convention in (3.4).

$$\text{Pb}(\text{s}) + \text{HSO}_4^-(\text{aq}) \underset{\text{charge}}{\overset{\text{discharge}}{\rightleftarrows}} \text{PbSO}_4(\text{s}) + \text{H}^+(\text{aq}) + 2\text{e}^- \tag{3.6}$$

Table 3-1: Stoichiometric coefficient values for the positive and negative electrode reactions

Positive electrode region, d_1	*Negative electrode region,* d_3
$s_{\text{PbO}_2(\text{s})} = -1$	$s_{\text{Pb(s)}} = +1$
$s_{\text{HSO}_4^-(\text{aq})} = -1$	$s_{\text{HSO}_4^-(\text{aq})} = +1$
$s_{\text{H}^+(\text{aq})} = -3$	$s_{\text{H}^+(\text{aq})} = -1$
$s_{\text{PbSO}_4(\text{s})} = +1$	$s_{\text{PbSO}_4(\text{s})} = -1$
$s_{\text{H}_2\text{O(l)}} = +2$	$n = +2$
$n = +2$	

3.4 Governing equations for the positive electrode, d_1

The governing equations for the positive electrode region is presented first but the equations of all three regions are based on the same principles and laws. These consist of material balance equations and Ohm's law applied to both the solid and liquid phases in each region as well as the concentration-dependent Butler-Volmer equation for electrode kinetics.

The region under consideration for the electrochemical reaction at the positive electrode given in (3.5), is depicted in Figure 3-5. The domains and boundaries are the same as explained in the previous section. Take note of the direction of the applied current density i_{app} – it is the same throughout the rest of the unit cell.

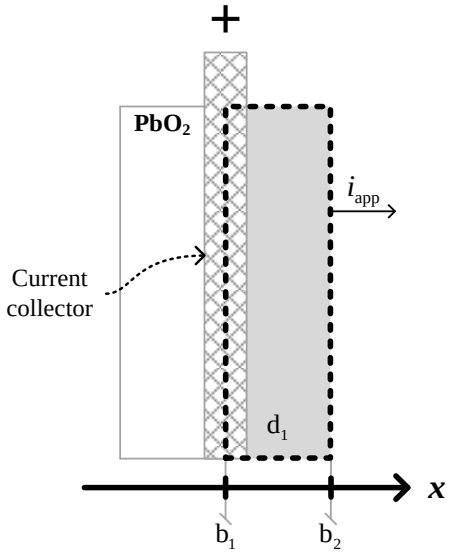

Figure 3-5: Region of the positive electrode referred to as d_1 in the multi-scale model

3.4.1 Porosity variation in an electrode

Porosity variation in an electrode with *k* solid species is given by the material balance equation as:

$$\frac{\partial \varepsilon}{\partial t} = \frac{1}{nF} \sum_{k}^{\text{solid species}} \left(\frac{s_k \text{Mw}_k}{\rho_k} \right) j \tag{3.7}$$

with *n* the number of electrons involved in the reaction, *F* the Faraday constant of 96,485 $(\text{A} \cdot \text{s})/\text{mol}$, Mw_k the molecular weight of solid species *k* in g/mol and ρ_k the density in g/cm^3 of solid species *k*. The reaction current per unit volume of electrode is represented by j in A/cm^3. Equation (3.7) is a direct application of Faraday's first law of electrolysis for material changes in a volume element [80].

Taking into account the conservation of charge equation in (3.2), the electrode reaction current is responsible for the current density in either the solid or liquid phases according to:

$$j = \frac{\partial i_2}{\partial x} = -\frac{\partial i_1}{\partial x} \tag{3.8}$$

For the discharge reaction of the positive electrode in (3.5), the porosity decreases as PbO_2 is converted to $PbSO_4$. The sulphate crystals form an insulating layer decreasing the available active surface area.

Substituting the stoichiometry coefficients for PbO_2 and $PbSO_4$ from Table 3-1 into (3.7), this porosity variation over time is given by:

$$\frac{\partial \varepsilon}{\partial t} - \frac{1}{nF}\left(\frac{\mathrm{Mw}_{\mathrm{PbSO_4}}}{\rho_{\mathrm{PbSO_4}}} - \frac{\mathrm{Mw}_{\mathrm{PbO_2}}}{\rho_{\mathrm{PbO_2}}}\right)\frac{\partial i_2}{\partial x} = 0 \tag{3.9}$$

The partial molar volume $\bar{V}_k$ of a species *k* in $\mathrm{cm}^3/\mathrm{mol}$ is given by:

$$\bar{V}_k = \frac{\mathrm{Mw}_k}{\rho_k} \tag{3.10}$$

Using this formula in (3.9), the porosity variation over time then becomes:

$$\frac{\partial \varepsilon}{\partial t} = \frac{\bar{V}_{\mathrm{PbSO_4}}}{nF}\cdot\frac{\partial i_2}{\partial x} - \frac{\bar{V}_{\mathrm{PbO_2}}}{nF}\cdot\frac{\partial i_2}{\partial x} \tag{3.11}$$

The volume PbO_2 that reacted at the electrode is replaced by the volume of $PbSO_4$ produced at the electrode. The sulphate crystals effectively plug the pores in the electrode and the electrode capacity decreases as discharge proceeds.

The rate of the reaction is directly proportional to the current density in the pore-filling electrolyte (i_2) and will be explained later using the Butler-Volmer equation for electrode kinetics.

3.4.2 Ohm's law in a solid

For a porous electrode with conductivity of σ in S/cm, Ohm's law gives the current density in the solid matrix due to the flow of electrons in response to an electric potential gradient as:

$$i_1 = -\varepsilon^{\mathrm{exm}}\sigma\frac{\partial \phi_1}{\partial x} \tag{3.12}$$

with exm a correction factor for tortuosity in the solid phase. Substituting (3.12) into (3.3) results in:

$$i_2 - \varepsilon^{\mathrm{exm1}}\sigma_{\mathrm{PbO_2}}\frac{\partial \phi_1}{\partial x} = i_{\mathrm{app}} \tag{3.13}$$

with exm1 the correction factor in the solid phase of d_1 and $\sigma_{\mathrm{PbO_2}}$ the conductivity of PbO_2.

3.4.3 Ohm's law in a solution

The current in an electrolyte is driven by electric and chemical potential gradients according to:

$$\frac{i_2}{\kappa^{\mathrm{eff}}} = -\frac{\partial \phi_2}{\partial x} - \frac{1}{F}\left(\frac{s_+}{\nu_+ n} + \frac{t_+^{\mathrm{o}}}{\nu_+ z_+} - \frac{s_{\mathrm{o}} c}{n c_{\mathrm{o}}}\right)\frac{\partial \mu_e}{\partial x} \tag{3.14}$$

with κ^{eff} the effective electrolyte conductivity, t_+^{o} the transference number of the cations (H^+) and μ_e the electrochemical potential of the electrolyte.

The stoichiometric coefficients (s_g) have $g = +, -, \mathrm{o}$ for either cation, anion or solvent. The solvent (H_2O) has a concentration of c_o in mol/cm^3 with the number of dissociated cations as v_+ and the number of dissociated anions (HSO_4^-) as v_- [92].

In (3.14), the effective electrolyte conductivity is given by $\kappa^{\mathrm{eff}} = \varepsilon^{\mathrm{ex}}\kappa$ where ex is a correction factor for tortuosity in the liquid phase and κ the electrolyte conductivity in S/cm.

Employing the relationship between the solvent and electrolyte concentrations and the definition of electrochemical potential as done in [92], (3.14) becomes:

$$\frac{i_2}{\varepsilon^{\mathrm{ex1}}\kappa} + \frac{\partial \phi_2}{\partial x} - \frac{RT}{F}\left(1 - 2t_+^{\mathrm{o}}\right)\frac{\partial \ln c}{\partial x} = 0 \tag{3.15}$$

with the coefficient values for the positive electrode reaction from Table 3-1. A correction factor for tortuosity in the liquid phase of d_1 is denoted by ex1. The universal gas constant of 8.3143 J/(mol·K) is denoted by *R* and the temperature in K by *T*.

The electrolyte conductivity (κ) is related to the acid concentration and temperature using:

$$\begin{aligned} &\kappa = c \cdot \exp(b), \\ &b = 1.1104 + 199.475c - 16{,}097.781c^2 + \frac{3916.95 - 99{,}406c - (712{,}860/T)}{T} \end{aligned} \tag{3.16}$$

with c in mol/cm^3 [34].

3.4.4 Material balance for the electrolyte

Using average quantities, a material balance for species *g* in the electrolyte is given by:

$$\frac{\partial(\varepsilon c_g)}{\partial t} = -\frac{\partial N_{x,g}}{\partial x} + R_g, \qquad R_g = -\frac{s_g}{nF} j \tag{3.17}$$

with $g = +, -, \mathrm{o}$ for either cation, anion or solvent. The molar flux in the *x*-axis direction of species *g* is represented by $N_{x,g}$ and the production rate of species *g* by R_g. The electrode reaction current per unit volume is denoted by *j* as defined in (3.8). The electrolyte's dissociated ions can be transported due to convection, migration and diffusion with the molar flux in the *x*-axis direction written as:

$$N_{x,g} = \underbrace{c_g v^*}_{\text{convection}} \underbrace{-D\frac{\partial c_g}{\partial x}}_{\text{diffusion}} \underbrace{+\frac{t_g^{\mathrm{o}}}{z_g F} i_2}_{\text{migration}}, \qquad g = +, - \tag{3.18}$$

with v^* the volume-averaged velocity in cm/s, c_g the species concentration in mol/cm^3 and *D* the diffusion coefficient of the electrolyte in cm^2/s. The migration term in (3.18) is zero when $g = \mathrm{o}$ for the solvent [93].

The derivation for the volume-averaged velocity (v^*) relies on the conservation of volume [94]. For an electrode soaked with electrolyte, the equation for porosity variation from (3.7) is used to obtain:

$$v^* = -\frac{1}{nF}\left(\frac{s_+\bar{V}_e}{\nu_+} + \frac{nt_+^{\mathrm{o}}\bar{V}_e}{\nu_+ z_+} + s_{\mathrm{o}}\bar{V}_{\mathrm{o}} + \sum_k^{\text{solid species}} \frac{s_k M_k}{\rho_k}\right) i_2 \tag{3.19}$$

Eq. (3.17) results in three equations that are reduced to a single equation, as done in [92], to yield:

$$\varepsilon\frac{\partial c}{\partial t} + v^*\frac{\partial c}{\partial x} = \frac{\partial}{\partial x}\left(\varepsilon^{\mathrm{ex1}} D\frac{\partial c}{\partial x}\right) + \left[-\frac{s_+}{\nu_+ nF} - \frac{t_+^{\mathrm{o}}}{\nu_+ z_+ F} + \frac{c}{nF}\left(\frac{s_+\bar{V}_e}{\nu_+} + \frac{nt_+^{\mathrm{o}}\bar{V}_e}{\nu_+ z_+} + s_{\mathrm{o}}\bar{V}_{\mathrm{o}}\right)\right]\frac{\partial i_2}{\partial x} \tag{3.20}$$

with $j = \partial i_2 / \partial x$ from (3.8) also substituted into (3.17).

Substitution of v^* from (3.19) along with stoichiometric coefficients and valence numbers for d_1 from Table 3-1 into (3.20), yields the material balance for the electrolyte as:

$$\begin{aligned}\varepsilon\frac{\partial c}{\partial t} - \frac{1}{nF}\left[\left(\frac{\mathrm{Mw}_{\mathrm{PbSO_4}}}{\rho_{\mathrm{PbSO_4}}} - \frac{\mathrm{Mw}_{\mathrm{PbO_2}}}{\rho_{\mathrm{PbO_2}}}\right) + 2\bar{V}_{\mathrm{o}} - (3-2t_+^{\mathrm{o}})\bar{V}_e\right] i_2\frac{\partial c}{\partial x} - \\ \frac{\partial}{\partial x}\left(\varepsilon^{\mathrm{ex1}} D\frac{\partial c}{\partial x}\right) + \left(-\frac{c}{nF}\left[2\bar{V}_{\mathrm{o}} - (3-2t_+^{\mathrm{o}})\bar{V}_e\right] - \frac{(3-2t_+^{\mathrm{o}})}{nF}\right)\frac{\partial i_2}{\partial x} = 0\end{aligned} \tag{3.21}$$

Note that (3.21) accounts for material changes due to the electrochemical reaction and mass transport effects from convection, diffusion and migration in the positive electrode region [36].

The electrolyte's diffusion coefficient, represented by D in cm^2/s, depends on the electrolyte concentration and temperature according to:

$$D = 1\times10^{-5}\left(1.75 + 260c\right)\exp(2174/T_{\mathrm{ref}} - 2174/T) \tag{3.22}$$

with T_{ref} the reference temperature of $298.15\,\mathrm{K}\ (25°\ \mathrm{C})$ [71].

The reference concentration is calculated using:

$$c_{\mathrm{ref}} = -2.9\times10^{-6}T + 5.75\times10^{-3} \tag{3.23}$$

to account for conditions other than the reference temperature [63].

3.4.5 Electrode kinetics

The reaction current per unit volume or j $(\mathrm{A/cm}^3)$ is proportional to the overall reaction rate given by:

$$j = r = r_f(c^\gamma, a_v, \eta, T) - r_b(c^\gamma, a_v, \eta, T) \tag{3.24}$$

with r_f and r_b the forward and backward reaction rates.

The active surface area of the electrode is represented by a_v in cm^{-1} and the electrode overpotential by η in V. The exponent on the concentration (γ) indicates the order of the reaction [75].

Both rates, r_f and r_b, can be written using the Butler-Volmer equation in a concentration-dependent form as:

$$\begin{aligned} r_f &= a_v i_{0,\text{ref}} \left(\frac{c}{c_{\text{ref}}} \right)^{\gamma} \exp\left(\frac{\alpha_a F}{RT} \eta \right) \\ r_b &= a_v i_{0,\text{ref}} \left(\frac{c}{c_{\text{ref}}} \right)^{\gamma} \exp\left(\frac{-\alpha_c F}{RT} \eta \right) \end{aligned} \tag{3.25}$$

with $i_{0,\text{ref}}$ the reaction current density at T_{ref} and c_{ref} [52].

The anodic (forward) and cathodic (backward) transfer coefficients, α_a and α_c, are related to the number of electrons transferred using:

$$\alpha_a + \alpha_c = n \tag{3.26}$$

A typical expression used for the active surface area (a_v) during discharge is written as:

$$a_v = a_{\max} \left(\Theta \right)^{\zeta} \tag{3.27}$$

where $a_{\max}$ is the maximum surface area for the electrode at full capacity and Θ is the electrode utilization variable [35].

The exponent ζ is an empirical parameter and accounts for the manner in which the sulphate crystals cover the surface of the electrode. Its value can be taken from previous works or determined by parameter estimation.

Electrode utilization (Θ) can be a function of the charge per unit volume Q (C/cm^3) [36] or electrode porosity (ε) and is used to relate the active surface area to the amount of conductive materials in a porous electrode [71].

With $Q_{\max}$ the maximum charge capacity of the electrode, the active surface area can be written as:

$$\begin{aligned} a_v &= a_{\max} \left(\frac{Q}{Q_{\max}} \right)^{\zeta} \quad \text{(discharge and rest)} \\ a_v &= a_{\max} \left(\frac{Q}{Q_{\max}} \right)^{\zeta} \left(1 - \frac{Q}{Q_{\max}} \right) \quad \text{(charge)} \end{aligned} \tag{3.28}$$

with Q the charge per unit volume during operation. It should be clear from this equation that electrode utilization actually refers to the electrode's state-of-charge or local SOC [36].

When using the maximum electrode porosity ($\varepsilon_{\max}$) in an expression of Θ, the active surface area is given by:

$$\begin{aligned} a_v &= a_{\max}\left(\frac{\varepsilon-\varepsilon_0}{\varepsilon_{\max}-\varepsilon_0}\right)^{\zeta} \quad \text{(discharge and rest)} \\ a_v &= a_{\max}\left(\frac{\varepsilon-\varepsilon_0}{\varepsilon_{\max}-\varepsilon_0}\right)^{\zeta}\left(\frac{\varepsilon_{\max}-\varepsilon}{\varepsilon_{\max}-\varepsilon_0}\right) \quad \text{(charge)} \end{aligned} \tag{3.29}$$

with ε_0 the porosity of a drained electrode. The charge per unit volume (Q) is related to the electrode reaction current according to:

$$\frac{\partial Q}{\partial t} = j \tag{3.30}$$

To arrive at the complete equation for j, (3.27) is substituted into (3.25) to expand (3.24) into the Butler-Volmer equation and written as:

$$j = a_{\max} i_{0,\text{ref}}\left(\frac{c}{c_{ref}}\right)^{\gamma}\left[\exp\left(\frac{\alpha_a F}{RT}\eta\right)-\exp\left(-\frac{\alpha_c F}{RT}\eta\right)\right](\Theta)^{\zeta} \tag{3.31}$$

with Θ as given in (3.28) or (3.29). In this study, the electrode utilization will be calculated using the porosity expressions of (3.29). For the model developed here, an extra term is added to (3.31) to account for the capacitance of the EDL (C_{dl}) in F/cm^2 to obtain:

$$\begin{aligned} j = a_{\max} i_{0,\text{ref}}\left(\frac{c}{c_{ref}}\right)^{\gamma}\left[\exp\left(\frac{\alpha_a F}{RT}\eta\right)-\exp\left(-\frac{\alpha_c F}{RT}\eta\right)\right](\Theta)^{\zeta} + \\ C_{\text{dl}} a_{\max}\left(\frac{\partial \phi_1}{\partial t}-\frac{\partial \phi_2}{\partial t}\right) \end{aligned} \tag{3.32}$$

with the overpotential, $\eta = \phi_1 - \phi_2 - U_{\text{PbO}_2}$, explained shortly in its own section [35]. The reaction current density at reference conditions ($i_{0,\text{ref}}$) is used to calculate the reaction current density at other conditions (i_0) as:

$$i_0 = i_{0,\text{ref}} \exp\left[E_{\text{A}}\left(T - T_{\text{ref}}\right)/\left(RT_{\text{ref}}T\right)\right] \tag{3.33}$$

where E_{A} is the activation energy in J/mol [63].

3.5 Overpotential

The overpotential (η) for the positive electrode reaction is given by:

$$\eta = \phi_1 - \phi_2 - E_{\text{PbO}_2} \tag{3.34}$$

with U_{PbO_2} the equilibrium potential of the positive electrode.

This equilibrium electrode potential is typically measured at $25\ °C$ with a standard hydrogen electrode (SHE) as the reference electrode in a three-electrode setup to obtain $E_{PbO_2} = 1.685\ V$. Most practical requirements do not allow for the insertion of a reference electrode. The solution is to use a Pb electrode as reference because it is made of the same material as the electrode under consideration [36]. The equilibrium potential (E_{eq}) of the positive electrode with a Pb reference electrode is then given by:

$$\begin{aligned} E_{eq} &= E_{PbO_2} - E_{Pb} \\ &= 1.685 - (-0.356) \\ &= 2.041\ V \end{aligned} \tag{3.35}$$

The standard electrode potential of PbO_2 is also influenced by the acid concentration according to:

$$\begin{aligned} E_{PbO_2}(m) = 1.628194 + 0.073924\log(m) + 0.03312\log^2(m) + \\ 0.043220\log^3(m) + 0.021567\log^4(m) \end{aligned} \tag{3.36}$$

with *m* the molality of the electrolyte in mol/kg [95]. This concentration dependence for the negative Pb electrode is written as:

$$\begin{aligned} E_{Pb}(m) = -0.294606 - 0.073595\log(m) - 0.030432\log^2(m) - \\ 0.030552\log^3(m) - 0.012045\log^4(m) \end{aligned} \tag{3.37}$$

Subtracting (3.37) from (3.36) results in the concentration-dependent expression for the equilibrium potential (E_{eq}) of the positive electrode and is given by:

$$\begin{aligned} E_{eq}(m) &= E_{PbO_2}(m) - E_{Pb}(m) \\ &= 1.9228 + 0.147519\log(m) + 0.063552\log^2(m) + \\ &\quad 0.073772\log^3(m) + 0.033612\log^4(m) \end{aligned} \tag{3.38}$$

with the molality calculated in (3.39) [95].

$$m = 1.00322\times10^3 c + 3.55\times10^4 c^2 + 2.17\times10^6 c^3 + 2.06\times10^8 c^4 \tag{3.39}$$

The expression for the overpotential in the positive electrode region (d_1) from (3.34) with substitution of the concentration-dependent equilibrium potential then becomes:

$$\eta = \phi_1 - \phi_2 - E_{eq}(m) \tag{3.40}$$

It is important to note that an expression for the overpotential in the negative electrode region (d_3) will be required later for the electrode kinetics equation in the same region. With the same Pb reference electrode, the overpotential in d_3 is given by $\eta = \phi_1 - \phi_2$.

In Chapter 4, an alternative EMF characterization method for a lead-acid cell is presented. The resulting EMF curve will be compared with the equilibrium potential in (3.38) to determine its validity.

3.6 Governing equations for the separator, d_2

Consider the separator region (d_2) sandwiched between the positive and negative electrode regions as depicted in Figure 3-6.

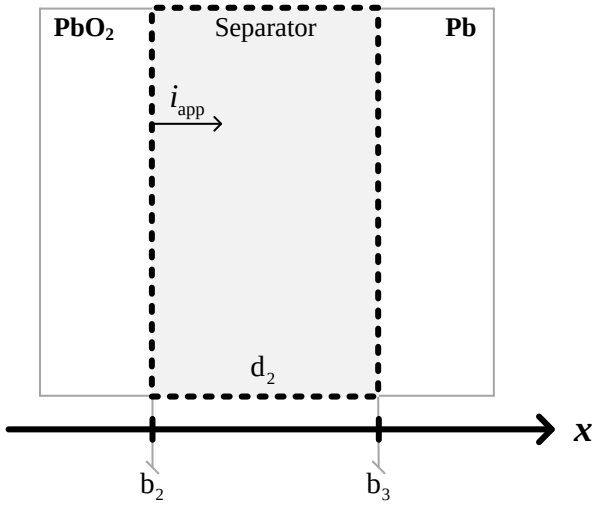

Figure 3-6: Region of the separator area referred to as the domain d_2 in the multi-scale model

The separator is used for ion transport and does not have a porosity variation over time. This constant porosity, with SEP indicating the separator region, is written as:

$$\varepsilon = \varepsilon_{\text{SEP}} \tag{3.41}$$

Since there is no solid active material in d_2, the solid phase current becomes $i_1 = 0$ and Ohm's law results in:

$$i_2 = i_{\text{app}} \tag{3.42}$$

The equation for Ohm's law in the solution of d_2 is very similar to that of d_1 in (3.15) and is given by:

$$\frac{i_2}{\varepsilon_{\text{sep}}^{\text{ex2}}\kappa} + \frac{\partial \phi_2}{\partial x} - \frac{RT}{F}\left(1 - 2t_+^{\text{o}}\right)\frac{\partial \ln c}{\partial x} = 0 \tag{3.43}$$

with ex2 a correction factor for tortuosity in the liquid phase of d_2. Note again, however, that the porosity in the separator region is a constant represented by ε_{SEP}.

With $\partial\varepsilon/\partial t = 0$, the material balance for the electrolyte, which accounts for mass transport due to convection and diffusion, is written as:

$$\varepsilon_{\text{sep}}\frac{\partial c}{\partial t} + v^*\frac{\partial c}{\partial x} - \frac{\partial}{\partial x}\left(\varepsilon_{\text{sep}}^{\text{ex2}} D\frac{\partial c}{\partial x}\right) = 0 \tag{3.44}$$

The volume-averaged velocity (v^*) in the separator region is the same as at the interface between the separator and the positive electrode according to:

$$v^*\Big|_{x=\mathrm{d}_2} = v^*\Big|_{x=\mathrm{b}_2} \tag{3.45}$$

This velocity at the positive electrode, using (3.19), is then written as:

$$v^*\Big|_{x=\mathrm{b}_2} = -\frac{1}{nF}\left[\left(\frac{\mathrm{Mw}_{\mathrm{PbSO_4}}}{\rho_{\mathrm{PbSO_4}}} - \frac{\mathrm{Mw}_{\mathrm{PbO_2}}}{\rho_{\mathrm{PbO_2}}}\right) + 2\bar{V}_{\mathrm{o}} - (3-2t_+^{\mathrm{o}})\bar{V}_e\right] i_2 \tag{3.46}$$

Substitution of (3.46) into (3.44) results in:

$$\varepsilon_{\mathrm{sep}}\frac{\partial c}{\partial t} - \frac{1}{nF}\left[\left(\frac{\mathrm{Mw}_{\mathrm{PbSO_4}}}{\rho_{\mathrm{PbSO_4}}} - \frac{\mathrm{Mw}_{\mathrm{PbO_2}}}{\rho_{\mathrm{PbO_2}}}\right) + 2\bar{V}_{\mathrm{o}} - (3-2t_+^{\mathrm{o}})\bar{V}_e\right] i_2\frac{\partial c}{\partial x} - \frac{\partial}{\partial x}\left(\varepsilon_{\mathrm{sep}}^{\mathrm{ex2}} D\frac{\partial c}{\partial x}\right) = 0 \tag{3.47}$$

as the complete material balance for the electrolyte in d_2.

3.7 Governing equations for the negative electrode, d_3

The major differences between the equations for the region d_3 as depicted in Figure 3-7 and the equations for d_1 are due to the different material properties of Pb and $\mathrm{PbO_2}$.

The electrochemical reactions at the separate electrodes make use of different stoichiometric coefficients as explained earlier.

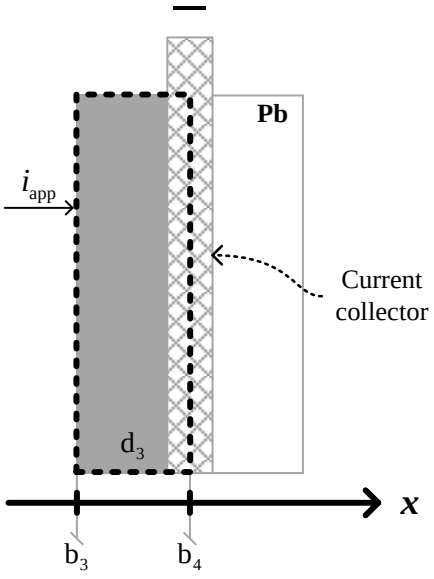

Figure 3-7: Region of the negative electrode area referred to as d_3 in the multi-scale model

The derivations of negative electrode counterparts for (3.9), (3.13), (3.15), (3.21) and (3.32) are the same and not repeated here.

The conductivity of lead (σ_{Pb}) is dependent on temperature and is calculated using:

$$\sigma_{\mathrm{Pb}} = 4.8\times10^{4} / \left[1 + 4.22\times10^{-3}(T - 293.15)\right] \tag{3.48}$$

The conductivity of the positive electrode $(\sigma_{\mathrm{PbO_2}})$ is usually taken as a constant [95].

3.8 Complete governing equations for the unit cell

The preceding sections presented the derivations for d_1 in detail whereas the equations for the separator and negative electrode domains were briefly discussed. The governing equations are simplified using various constants K_i as given in Table 3-2. As an example, take (3.9) written as

$$\frac{\partial \varepsilon}{\partial t} + K_1 j = 0 \qquad \text{with} \qquad K_1 = -\frac{1}{nF}\left(\frac{\mathrm{Mw}_{\mathrm{PbSO_4}}}{\rho_{\mathrm{PbSO_4}}} - \frac{\mathrm{Mw}_{\mathrm{PbO_2}}}{\rho_{\mathrm{PbO_2}}}\right) \tag{3.49}$$

With similar modifications to the governing equations for all three domains using the constants K_i in Table 3-2, the equations in Table 3-3 are obtained. The constants in d_2 are the same as those used in d_1 because of the relationship in (3.45).

Table 3-2: Expressions for K_i constants used in governing equations

Constant	*Positive electrode region,* d_1	*Negative electrode region,* d_3
K_1	$-\frac{1}{nF}\left(\frac{\mathrm{Mw}_{\mathrm{PbSO_4}}}{\rho_{\mathrm{PbSO_4}}} - \frac{\mathrm{Mw}_{\mathrm{PbO_2}}}{\rho_{\mathrm{PbO_2}}}\right)$	$\frac{1}{nF}\left(\frac{\mathrm{Mw}_{\mathrm{PbSO_4}}}{\rho_{\mathrm{PbSO_4}}} - \frac{\mathrm{Mw}_{\mathrm{Pb}}}{\rho_{\mathrm{Pb}}}\right)$
K_2	$-\frac{RT}{F}\left(1 - 2t_+^{\mathrm{o}}\right)$	
K_3	$K_1 + K_4$	
K_4	$-\frac{1}{nF}\left[2\bar{V}_{\mathrm{o}} - \left(3 - 2t_+^{\mathrm{o}}\right)\bar{V}_{\mathrm{e}}\right]$	$\frac{\left(1 - 2t_+^{\mathrm{o}}\right)}{nF}\bar{V}_{\mathrm{e}}$
K_5	$-\frac{\left(3 - 2t_+^{\mathrm{o}}\right)}{nF}$	$-\frac{\left(1 - 2t_+^{\mathrm{o}}\right)}{nF}$
K_6	$a_{\max} i_0$	
K_7	$\frac{\alpha_a F}{RT}$	
K_8	$\frac{\alpha_c F}{RT}$	
K_9	$C_{\mathrm{dl}} a_{\max}$	

Table 3-3: Governing equations for the POS, SEP and NEG regions

Positive electrode region, $\mathrm{d}_1 = 0 : l_{\mathrm{POS}}$	
Porosity variation	$\dfrac{\partial \varepsilon}{\partial t} + K_1 j_{\mathrm{PbO_2}} = 0$
Ohm's law in a solution	$\dfrac{i_2}{\varepsilon^{\mathrm{ex1}} \kappa} + \dfrac{\partial \phi_2}{\partial x} + K_2 \dfrac{\partial \ln c}{\partial x} = 0$
Ohm's law in a solid	$i_2 - \varepsilon^{\mathrm{exm1}} \sigma_{\mathrm{PbO_2}} \dfrac{\partial \phi_1}{\partial x} = i_{\mathrm{app}}$
Material balance	$\varepsilon \dfrac{\partial c}{\partial t} + K_3 i_2 \dfrac{\partial c}{\partial x} - \dfrac{\partial}{\partial x}\left(\varepsilon^{\mathrm{ex1}} D \dfrac{\partial c}{\partial x} \right) + \left(K_4 c + K_5 \right) j_{\mathrm{PbO_2}} = 0$
Electrode kinetics	$j = K_6 \left(\dfrac{c}{c_{ref}} \right)^{\gamma} \left[\exp\left(K_7 \eta \right) - \exp\left(-K_8 \eta \right) \right] \left(\Theta \right)^{\zeta} + K_9 \left(\dfrac{\partial \phi_1}{\partial t} - \dfrac{\partial \phi_2}{\partial t} \right)$
Separator region, $\mathrm{d}_2 = l_{\mathrm{POS}} : l_{\mathrm{POS}} + l_{\mathrm{SEP}}$	
Ohm's law in a solution	$\dfrac{i_2}{\varepsilon_{\mathrm{sep}}^{\mathrm{ex2}} \kappa} + \dfrac{\partial \phi_2}{\partial x} + K_2 \dfrac{\partial \ln c}{\partial x} = 0$
Material balance	$\varepsilon_{\mathrm{sep}} \dfrac{\partial c}{\partial t} + K_3 i_2 \dfrac{\partial c}{\partial x} - \dfrac{\partial}{\partial x}\left(\varepsilon_{\mathrm{sep}}^{\mathrm{ex2}} D \dfrac{\partial c}{\partial x} \right) = 0$
Other variables	$\varepsilon = \varepsilon_{\mathrm{sep}}, \quad \phi_1 = 0, \quad i_2 = i_{\mathrm{app}}$
Negative electrode region, $\mathrm{d}_3 = l_{\mathrm{POS}} + l_{\mathrm{SEP}} : l_{\mathrm{POS}} + l_{\mathrm{SEP}} + l_{\mathrm{NEG}}$	
Porosity variation	$\dfrac{\partial \varepsilon}{\partial t} + K_1 j = 0$
Ohm's law in a solution	$\dfrac{i_2}{\varepsilon^{\mathrm{ex2}} \kappa} + \dfrac{\partial \phi_2}{\partial x} + K_2 \dfrac{\partial \ln c}{\partial x} = 0$
Ohm's law in a solid	$i_2 - \varepsilon^{\mathrm{exm3}} \sigma_{\mathrm{Pb}} \dfrac{\partial \phi_1}{\partial x} = i_{\mathrm{app}}$
Material balance	$\varepsilon \dfrac{\partial c}{\partial t} + K_3 i_2 \dfrac{\partial c}{\partial x} - \dfrac{\partial}{\partial x}\left(\varepsilon^{\mathrm{ex3}} D \dfrac{\partial c}{\partial x} \right) + \left(K_4 c + K_5 \right) j = 0$
Electrode kinetics	$j = K_6 \left(\dfrac{c}{c_{ref}} \right)^{\gamma} \left[\exp\left(K_7 \eta \right) - \exp\left(-K_8 \eta \right) \right] \left(\Theta \right)^{\zeta} + K_9 \left(\dfrac{\partial \phi_1}{\partial t} - \dfrac{\partial \phi_2}{\partial t} \right)$

3.9 Boundary conditions

With the governing equations for all three domains presented, the boundary conditions between each domain are now explained. The major principle in the boundary conditions is that the current must be only ionic at the separator and only electronic at the collectors [52]. External boundary conditions were chosen to represent a sealed unit. The discharge current is applied to the left external boundary (b_1) and the right external boundary (b_4) corresponds to electric ground. At these two external boundaries, there is no pore-filling electrolyte and therefore, no superficial current density.

3.9.1 Centre of the positive electrode, b_1

The plane of symmetry used in the unit cell implies that, at an external boundary such as b_1, the following conditions hold:

$$\frac{\partial \varepsilon}{\partial x} = 0, \quad \frac{\partial \phi_2}{\partial x} = 0, \quad \frac{\partial c}{\partial x} = 0 \tag{3.50}$$

Since all of the current is in the collector and none is in the electrolyte at this boundary, a condition for the current in the liquid phase is written as:

$$i_2 = 0 \tag{3.51}$$

The potential in the solid phase is simply given by:

$$\phi_1 = E_{\text{eq}} \tag{3.52}$$

3.9.2 Interface between positive electrode and separator, b_2

This boundary is an internal boundary at a transitional interface between the electrode and the separator which means that the molar flux of the ions across the interface must be continuous. This flux continuity for the interface between positive electrode and separator is given by [71]:

$$\varepsilon^{\text{ex1}} \frac{\partial c}{\partial x}\bigg|_{x=\text{d}_1} = \varepsilon_{\text{sep}}^{\text{ex2}} \frac{\partial c}{\partial x}\bigg|_{x=\text{d}_2} \tag{3.53}$$

According to the the macro-homogenous approach [71], the current density in the electrolyte should also remain continuous across this interface and the continuity is stated as:

$$\varepsilon^{\text{ex1}} \frac{\partial \phi_2}{\partial x}\bigg|_{x=\text{d}_1} = \varepsilon_{\text{sep}}^{\text{ex2}} \frac{\partial \phi_2}{\partial x}\bigg|_{x=\text{d}_2} \tag{3.54}$$

The variation of porosity with time within the interface is the same as in the electrode and is given by:

$$\frac{\partial \varepsilon}{\partial t} = \frac{1}{nF}\left(\frac{\text{Mw}_{\text{PbSO}_4}}{\rho_{\text{PbSO}_4}} - \frac{\text{Mw}_{\text{PbO}_2}}{\rho_{\text{PbO}_2}}\right)\frac{\partial i_2}{\partial x}\bigg|_{x=\text{d}_1} \tag{3.55}$$

The separator is present at this boundary and implies that the current can only be ionic throughout the separator according to:

$$i_2 = i_{\text{app}} \tag{3.56}$$

Since all of the current is in the electrolyte phase, there can also be no solid-phase potential gradient and the boundary condition is written as:

$$\left.\frac{\partial \phi_1}{\partial x}\right|_{x=\mathrm{d}_1} = 0 \tag{3.57}$$

3.9.3 Interface between separator and negative electrode, b_3

The same reasoning for the boundary conditions of b_2 is used to obtain the boundary conditions for b_3 in (3.58)-(3.62).

$$\varepsilon_{\text{sep}}^{\text{ex2}} \left.\frac{\partial c}{\partial x}\right|_{x=\mathrm{d}_2} = \varepsilon^{\text{ex3}} \left.\frac{\partial c}{\partial x}\right|_{x=\mathrm{d}_3} \tag{3.58}$$

$$\varepsilon_{\text{sep}}^{\text{ex2}} \left.\frac{\partial \phi_2}{\partial x}\right|_{x=\mathrm{d}_2} = \varepsilon^{\text{ex3}} \left.\frac{\partial \phi_2}{\partial x}\right|_{x=\mathrm{d}_3} \tag{3.59}$$

$$\frac{\partial \varepsilon}{\partial t} = -\frac{1}{nF}\left(\frac{\mathrm{Mw}_{\mathrm{PbSO_4}}}{\rho_{\mathrm{PbSO_4}}} - \frac{\mathrm{Mw}_{\mathrm{Pb}}}{\rho_{\mathrm{Pb}}}\right)\left.\frac{\partial i_2}{\partial x}\right|_{x=\mathrm{d}_3} \tag{3.60}$$

$$i_2 = i_{\text{app}} \tag{3.61}$$

$$\left.\frac{\partial \phi_1}{\partial x}\right|_{x=\mathrm{d}_2} = 0 \tag{3.62}$$

3.9.4 Centre of the negative electrode, b_4

This boundary is the other external boundary of the unit cell which means that (3.50) and (3.51) of b_1 hold true here. The solid-phase potential at the current collector of the negative electrode is given by:

$$\phi_1 = 0 \tag{3.63}$$

The governing equations and boundary conditions of the multi-scale model have now been presented. Initial conditions will be discussed during numerical simulation in Section 5.2.

The several input parameters of the multi-scale model presented in this chapter will be subjected to a parametric analysis in Chapter 5 and parameter estimation in Chapter 6.

3.10 Conclusions

In this chapter, the macro-homogeneous approach was applied to a lead-acid cell in the development of a multi-scale electrochemical model. The model was defined by numerous partial differential equations derived using material balance equations, Ohm's law and the concentration-dependent Butler-Volmer equation for electrode kinetics. The boundary conditions for the two external and two internal boundaries were also explained.

Convection in the separator electrolyte for a VRLA cell with an immobile electrolyte is a new feature of the model presented in this thesis. Additionally, the mutli-scale model does not consider the cell to be isothermal. The cell's internal temperature variations are not explicitly modelled but the effects of temperature variations are taken into account using equations (3.16), (3.22) and (3.48). Further temperature considerations are discussed in the next chapter.

The multi-scale model is an integration of various previous efforts based on the macro-homogeneous approach. As such, the model's value as a research contribution is not based in its equations but rather in its utility. Following experimental model validation, the multi-scale model will be used to simulate the electrode surface areas during the operating modes that cause irreversible sulphation. The model does not contain explicit equations describing sulphation of the porous electrodes.

A second contribution by this study consists of an alternative method to characterize a lead-acid cell's EMF. The resulting EMF curve, which represents the cell's actual behaviour, finds its worth during parameter estimation for the multi-scale model. EMF characterization is discussed in detail in the following chapter.

4 ELECTROMOTIVE FORCE CHARACTERIZATION OF A LEAD-ACID CELL

This chapter starts with a brief overview of the existing methods for electromotive force (EMF) characterization. The inspiration behind an alternative concentration-based method is presented and its implementation is explained. The proposed method for EMF characterization is applied to experimental data from VRLA cells and its performance is compared to existing methods. The validation results indicate a significant improvement in accuracy and applicability over linear interpolation and linear extrapolation. As such, the concentration-based method for EMF characterization presented here is a secondary contribution of this study. The end result is a curve of the lead-acid cell's measured EMF against estimated electrolyte molality.

4.1 Existing methods for EMF characterization

EMF characterization utilizes macroscopic data to extract information regarding a cell or battery's inherent behaviour. Data such as voltage and current measurements are the norm in a typical battery energy storage application [96]. As such, methods that make use of readily available data are emphasized here.

Complex methods employing techniques such as electrochemical impedance spectroscopy (EIS) require specialized equipment and expertise which the general battery user cannot be expected to own. The existing methods for EMF characterization under consideration are known as voltage relaxation, linear interpolation and linear extrapolation [97]. These methods result in a curve with the state-of-charge (SOC) on the *x*-axis and the EMF on the *y*-axis.

4.1.1 Voltage relaxation

This EMF characterization method makes use of fully relaxed open-circuit voltage (OCV) measurements to relate the EMF to SOC [97]. The voltage relaxation method consists of discharging a fully charged cell in small capacity intervals at a low rate until completely empty. At each interval, the cell is given a predefined rest period for the OCV to relax and the EMF is recorded. The resulting data points are used to fit an EMF-SOC curve valid for discharge. To obtain the EMF-SOC curve valid for charge, the empty cell is charged using the same rate and capacity intervals as the discharge step until completely recharged.

By using more intervals during the characterization, additional points can be obtained to increase the accuracy of the fitted EMF curve. Doing so results in a costly increase in time due to the intermittent rest periods required for OCV measurement [64]. The associated time commitment of the voltage relaxation method favours the use of the other two methods which are called linear interpolation and linear extrapolation [98].

4.1.2 Linear interpolation

EMF characterization via linear interpolation consists of averaging the measured voltage profiles during discharging and charging [59]. A fully charged battery is discharged at a low rate until empty, and then charged from empty to full using the same current magnitude. Linear interpolation does not require intermittent rest periods for OCV measurements. Instead, the EMF at a specific SOC is calculated as the average between the charge (v_c) and discharge voltage (v_d) and is shown in Figure 4-1 [48].

The resulting interpolated EMF values (E_{int}) are used to obtain a fit (E_{fit}) of the EMF-SOC curve. Notice that EMF characterization using linear interpolation results in a single EMF-SOC curve unlike the two curves from the voltage relaxation method.

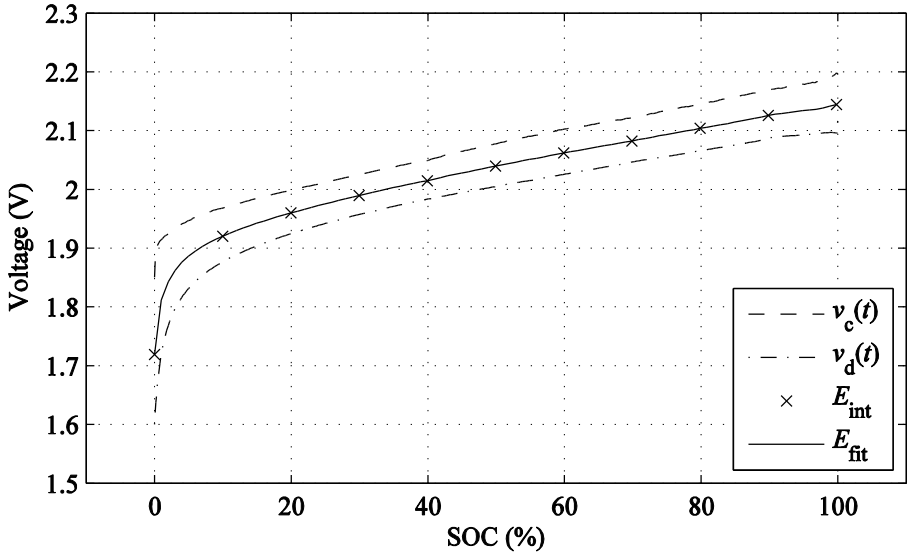

Figure 4-1: Illustration of EMF characterization using linear interpolation

4.1.3 Linear extrapolation

Obtaining an EMF-SOC curve using linear extrapolation requires multiple voltage curves from either charge or discharge [97]. A full battery is discharged at a low rate until empty, at least twice, using different current magnitudes. The data points at a specific SOC are extrapolated to zero current for the OCV – this value is then taken as the EMF at the same SOC. The various EMF values are then used to fit an EMF-SOC curve valid for discharge.

Similarly, the EMF curve valid for charge is obtained by charging an empty battery to full, at least twice, using different current magnitudes. As illustrated in Figure 4-2, the curves $(v_{c,1})$ and $(v_{c,2})$ are the voltage curves at two different charging rates and (E_{ext}) the extrapolated EMF values. These EMF values are used to obtain a fit (E_{fit}) of the EMF-SOC curve valid for charge.

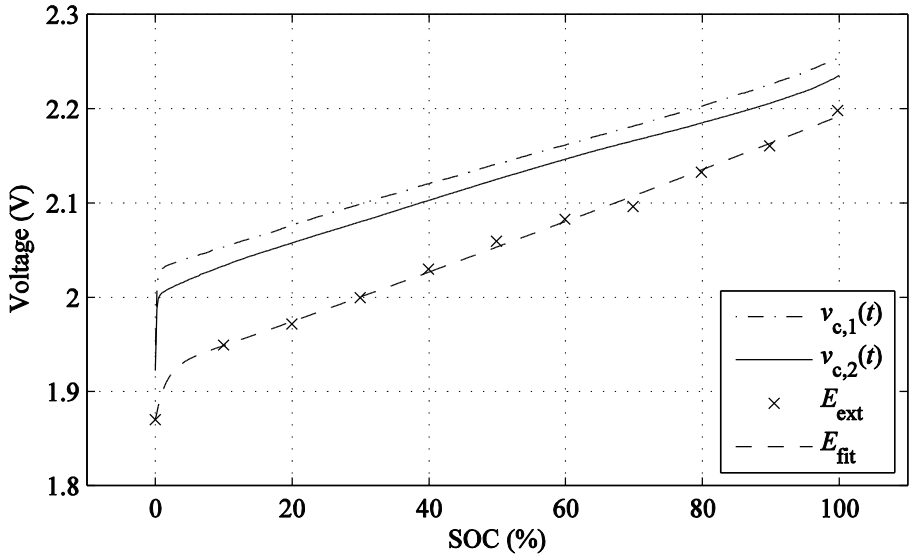

Figure 4-2: Illustration of EMF characterization using linear extrapolation for charge

Take note that linear extrapolation results in two EMF-SOC curves, even though linear extrapolation for discharge is not illustrated here. The only method that does not result in two curves – one valid for charge and another valid for discharge – is the linear interpolation method for EMF characterization.

4.1.4 Shortcomings of existing methods for EMF characterization

The existing methods for EMF characterization involve somewhat more than the simple explanations offered here and the reader is referred to the previous works of Bergveld [97] and Pop [59], [99]. For comparison purposes with the concentration-based method presented later, the shortcomings of the existing methods are more important at this point.

Linear interpolation assumes that the cell's internal resistance is symmetric during charge and discharge, which is not the case in reality [48].

The other two methods, voltage relaxation and linear extrapolation, produce EMF-SOC curves wherein hysteresis effects can be observed and is more representative of actual behaviour [10].

Challenging requirements common to all three methods are the use of sufficiently low charge or discharge rates and a constant temperature environment [5]. It has been recommended that the chosen rate be smaller than 0.1C to avoid early entry into constant voltage (CV) charging [48].

The SOC calculations involved in the existing methods rely on predefining the battery as either full before starting a discharge or as empty before a charge. Without these reference values, the SOC cannot be calculated [97]. As discussed earlier, the three existing methods rely on SOC calculations which are known for integrating errors over time along with the charge into or out of the battery [59].

4.2 Concentration-based method for EMF characterization

An alternative method for EMF characterization has to use the same available information as the existing methods to enable a fair comparison. It should not, however, rely on SOC information because the aim is to avoid the problems inherent to SOC calculations. Battery capacity is usually specified in terms of the positive electrode's active mass – the amount of active material that can react with the electrolyte. Electrolyte concentration provides an alternative to using SOC information for characterization of the battery's behaviour. The Nernst equation is widely used to relate the EMF and the concentration of an electrochemical cell [58].

4.2.1 The Nernst equation applied to a lead-acid cell

The complete lead-acid cell reaction is repeated here as:

$$\mathrm{Pb} + \mathrm{PbO_2} + 2\mathrm{H_2SO_4} \rightleftarrows 2\mathrm{PbSO_4} + 2\mathrm{H_2O} \tag{4.1}$$

The Nernst equation for the complete reaction is written as:

$$E = 2.048 - \frac{RT}{2F}\ln Q \tag{4.2}$$

with E the cell's EMF, R the universal gas constant of 8.3144 $\mathrm{J}\cdot\left(\mathrm{mol}\cdot\mathrm{K}\right)^{-1}$, T the absolute temperature in K, F the Faraday constant of 96,485 $\mathrm{C}\cdot\mathrm{mol}^{-1}$ and Q the reaction quotient [51].

Eq. (4.2) enables the calculation of the EMF in non-standard conditions. The reaction quotient (Q) is the ratio of the product concentrations to the reactant concentrations, each raised to the power of their associated stoichiometric coefficient [51].

For the lead-acid cell reaction in (4.1), Q is written in terms of concentrations and species activities (a_i) in the following equation [10]:

$$Q = \frac{\left[\mathrm{PbSO_4}\right]^2\left[\mathrm{H_2O}\right]^2}{\left[\mathrm{Pb}\right]\left[\mathrm{PbO_2}\right]\left[\mathrm{H_2SO_4}\right]^2} = \left(\frac{a_{\mathrm{H_2O}}}{a_{\mathrm{H_2SO_4}}}\right)^2 \tag{4.3}$$

The activity of species i is given by $a_i = \gamma_i \cdot m$ wherein γ_i is the activity coefficient of the relevant species and m is the molality in $\mathrm{mol}\cdot\mathrm{kg}^{-1}$.

Substituting Q in terms of species activity from (4.3) into (4.2), results in the Nernst equation for the lead-acid cell as:

$$E(m,T) = 2.048 + \ln(10)\frac{RT}{F}\log_{10}\left(\frac{a_{H_2SO_4}}{a_{H_2O}}\right) \tag{4.4}$$

The Nernst equation as given in (4.4) provides a means of calculating a cell's EMF at the reference temperature and various molalities. The usefulness of molality is based in the fact that, unlike molarity, it is independent of temperature [5].

The molality of a vented LAB can be obtained by measuring the specific gravity of the electrolyte with a hydrometer. Measuring the molality of a commercially available valve-regulated LAB, particularly one with an immobile electrolyte, is no easy task.

Without the sophistication of experimental cell configurations in a laboratory environment, the aim at this point is to estimate the molality using the available information.

4.2.2 Inspiration behind the concentration-based method

Keeping in mind that the existing methods make use of voltage and current measurements to obtain an EMF curve, these measurements are now investigated. Consider Figure 4-3 illustrating a typical voltage profile of a lead-acid cell before $(t < t_1)$, during $(t_1 \le t \le t_2)$ and after $(t > t_2)$ discharge.

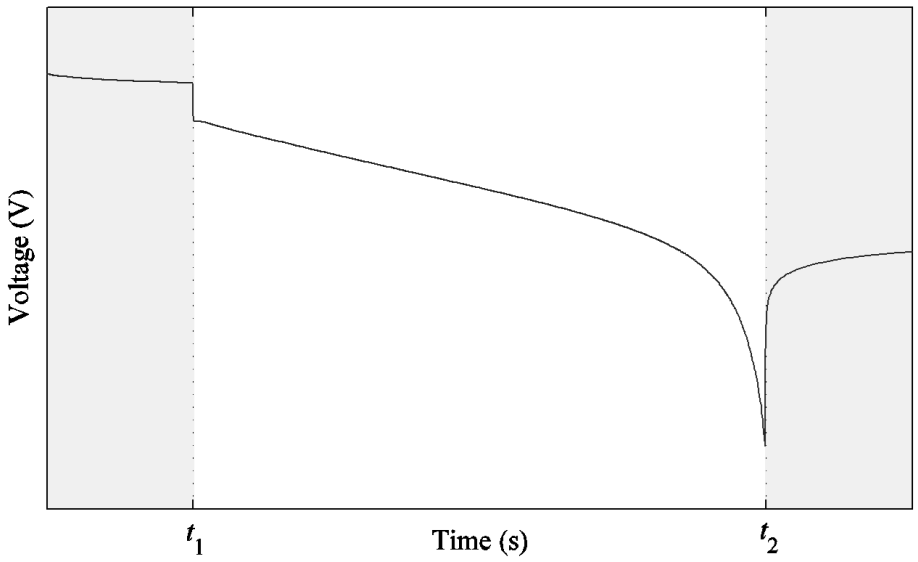

Figure 4-3: Typical voltage profile of a lead-acid cell before, during and after discharge

The electric work done by the cell (Δw) during discharge is the difference in the energy content before discharge and the remaining energy content after discharge.

The equation for this electric work done by the cell is written as:

$$\Delta w = w(t_1) - w(t_2) = w_1 - w_2 \tag{4.5}$$

with t_1 and t_2 denoting the time instances as illustrated in Figure 4-3.

The possible maximum electric work $(w_{\max})$ is the product of electric charge and a cell's EMF and is given by:

$$w_{\max} = n_e FE \tag{4.6}$$

with n_e the number of electrons involved in the reaction and F the Faraday constant [51].

Applying (4.6) to (4.5) results in an expression for the work performed by the cell during discharge as:

$$\Delta w = n_e F(E_1 - E_2) \tag{4.7}$$

with E_1 and E_2 the cell's EMF at time instances t_1 and t_2 in Figure 4-3.

Assuming a constant temperature of $T_{\text{ref}} = 298.15\ \text{K}\ (25\ ^\circ\text{C})$ for now, the Nernst equation in (4.4) provides $E_1 = E(m_1)$ and $E_2 = E(m_2)$ with m_1 and m_2 the electrolyte molality in $\text{mol}\cdot\text{kg}^{-1}$ at time instances t_1 and t_2 in Figure 4-3.

Substitution into (4.7) gives the electric work done by the cell written as:

$$\Delta w = n_e F\left[E(m_1) - E(m_2)\right] \tag{4.8}$$

Dividing Δw by the total discharge time (Δt) on both sides results in the following:

$$\frac{\Delta w}{\Delta t} \cdot \frac{1}{n_e F} = \frac{E(m_1) - E(m_2)}{\Delta t} \tag{4.9}$$

with $\Delta t = t_2 - t_1$. The result of (4.9) implies that a relationship exists between the rate of change in the electric work done by the cell and its change in concentration during operation [58]. This implied relationship is the inspiration behind the concentration-based EMF characterization method.

Implementations of the Nernst equation to predict or simulate the cell voltage can be found in the relevant literature [28]. To the best of the author's knowledge however, the concentration-based method presented here is an original research contribution.

4.3 Implementation of the concentration-based method

The required experimental data and subsequent calculations of the concentration-based method are now presented. Temperature considerations are explained and, where appropriate, calculations are provided. A full sample calculation is also presented after explaining the implementation of the concentration-based method for EMF characterization.

4.3.1 Experimental data

The voltage profile of a lead-acid cell during discharge as shown in Figure 4-3 is an example of the required experimental data for the calculations that follow shortly. The experiment consists of observing the cell at rest before discharge, discharging at a desired rate until the recommended cut-off voltage (COV) and then letting the cell rest again. The shaded areas in Figure 4-3 indicate when the cell was at rest and open-circuit voltage measurements were possible.

To obtain a representative discharge profile, it is recommended that the discharge starts with a cell that has been charged prior to the experiment and then completely rested. The terminal voltage, applied current and external temperature are measured and recorded throughout the whole experiment. The cells available for experimental measurements do not have internal temperature sensors and, since the aim is to keep the cell sealed, external sensors have to be used. The external temperature measurement is taken at the negative terminal as the best available estimate for the cell's temperature.

4.3.2 Open-circuit voltage measurements

The open-circuit voltage (OCV) is measured before $\left(t < t_1\right)$ and after discharge $\left(t > t_2\right)$ and recorded as the EMF values E_1^* and E_2^*. The OCV should only be measured when fully relaxed to obtain the EMF. Some researchers have found that the OCV can be considered stable if the change in voltage over time is lower than a specified threshold [100].

To ensure stable OCV measurements, the battery is allowed to rest for at least 3 hours and then checked to see if its voltage changes with less than 4 $\mu\mathrm{V}\cdot\mathrm{s}^{-1}$ for 60 seconds or longer. If the threshold condition is not satisfied, subsequent rest periods of 15 minutes and voltage tests are allowed until this threshold condition is met.

4.3.3 Temperature considerations

The earlier assumption of a constant temperature environment is not guaranteed outside of laboratory conditions. The values for the EMF, E_1^* and E_2^*, might have been measured at temperatures other than the reference temperature of $T_{\mathrm{ref}} = 298.15\ \mathrm{K}\ \left(25\ ^\circ\mathrm{C}\right)$. Temperature variations have a substantial effect on the cell's EMF and, as a result, on the OCV measurements [63].

For the explanation that follows, the time instant $(t_1 \text{ or } t_2)$ is disregarded for simplicity. It is possible to convert the EMF at a different temperature (T) to the EMF at the reference temperature (T_{ref}) by using a temperature coefficient. This coefficient $(\Delta E / \Delta T)$ for a given molality (m) is given by:

$$\frac{\Delta E}{\Delta T} = \Lambda_g\left(m\right) + \Lambda_h\left(m\right)\cdot\Delta T \tag{4.10}$$

with $\Delta E = E\left(m,T\right) - E\left(m,T_{\mathrm{ref}}\right)$ and $\Delta T = T - T_{\mathrm{ref}}$ [101].

The empirical constants, $\Lambda_g(m)$ and $\Lambda_h(m)$, were determined and validated by previous researchers for temperatures ranging from 0 to 60 °C at various molalities [102]. The relationship in (4.10) is illustrated in Figure 4-4.

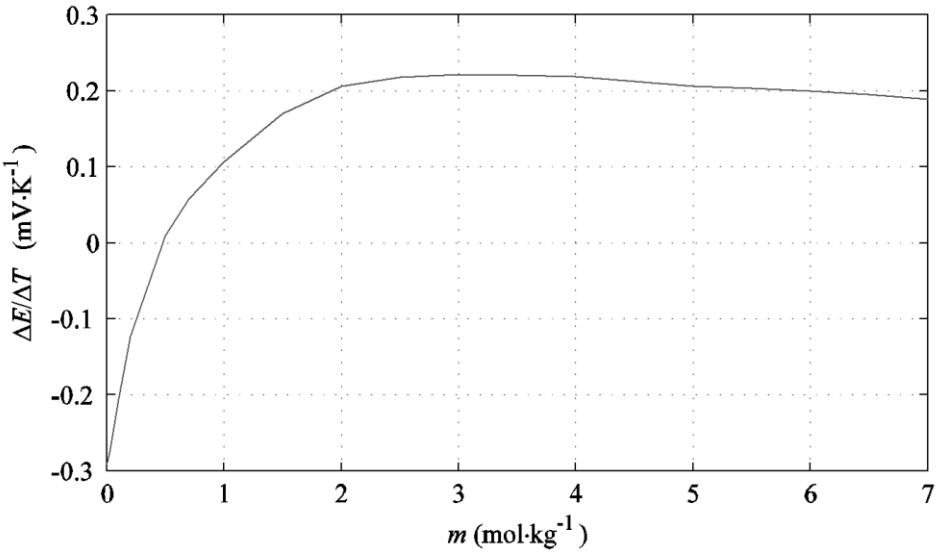

Figure 4-4: Reported temperature coefficient of EMF against electrolyte molality

Since the molality (*m*) is unknown at this point, $\Lambda_g(m)$ and $\Lambda_h(m)$ for (4.10) have to be determined in some other way.

4.3.4 Estimating electrolyte molality using EMF and temperature

The electrolyte concentration cannot simply be measured in advanced lead-acid batteries without modifying the battery or using specialized equipment [58]. The calculations used to estimate the electrolyte molality in the concentration-based method are now explained with the associated time instant still being disregarded.

The EMF at the reference temperature, $E(m,T_{\text{ref}})$, is reported in [10] and substituted into (4.10) to obtain the following:

$$E(m,T) = E(m,T_{\text{ref}}) + \Lambda_g(m)\cdot\Delta T + \Lambda_h(m)\cdot\Delta T^2 \tag{4.11}$$

This result is the predicted value of E at T for various m. If, for example, $E(m,T)$ was measured at $T = 308.15\ \text{K}\ (35\ °\text{C})$, (4.11) results in:

$$E(m,308.15) = E(m,298.15) + \Lambda_g(m)\cdot(10) + \Lambda_h(m)\cdot(10)^2 \tag{4.12}$$

with the resulting curve for $E(m,T)$ shown in Figure 4-5 (a).

The curve for $E\left(m,T_{\text{ref}}\right)$ as reported by Pavlov [10] is also shown even though the difference is hard to distinguish. Figure 4-5 (b) shows the same curves but over a smaller range for better visibility. In this example, the actual value of the EMF with $T = 308.15$ K was experimentally measured to be $E^{*}\left(m,T\right) = 2$ V.

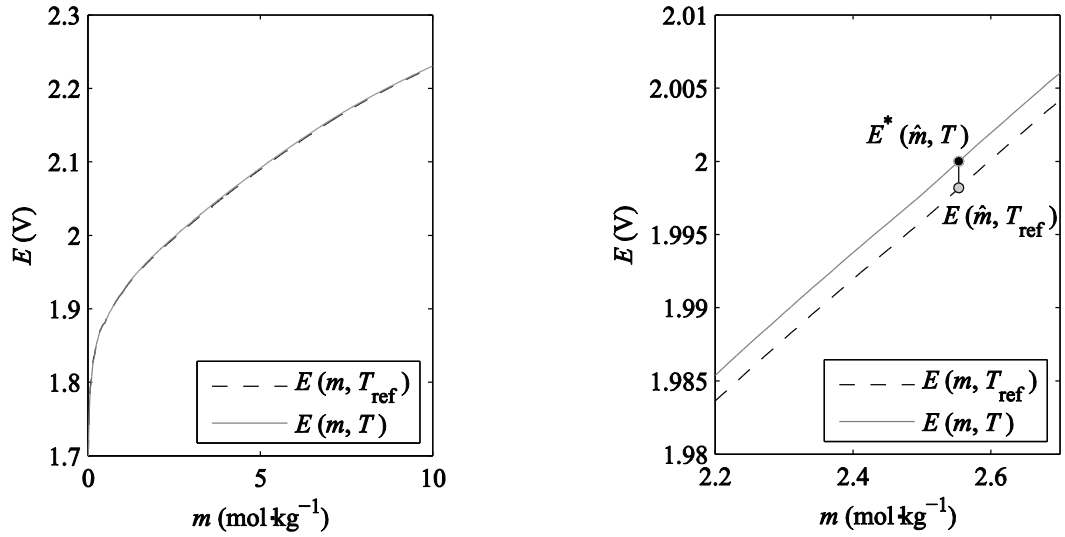

(a) (b)

Figure 4-5: (a) EMF at reference and measured temperatures against molality and (b) with the temperature coefficient also indicated

Since E^{*} should equal E at the same molality, 2 V is indicated in Figure 4-5 (b) on the curve of E and denoted as $E^{*}\left(\hat{m},T\right)$ with $\hat{m}$ the estimated molality. At this point, $\hat{m}$ can be obtained from the x-axis as $\hat{m} = 2.5535\ \text{mol}\cdot\text{kg}^{-1}$ and $E\left(\hat{m},T_{\text{ref}}\right) = 1.9982$ V.

The constants, Λ_g and Λ_h, in (4.10) can now be selected from [102] using $\hat{m}$ for the molality. Doing so provides $\Lambda_g = 1.74\text{e}^{-4}$ and $\Lambda_h = 9.97\text{e}^{-7}$. Substitution of these values into (4.10) produces a value for the temperature coefficient of the EMF as:

$$\frac{\Delta E}{\Delta T} = 1.74\text{e}^{-4} + 9.97\text{e}^{-7}\cdot 10 = 0.184\ \text{mV}\cdot\text{K}^{-1} \tag{4.13}$$

Using the values obtained from Figure 4-5 (b) to calculate the temperature coefficient of the EMF results in the following:

$$\frac{\Delta E}{\Delta T} = \frac{E^{*}\left(\hat{m},T\right) - E\left(\hat{m},T_{\text{ref}}\right)}{T - T_{\text{ref}}} = \frac{2 - 1.9982}{308.15 - 298.15} = 0.18\ \text{mV}\cdot\text{K}^{-1} \tag{4.14}$$

Since $0.184\ \text{mV}\cdot\text{K}^{-1} \approx 0.18\ \text{mV}\cdot\text{K}^{-1}$, the result of (4.13) is verified.

To summarize, the molality estimate $(\hat{m}_1)$ at t_1 in Figure 4-3 is obtained using the measured values of the EMF (E_1^*) and temperature (T_1) in the following relation:

$$E_1^* = E^*\left(\hat{m}_1, T_1\right) = E\left(\hat{m}_1, T_1\right) \tag{4.15}$$

The calculation of $\hat{m}_2$ is performed in the same manner using E_2^* and T_2 at instant t_2.

4.3.5 Electric work calculations

Molality estimates ($\hat{m}_1$ and $\hat{m}_2$) have been calculated using E_1^* and E_2^* but the EMF and the molality during discharge $(t_1 \le t \le t_2)$ are still unknown. The changes in the work done by the cell are now used to obtain the changes in molality during discharge as motivated by (4.9). From this point, $m_1 = \hat{m}_1$ and $m_2 = \hat{m}_2$ for the electrolyte molality at t_1 and t_2.

The electric work done by the cell at some instant t_k during discharge, $\Delta w(t_k)$, is the sum of the work done up until t_j with $j < k$ and the work done from t_j to t_k written as:

$$\Delta w(t_k) = \Delta w(t_j) + \int_{t_j}^{t_k} v_{\mathrm{d}}(\tau)\left|i_{\mathrm{d}}(\tau)\right| d\tau \tag{4.16}$$

with i_{d} and v_{d} the current and voltage measurements during discharge. At the beginning of discharge, the cell has not done any work yet and $\Delta w(t_1) = 0.$ Using $\Delta w(t_1) = \Delta w_1$ and $\Delta w(t_2) = \Delta w_2$, a mapping of the changes in work done by the cell to the changes in molality is given by:

$$\begin{aligned} &\frac{m(t_k) - m_1}{\Delta m} = \frac{\Delta w(t_k) - \Delta w_1}{\Delta(\Delta w)} \\ &\therefore m(t_k) = (m_2 - m_1)\cdot\left[\Delta w(t_k) - \Delta w_1\right] / (\Delta w_2 - \Delta w_1) + m_1 \end{aligned} \tag{4.17}$$

with $m(t_k)$ the estimated molality at some instant t_k during discharge. This estimated molality's species activities, as reported in [10], can be used to calculate the EMF at this instant, t_k, from the Nernst equation in (4.4). It should be mentioned that the approach explained in this section does not take irreversible energy losses into account.

4.3.6 Sample calculation using the concentration-based method

Consider Figure 4-6 showing the experimental voltage profile and measured temperature for a single-cell VRLA battery using an AGM separator with a rated capacity of $Q_{\mathrm{R}} = 4.5$ Ah over 20 h. The discharge current was $I_{\mathrm{d}} = -0.45$ A which is equal to a 0.1C rate.

The EMF and temperature measured at t_1 and t_2 are also indicated in Figure 4-6 and is given by:

$$\begin{aligned} E_1^* &= 2.1415 \text{ V}, T_1 = 16.7009 \text{ °C} \approx 289.9 \text{ K} \\ E_2^* &= 1.9588 \text{ V}, T_2 = 20.9892 \text{ °C} \approx 294.1 \text{ K} \end{aligned} \tag{4.18}$$

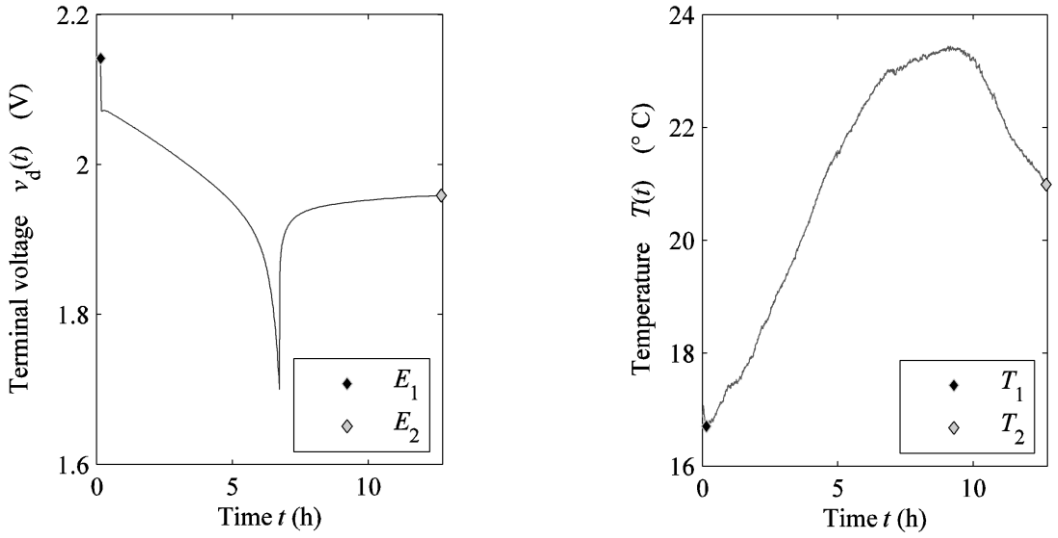

(a) (b)

Figure 4-6: (a) Experimental voltage profile and (b) measured temperature in the sample calculation of the concetration-based method for EMF characterization

Molality estimation as described in Section 4.3.4 at t_1 and t_2 can be seen in Figure 4-7 (a) and (b). The values of $m_1 = 6.6309\ \text{mol}\cdot\text{kg}^{-1}$ and $m_2 = 1.6602\ \text{mol}\cdot\text{kg}^{-1}$ are obtained from the data on the *x*-axis shown in Figure 4-7 (a) and (b). These are the estimates for the electrolyte molality just before discharge starts and at the end of discharge.

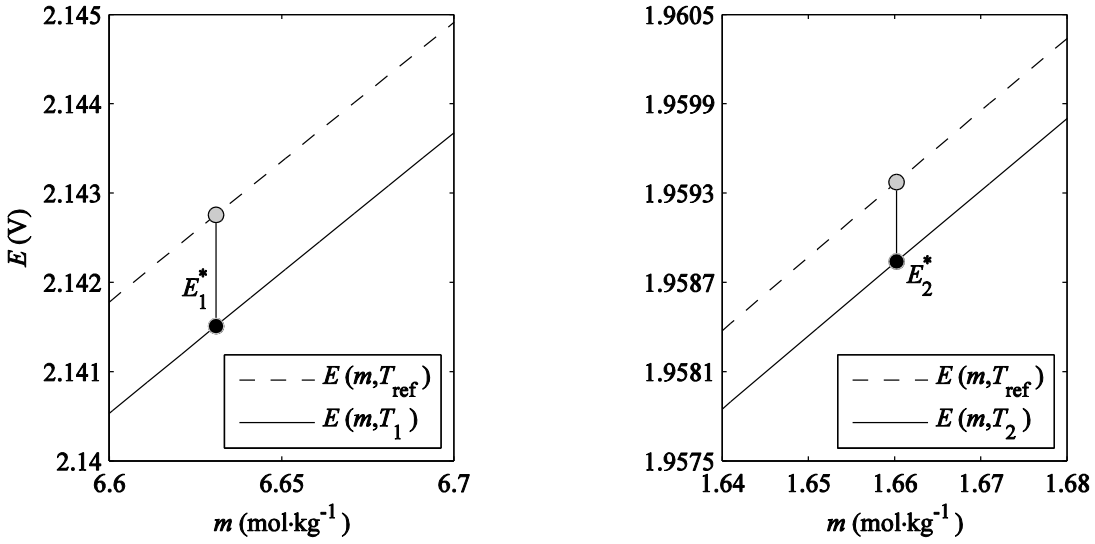

(a) (b)

Figure 4-7: (a) Molality estimation at the start of discharge and (b) at the end of discharge

The next step consists of estimating the molality during discharge from the changes in electric work done by the cell.

Using (4.16) with measurements of $v_{\mathrm{d}}(t)$ and $i_{\mathrm{d}}(t)$ and noting that $\Delta w_1 = 0$, the electric work performed by the cell is calculated as:

$$\Delta w_2 = 2.1076 \times 10^4 \text{ J} = 5.8545 \text{ Wh} \tag{4.19}$$

with $\Delta w(t_k)$ shown in Figure 4-8.

Selecting a time instant $t_k = 4.133$ h corresponds to a value for electric work done by the cell of $\Delta w(t_k) = 3.618$ Wh. Substitution of these values into (4.17) obtains the molality estimate as given in:

$$m(t_k) = (1.6602 - 6.6309) \cdot [3.618 - 0] / (5.8545 - 0) + 6.6309 = 3.5591 \text{ mol} \cdot \text{kg}^{-1} \tag{4.20}$$

where $T(t_k) = 20.59$ °C for the same time instant, $t_k = 4.133$ h.

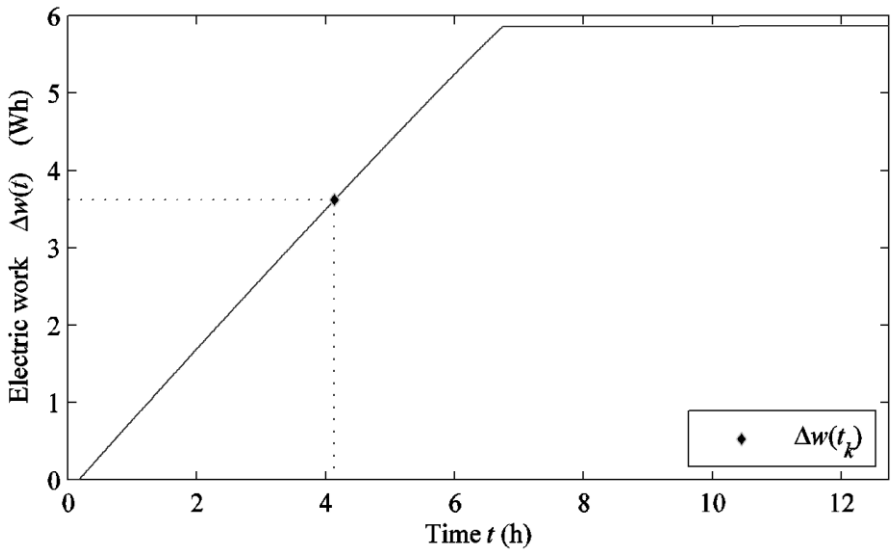

Figure 4-8: Changes in electric work done by the cell over time and sample at t_k

For $m(t_k) = 3.5591 \text{ mol} \cdot \text{kg}^{-1}$ and referring to [10], the species activities for the electrolyte and water are determined as $a_{\mathrm{H_2SO_4}} = 0.5459$ and $a_{\mathrm{H_2O}} = 0.8123$. Substitution of these species activities at $t_k = 4.133$ h into the Nernst equation of (4.4) results in:

$$\begin{aligned} E(m, T_{\mathrm{ref}}) &= 2.048 + \ln(10)\frac{RT_{\mathrm{ref}}}{F}\log_{10}\left(\frac{a_{\mathrm{H_2SO_4}}}{a_{\mathrm{H_2O}}}\right) \\ \therefore E(3.5591, 298.15) &= 2.048 + \left[\frac{(2.3026)(8.3144)(298.15)}{96485}\right]\log_{10}(0.672) \\ \therefore E(3.5591, 298.15) &= 2.0378 \text{ V} \end{aligned} \tag{4.21}$$

To obtain the EMF at $m(t_k) = 3.5591 \text{ mol} \cdot \text{kg}^{-1}$ and $T(t_k) = 20.59 \text{ °C} = 293.74 \text{ K}$, empirical constants as in (4.11) are used to correct for temperature effects on the EMF measurement:

$$\begin{aligned} & E(m,T) = E(m,T_{\text{ref}}) + \Lambda_g(m) \cdot \Delta T + \Lambda_h(m) \cdot \Delta T^2 \\ & \therefore E(3.5591, 293.74) = E(3.5591, 298.15) + \Lambda_g(3.5591) \cdot \Delta T + \Lambda_h(3.5591) \cdot \Delta T^2 \\ & \therefore E(3.5591, 293.74) = 2.0378 + 1.7766 \times 10^{-4} \cdot (-4.41) + 9.3957 \times 10^{-7} \cdot (-4.41)^2 \\ & \therefore E(3.5591, 293.74) = 2.0370 \text{ V} \end{aligned} \tag{4.22}$$

The same calculation is repeated for the complete experiment and the results are shown in Figure 4-9.

Even though a sample calculation has been presented for a discharge experiment, the same steps apply for a charge experiment. A different current magnitude to i_{d} may be used. It is recommended that the charge experiment starts with a cell which is more or less empty and then charged to full according to manufacturer's specifications. The same variables measured for the discharge experiment are measured for a charge experiment: terminal voltage, applied current and temperature.

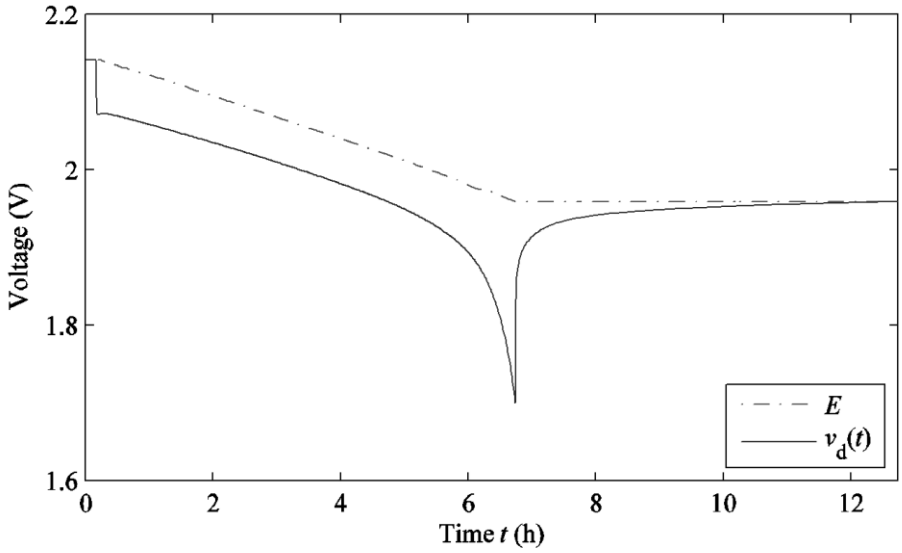

Figure 4-9: Terminal voltage and EMF for a complete discharge experiment in the sample calculation of the concentration-based method for EMF characterization

With the explanation of the concentration-based method for EMF characterization now complete, the next section focuses on verification and validation of this method.

4.4 Verification and validation of the concentration-based method

Even though the concentration-based method seems time-consuming in its explanation, computation in MATLAB® using experimental data from hundreds of charge/discharge cycles executes in seconds. As mentioned earlier, single-cell VRLA batteries with $Q_{\text{R}} = 4.5$ Ah over 20h were used for the collection of experimental data. A total of 8 cells were cycled at different rates ranging from 0.3C to 0.02C.

4.4.1 Verification

The concentration-based method's output (fitted curve) is verified in the current work by examining if: (i) the EMF is higher than the cell voltage during discharge, (ii) the EMF is lower than the cell voltage during charge and (iii) the EMF against estimated molality compares well with EMF values against actual molality as provided by literature.

Consider Figure 4-10 (a) which shows the fitted EMF against molality along with the discharge (v_d) and charge voltage profiles (v_c) for a cycle with rates of 0.04C and $I_{applied} = \mp 0.18\text{A}$.

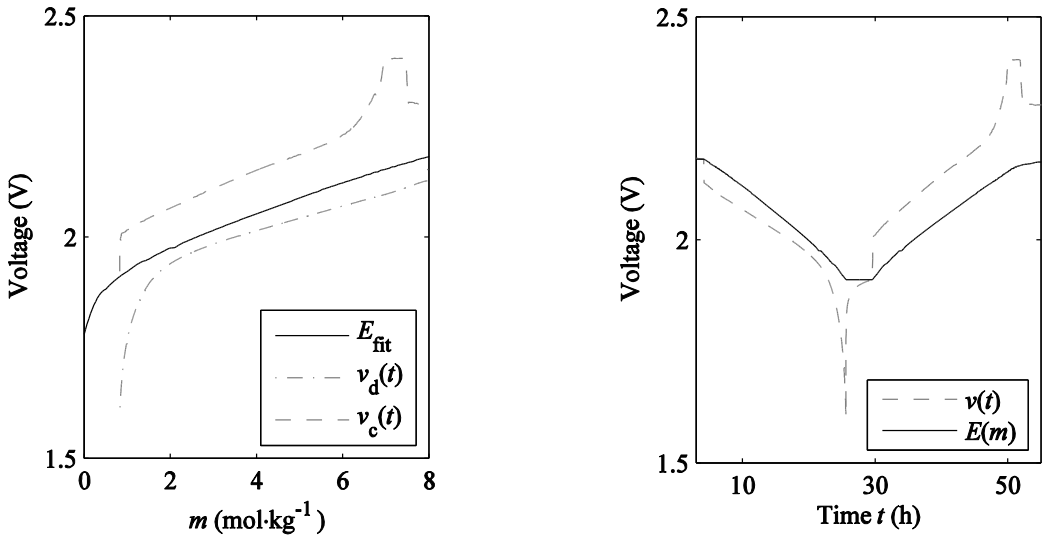

(a) (b)

Figure 4-10: Verification of (a) the fitted EMF curve against molality and (b) the estimated EMF over time with experimental discharge and charge voltage profiles (Rate: 0.04C, 25±3 °C)

Clearly, the EMF is lower than the cell voltage during charge and higher than the cell voltage during discharge – conditions (i) and (ii) for verification are satisfied. Figure 4-10 (b) displays the estimated EMF over time which was obtained using the fitted EMF curve. With regard to condition (iii), Cugnet et. al. [63] provides the relationship of EMF versus molality as determined by Bode [95] in 1977. This relationship, denoted as E_{Cugnet}, is shown in Figure 4-11.

Also shown in Figure 4-11 are several measured values of the cell's EMF denoted as E^* at their estimated molalities, *m*. The EMF curve fitted to these measured values (E^*) is also shown and denoted as E_{fit}. The results in Figure 4-11 compare well with E_{Cugnet} from literature and, as such, condition (iii) for verification of the concentration-based method's output is satisfied.

Since all three conditions for verification (i-iii) are satisfied, the EMF characterization using the concentration-based method is sufficiently verified.

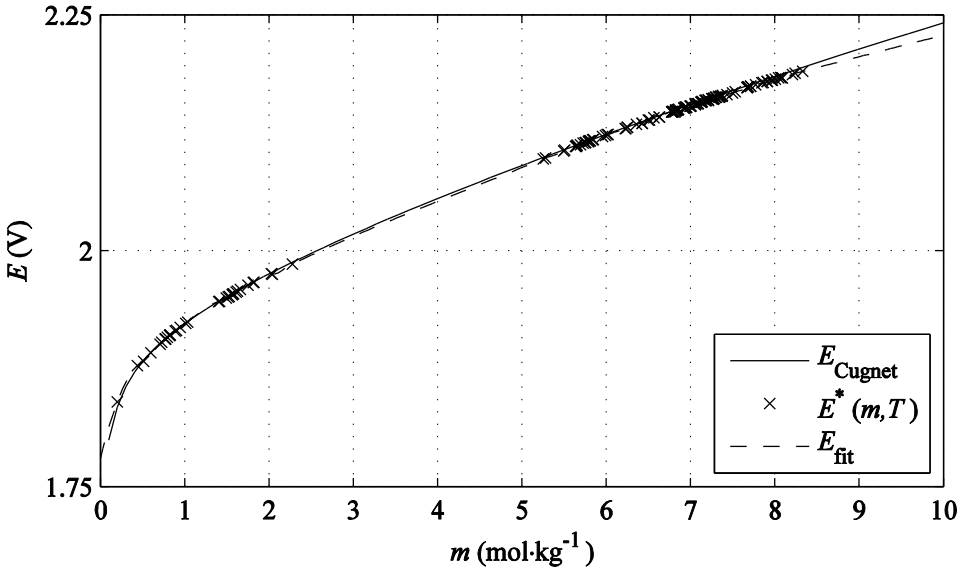

Figure 4-11: Verification of the fitted EMF using the EMF against molality from literature

4.4.2 Validation

Validation is performed by comparing the outputs from linear interpolation and linear extrapolation with the output from the concentration-based method. Regardless of the method, the measurement data used for validation is different than the measurement data used for characterization of the EMF.

EMF curves were obtained by fitting second-order exponential functions to the EMF values in MATLAB®. Figure 4-12 shows the EMF values at various SOC levels obtained from linear interpolation (E_{int}) and the validation data (E_{val}) as well as the discharge and charge voltage profiles. The SOC was calculated using Coulomb-counting and normalized to the maximum discharge capacity.

Normalization of the accumulated charge to the maximum capacity is still in use today [103], but its first documented use in linear interpolation for EMF characterization appeared in 2002 by Bergveld, Kruijt and Notten [48].

Notice that Figure 4-12 contains no EMF curve fitted to the EMF values. The charge and discharge voltage profiles were obtained using a 0.05C rate – a rate considered more than low enough to prevent early entry into the CV charging stage [48].

As can be seen in Figure 4-12, CV charging started around 85% SOC. The resulting EMF characterization around this area is incorrect and it was decided to repeat the linear interpolation method using lower rates of 0.04C and 0.02C. The EMF curve valid for charge using linear extrapolation also suffered from this complication and the cycling rates were also reduced to those used in linear interpolation.

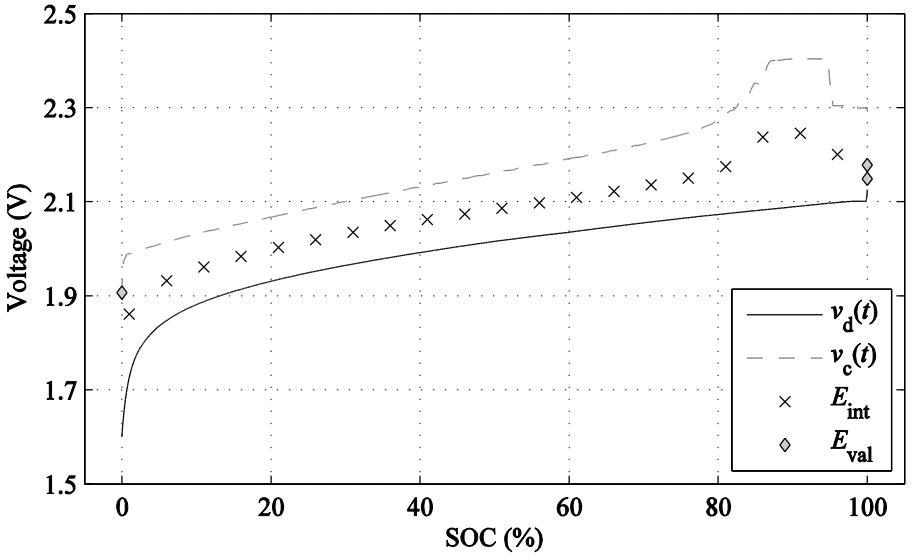

Figure 4-12: Linear interpolation for EMF characterization with SOC normalized to maximum discharge capacity (Rate: 0.05C, 25±1 °C)

Figure 4-13 contains the results from linear interpolation and linear extrapolation at the reduced rates. Observe that linear interpolation produced a single EMF curve (E_{int}) whereas linear extrapolation yielded two EMF curves – $E_{\text{d,ext}}$ valid for discharge and $E_{\text{c,ext}}$ valid for charge.

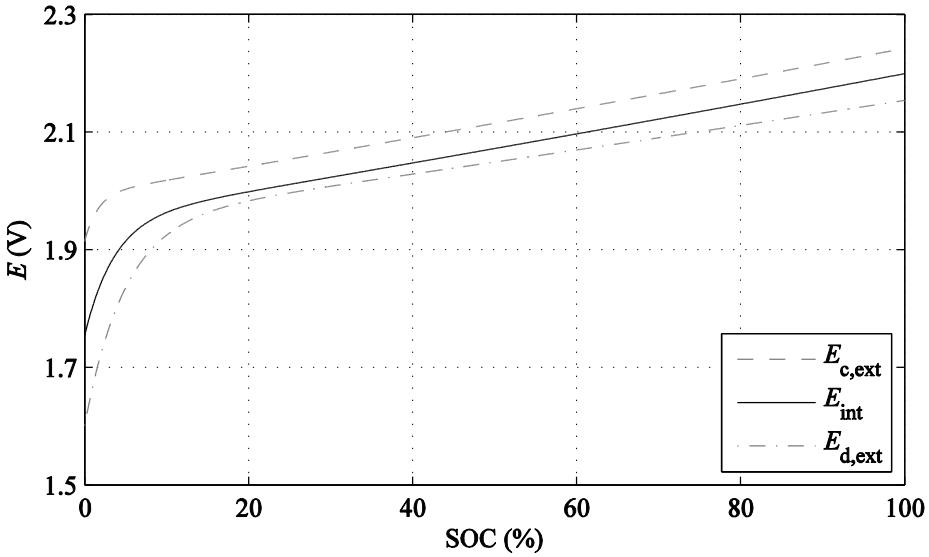

Figure 4-13: EMF curves using existing methods of interpolation and extrapolation at 25±1 °C (Rate: 0.04C, 0.02C)

Figure 4-14 shows the EMF curve obtained by the proposed method using the same 0.05C cycle data as in Figure 4-12. The values $E(m)$ are the EMF values calculated using the concentration-based method presented and explained earlier.

Clearly, CV charging does not produce the complications seen in the results from linear interpolation and linear extrapolation for EMF characterization.

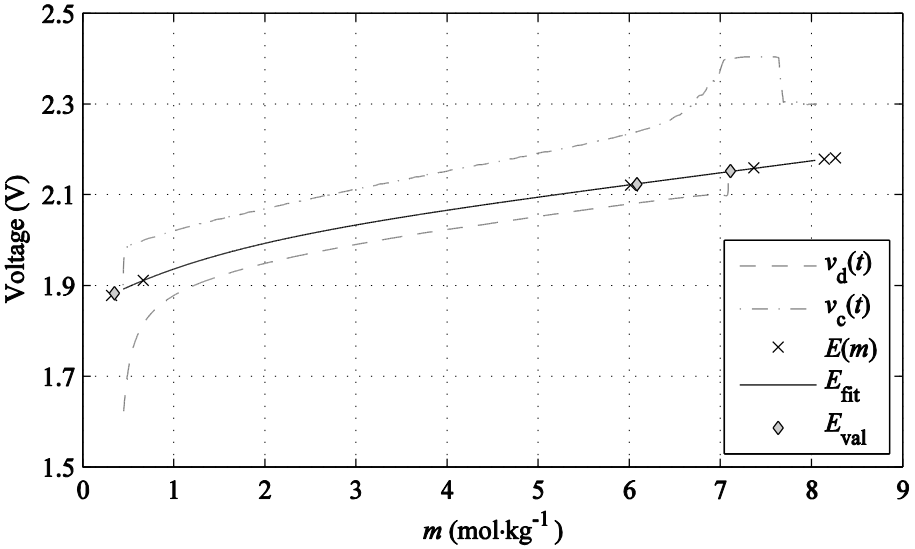

Figure 4-14: EMF as characterized by the concentration-based method (Rate: 0.05C)

The fitted curve (E_{fit}) compares well with the validation data (E_{val}) in Figure 4-14 but more quantitative measures are used to complete the validation of the concentration-based method. Table 4-1 shows the goodness-of-fit (GOF) statistics for each EMF characterization method applied in the current work. The statistics for linear extrapolation were calculated using both EMF curves, $E_{\text{d,ext}}$ and $E_{\text{c,ext}}$.

The sum of squares due to error (*sse*), the root mean squared error (*rmse*) and the R-square adjusted for degrees-of-freedom in the error (*rsq*) all indicate how well the resulting curves fit the data used in EMF characterization. The two bottom values, sse_V and $rmse_V$, are GOF statistics of the resulting curves when compared to validation data – data from cycles not used in the characterization phase.

Table 4-1: Goodness-of-fit statistics for EMF characterization methods

	Linear interpolation	*Linear extrapolation*	*Concentration-based*
sse	$1.58e^{-4}$	$1.56e^{-4}$	$1.12e^{-7}$
rmse	0.0035	0.0037	$2.37e^{-4}$
rsq	0.9987	0.9976	1
sse_V	0.0719	0.1491	$8.00e^{-6}$
$rmse_V$	0.0894	0.1322	0.0016

Linear interpolation and linear extrapolation do equally well until evaluated with validation data when linear interpolation clearly performs better. The concentration-based method from the current work produces better results than both linear interpolation and linear extrapolation.

To enable a visual comparison between the EMF curves from the existing methods and the proposed method, the EMF from concentration is plotted against SOC in Figure 4-15 and not against molality as done previously. Note that the interpolated EMF in this figure is the one obtained using very low rates for characterization to avoid CV charging complications.

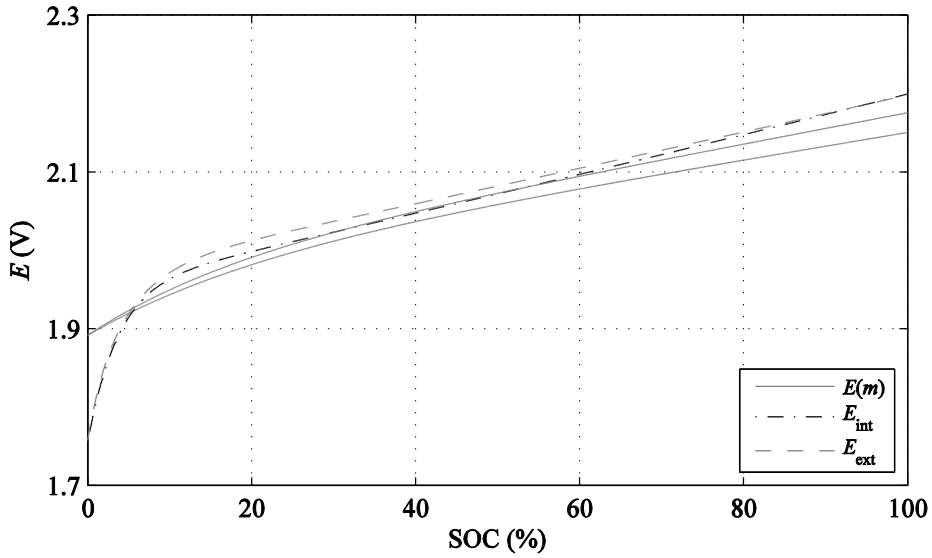

Figure 4-15: EMF curves from existing methods and concentration-based method against SOC normalized to the maximum discharge capacity

A hysteresis effect, as supported by literature [10], is clearly visible in the concentration-based EMF curve shown in Figure 4-15. The EMF-SOC relationship in lead-acid batteries is non-linear as reported by Waag [58], and the results in the current work corroborate the same conclusion.

A final validation result presents the EMF curve from the concentration-based characterization method used to model the EMF during charge and discharge in Figure 4-16. The measured EMF was obtained after resting and satisfying the threshold condition for OCV measurement as explained previously.

The modelled EMF using the concentration-based EMF curve coincides well with the measured EMF of the cells used for experimental data collection. This result indicates that the EMF curve might be used for concentration estimates in an online application. Experimental measurements of the cell's concentration against EMF will be required to fully explore this possible implementation.

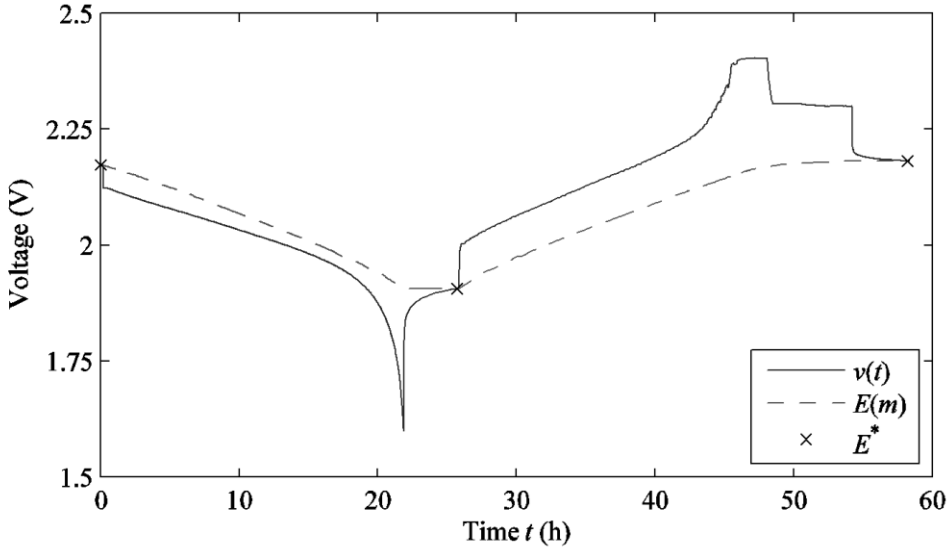

Figure 4-16: Modelled EMF during discharge and charge using EMF curve from concentration-based characterization method (Rate: 0.05C)

4.5 Conclusions

The aim of EMF characterization is to obtain representative information of a cell's behaviour during charge, discharge and rest. The methods used in this work – existing and new – do not require disassembling the cell and make use of macroscopic data in the form of terminal voltage, applied current and temperature measurements.

If the aim is to obtain a general impression of a cell's EMF and there are no time constraints, the existing methods for EMF characterization will suffice. For the purposes of this study, they did not provide an accurate enough picture of the cell's behaviour and an alternative method had to be devised.

The inspiration behind the concentration-based method for EMF characterization was presented and its implementation explained in detail. This method is not an attempt at SOC indication and does not employ SOC calculations for EMF characterization.

OCV measurements are used as the EMF of the cell to obtain estimates of the molality when the cell is at rest. The electric work done by the cell during operation is used to obtain the changes in molality which are then used with the Nernst equation to calculate the EMF during charge or discharge.

EMF characterization using the concentration-based method is verified using experimental data from single-cell VRLA batteries. Its EMF curve is compared to the EMF curves obtained from two existing characterization methods: linear interpolation and linear extrapolation. The results indicate a significant improvement in accuracy over existing methods and validate the proposed method.

Temperature effects on OCV measurements are also taken into account in the concentration-based method making it unnecessary for a temperature-controlled environment during the experiments. Experimental conditions during data collection for the concentration-based method varied between 10 and 30 °C. The key to the original method for EMF characterization presented in this chapter is based on the fact that molality does not depend on temperature.

The resulting curve of the lead-acid cell's EMF against estimated molality in Figure 4-11 is used in the following chapter during experimental validation of the multi-scale electrochemical model presented in Chapter 4.

5 PARAMETRIC ANALYSIS OF THE MULTI-SCALE MODEL

The multi-scale model's input parameters are subjected to analysis in this chapter. The initial set of parameters is discussed and details of the numerical solution are presented. The most uncertain parameters are used in elementary effects analysis by the Morris method to determine their rank in the multi-scale model. A final set of the most influential parameters is subjected to variance-based sensitivity analysis using a Monte Carlo experiment. Each parameter's first order and total sensitivity coefficients with respect to both the simulated cell voltage and the model error are obtained. The chapter is concluded with a summary of the qualitative and quantitative results which will be used for parameter estimation during model validation in the next chapter.

5.1 Model input parameters

The complete set of input parameters for the multi-scale electrochemical model presented in Chapter 3 can be seen divided into four columns in Table 5-1.

Table 5-1: Complete set of model input parameters for the multi-scale model

Parameter	*Count*	*Parameter*	*Count*	*Parameter*	*Count*	*Parameter*	*Count*
$a_{\max}$	2	exm	2	l	3	ρ_{M}	2
α_{a}	2	ε_0	2	$\mathrm{MW}_{\mathrm{Pb}}$	1	σ_{M}	2
α_{c}	2	$\varepsilon_{\max}$	2	$\mathrm{MW}_{\mathrm{PbO_2}}$	1	t_+^{o}	1
C_{dl}	2	$\varepsilon_{\mathrm{SEP}}$	1	$\mathrm{MW}_{\mathrm{PbSO_4}}$	2	T_{ref}	1
c_{ref}	1	γ	2	N	1	$\bar{V}_{\mathrm{e}}$	1
D	1	h	1	n	1	$\bar{V}_{\mathrm{o}}$	1
E_{A}	2	$i_{0,\mathrm{ref}}$	2	ρ_{Pb}	1	w	1
ex	3	κ	1	$\rho_{\mathrm{PbO_2}}$	1	ζ	2
Total:	**15**	*Total:*	**13**	*Total:*	**11**	*Total:*	**11**

Some of the input parameters are defined over more than a single domain of the model and require multiple parameter values to be determined. These multiple values are reflected in the *Count* column of each parameter. At the bottom of the table is the total count for each column, which all sum to a total of 50 parameter values required by the multi-scale model for simulation.

Many of these parameter values can either be measured, calculated or obtained from literature. The input space of the multi-scale model, as presented in Table 5-1, will now be reduced by fixing the least uncertain input parameters – the remaining parameters will be screened using elementary effects analysis (EEA) [86].

5.1.1 Design parameters

One of the single-cell VRLA batteries used for experimental data collection was disassembled for measurement of the internal components. The measurements were made using a digital vernier calliper with a precision of 10 μm. These measurements are grouped in Table 5-2 as the design parameters of the lead-acid cell. The design parameter values could also have been obtained from the manufacturer of the cell or battery under investigation.

Table 5-2: Measured design parameters for each domain of the lead-acid cell

Parameter	*Description*	*Unit*	d_1	d_2	d_3
h	Height of plate	mm		69	
l	Width of region	mm	1.7	1.3	1.15
N_{plates}	Total number of plates per cell	-		$5\ (2\times \text{PbO}_2,\ 3\times \text{Pb})$	
w	Plate width	mm		38.5	

5.1.2 Electrolyte material properties

The physical properties of H_2SO_4 diluted in water are commonly used for some of the model input parameters of the electrolyte. These physical properties, as listed in Table 5-3, are obtained from open literature, previous figures or equations shown in the *Source* column. The electrolyte conductivity κ has been calculated for $T_{\text{ref}} = 298.15\,\text{K}\ (25\ ^\circ\text{C})$ but in the multi-scale model it is calculated for other temperatures when necessary using (3.16).

The parameter c_{ref} refers to the electrolyte concentration of a fully charged cell at reference temperature and is typically calculated as 4.9e^{-3} mol/cm^3 for $T_{\text{ref}} = 298.15\,\text{K}\ (25\ ^\circ\text{C})$ using (3.23) [63]. This value is applicable to the electrolyte of vented designs.

The concentration in a VRLA cell with an AGM separator is usually higher. Other values found in literature for c_{ref} are 5.7e^{-3} mol/cm^3 [104] and 5.357e^{-3} mol/cm^3 or 6.23e^{-3} mol/cm^3 depending on the saturation of the separator [45].

Table 5-3: Electrolyte material properties for the multi-scale model

Parameter	*Description*	*Unit*	d_1, d_2, d_3	*Source*
c_{ref}	Reference concentration at 25 °C	mol/cm^3	6.16e^{-3}	Figure 4-11
κ	Electrolyte conductivity at 25 °C	S/cm	0.79	(3.16), [63]
$\bar{V}_{\text{e}}$	Partial molar volume of H_2SO_4	cm^3/mol	45	[63]
$\bar{V}_{\text{o}}$	Partial molar volume of H_2O	cm^3/mol	17.5	[63]

The value of c_{ref} in Table 5-3 was determined using the resulting curve of EMF against molality in Figure 4-11 from the concentration-based method for EMF characterization. This EMF curve is repeated in Figure 5-1. As given in the manufacturer's datasheet, the single-cell VRLA battery used in this study has $E_{\text{full}} = 2.19$ V at $T_{\text{ref}} = 298.15$ K (25 °C).

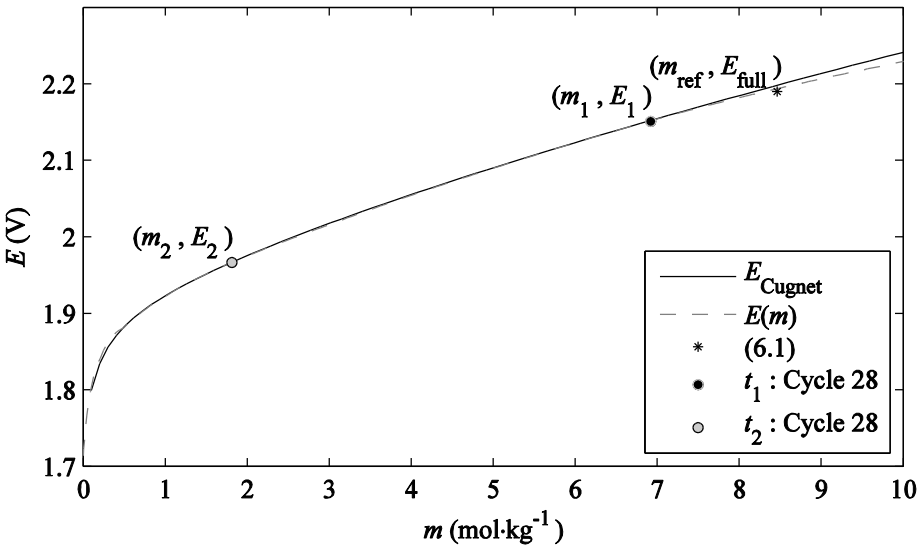

Figure 5-1: EMF curve from the concentration-based method used in the multi-scale model

Using $E_{\text{full}} = 2.19$ V on the curve, provides $m_{\text{ref}} = 8.32$ mol/kg as indicated. Eq. (3.39) is used to convert from molality (mol/kg) to molarity (mol/cm^3) and obtain the reference concentration for the VRLA cell used in this study as $c_{\text{ref}} = 6.16\text{e}^{-3}$ mol/cm^3.

A quick verification of $c_{\text{ref}} = 6.16\text{e}^{-3}$ mol/cm^3 is the popular empirical equation in the LAB industry to determine a fully charged cell's specific gravity (*SG*) [105]. This equation is given by:

$$SG = E_{\text{full}} - 0.84 \tag{5.1}$$

with E_{full} the cell's EMF when fully charged. Substitution in (5.1) with $E_{\text{full}} = 2.19$ V gives the *SG* in the following calculation:

$$SG = 2.19 - 0.84 = 1.34 \tag{5.2}$$

Tabular data by Linden [50] is used to convert this *SG* to molarity and the equivalent electrolyte concentration then becomes $c = 6.13\text{e}^{-3}$ mol/cm$^3 \approx c_{\text{ref}}$.

Also shown in Figure 5-1 are the points (m_1, E_1) and (m_2, E_2) with their values given by:

$$\begin{aligned} m_1 &= 6.920 \text{ mol/kg} \approx c_1 = 5.371\text{e}^{-3} \text{ mol/cm}^3,\ E_1 = 2.151 \text{ V} \\ m_2 &= 1.832 \text{ mol/kg} \approx c_2 = 1.710\text{e}^{-3} \text{ mol/cm}^3,\ E_2 = 1.967 \text{ V}. \end{aligned} \tag{5.3}$$

These values were obtained using experimental data from the 28$^{\text{th}}$ cycle of cell #3. The OCV at time instances t_1 and t_2 were recorded as E_1^* and E_2^* along with the temperature. These EMF values and temperature coefficients, as explained in Section 4.3, were employed to calculate E_1 and E_2 at T_{ref} and the respective molality estimates.

The molality estimates are m_1 and m_2 in Figure 5-1 and, along with $(m_{\text{ref}}, E_{\text{full}})$, provide some of the initial values for the electrolyte and EMF required by the multi-scale model for numerical solution.

5.1.3 Electrode material properties

Material properties for the electrodes and separator are also used for some of the model input parameters in the multi-scale model. Table 5-4 contains values for the porosities of both electrodes at full and empty states. The porosity values were measured experimentally by previous researchers as indicated in the *Source* column. It is possible to obtain a rough estimate of these values using the densities of Pb and PbO_2 if the pore space within the electrodes is accounted for [92].

The first uncertain parameter is σ_{PbO_2} or the electrical conductivity of the positive electrode material, emphasized by outline in Table 5-4. Various works report differing values for this parameter: 80 S/cm [63], 135 S/cm [106], 500 S/cm [32], [34]. As such, σ_{PbO_2} will be subjected to EEA to determine its rank within the multi-scale model.

Table 5-4: Electrode and separator material properties for the multi-scale model

Parameter	*Description*	*Unit*	d_1	d_2	d_3	*Source*
ε_0	Porosity at zero charge		0.3466		0.3066	[63]
ε_{max}	Porosity at full charge		0.53		0.53	[63]
ε_{SEP}	Porosity of separator			0.96		[45]
MW_{Pb}	Molecular weight of Pb	g/mol			207.2	[32]
MW_{PbO_2}	Molecular weight of PbO_2	g/mol	239.19			[32]
MW_{PbSO_4}	Molecular weight of $PbSO_4$	g/mol	303.3		303.3	[32]
ρ_{Pb}	Density of Pb	g/cm^3			11.34	[32]
ρ_{PbO_2}	Density of PbO_2	g/cm^3	9.7			[32]
ρ_{PbSO_4}	Density of $PbSO_4$	g/cm^3	6.3		6.3	[32]
σ_{Pb}	Conductivity of Pb at 25 °C	S/cm			$4.7e^4$	(3.48), [63]
$\boxed{\sigma_{PbO_2}}$	Conductivity of PbO_2	S/cm	80			[63], [71]

5.1.4 Parameters for species transport

The model input parameters applicable to the species transport equations can be found in Table 5-5. The acid diffusion coefficient *D* has been calculated for $T_{ref} = 298.15\,K$ (25 °C) but in the multi-scale model is calculated at other temperatures when necessary using (3.22).

Table 5-5: Parameters for species transport in the multi-scale model

Parameter	*Description*	*Unit*	d_1	d_2	d_3	*Source*
D	Acid diffusion coefficient at 25 °C	cm^2/s		$3.2e^{-5}$		(3.22), [63]
$\boxed{ex}$	Tortuosity correction in liquid phase		1.5	1.5	1.5	[63]
$\boxed{exm}$	Tortuosity correction in solid phase		0.5		0.5	[32]
t_+^o	Transference number of H^+			0.72		[34]

The values for the tortuosity correction parameters ex and exm in the different domains of the mult-scale model are those most used in previous modelling efforts but it is not clear exactly how they were chosen. For this reason, ex and exm will also be subjected to EEA to determine their influence as model input parameters.

5.1.5 Parameters for electrode kinetics

The parameters for electrode kinetics, as shown in Table 5-6, are difficult to determine even with specialized equipment [42]. A wide-spread practice consists of using parameter values from literature despite the significant uncertainty associated with these parameters [63]. The parameters for electrode kinetics outlined in Table 5-6 will be subjected to EEA in this study.

Table 5-6: Parameters for electrode kinetics in the multi-scale model

Parameter	*Description*	*Unit*	d_1	d_2	d_3	*Source*
a_{max}	Maximum active surface area	cm^2/cm^3	$2.3e^5$		$2.3e^4$	[34]
α_a	Anodic transfer coefficient	-	1.21		1.55	[32]
α_c	Cathodic transfer coefficient	-	0.79		0.45	[32]
C_{dl}	Double-layer capacitance	F/cm^2	$2e^{-5}$		$2e^{-5}$	[63]
E_A	Activation energy	J/mol	$5e^4$		$5e^4$	[63]
γ	Reaction order	-				[34]
$i_{0,ref}$	Transfer current density	A/cm^2	$9e^{-7}$		$9e^{-6}$	[34]
n	Number of electrons involved	mol		2		[63]
ζ	Morphology parameter	-	1.5		1.5	[32]

The cathodic transfer coefficient (α_c) for both electrode domains is easily calculated using:

$$\alpha_c = n - \alpha_a = 2 - \alpha_a \tag{5.4}$$

Only the values for the anodic transfer coefficient (α_a) have to be determined [32]. For this reason, α_c will not be subjected to further analysis.

5.2 Numerical solution of the multi-scale model

The sets of partial differential equations, consisting of the governing equations and boundary conditions for the multi-scale model, were programmed in COMSOL Multiphysics®.

5.2.1 Initial values

The initial value for the electrolyte concentration and the cell's EMF were explained in Section 0. The electrolyte concentration is initially considered to be uniform throughout the cell because the cell is fully relaxed. Other initial conditions were chosen to represent a lead-acid cell at the beginning of discharge with full capacity available. The porosity is also considered initially uniform throughout each electrode.

The reference electrode is selected as a concentration-independent Pb electrode. As such, the initial solid potential of the positive electrode is the measured EMF of the cell at the start of discharge. The negative electrode has a solid potential of 0 V. The solid potential does not exist in the separator region and all other initial values are calculated by the solver.

5.2.2 Model verification

The multi-scale model is used to simulate a 0.1C discharge of the VRLA cell to a COV of 1.7 V. The cell is then allowed to rest for 4 hours and a constant-current charge also at 0.1C starts. The simulated and measured cell voltages are shown in Figure 5-2.

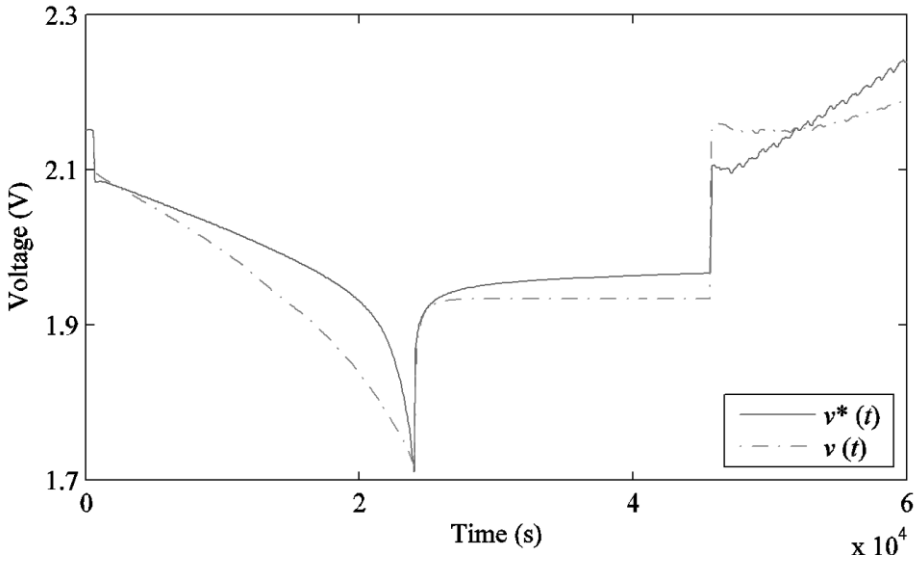

Figure 5-2: Simulated and measured voltage of a VRLA cell with an immobile electrolyte

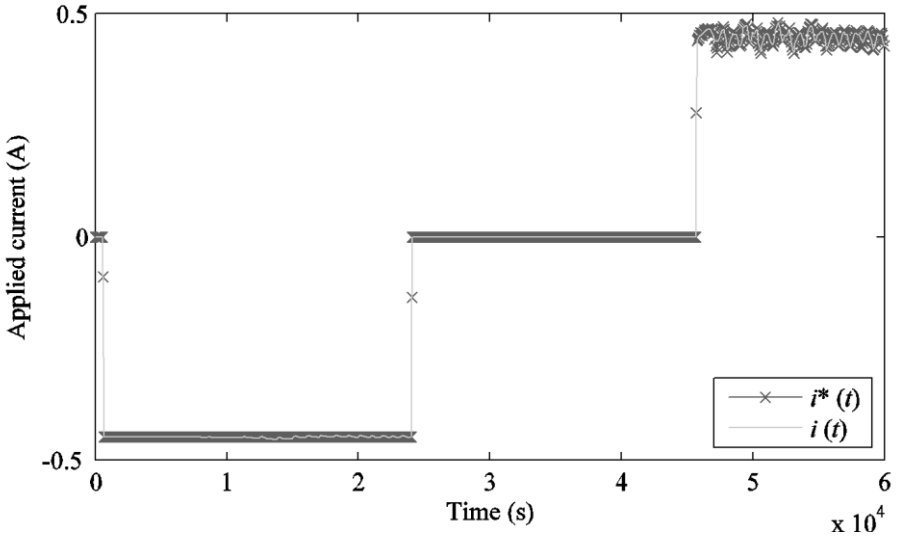

Figure 5-3: Simulated and measured current applied to the lead-acid cell at 0.1C

The applied current as measured during the discharge/charge cycle in Figure 5-2, is shown Figure 5-3 along with the simulated current. The simulated electrolyte concentration is illustrated Figure 5-4 in time and over the different regions of the lead-acid cell as indicated by the boundaries. The concentration decreases as the cell discharges and then increases again during the subsequent charge.

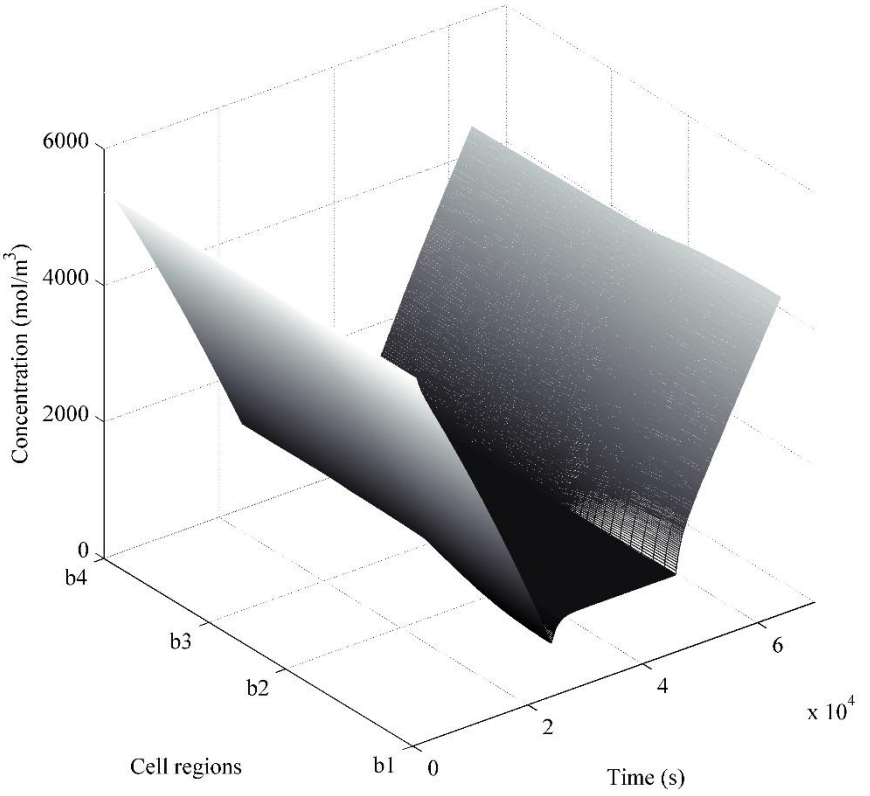

Figure 5-4: Simulated electrolyte concentration in the lead-acid cell regions over time

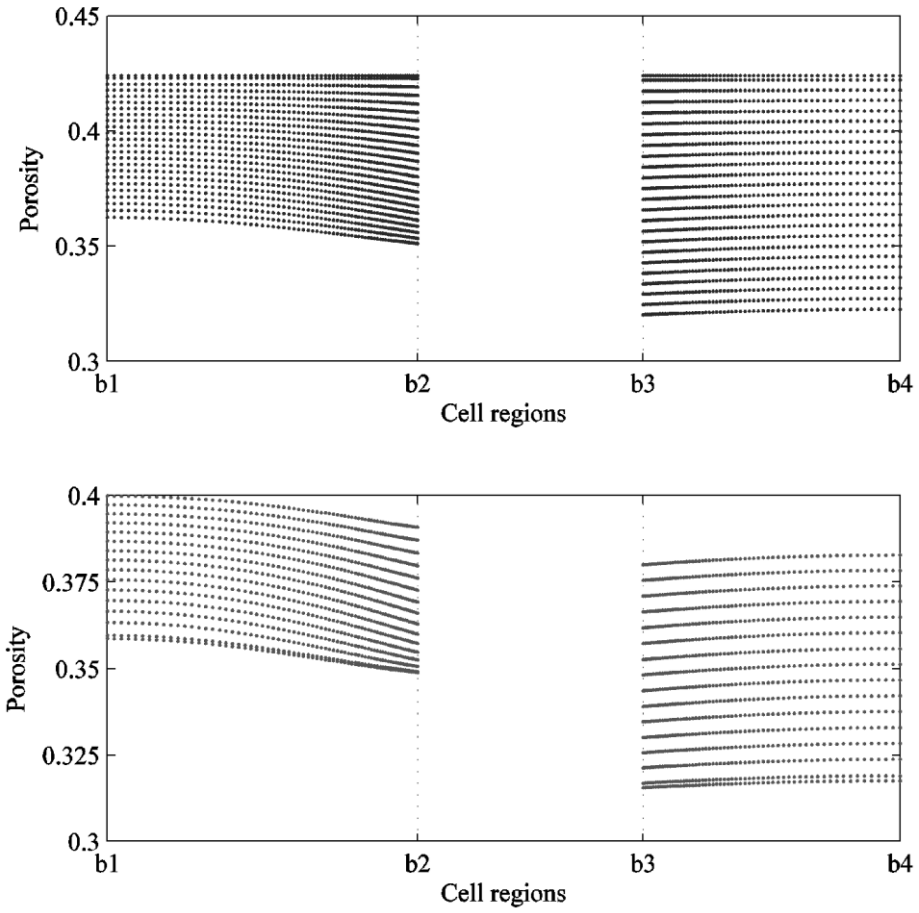

Figure 5-5: Electrode porosities during discharge (top) and charge (bottom)

The porosities of both electrodes during this cycle are shown in Figure 5-5 as they decrease during discharge from a uniform starting point and then increase during charge. The preceding figures indicate that the simulated lead-acid cell behaves as it should during discharge, rest and charge. The electrodes and electrolyte also respond correctly to the applied current. As such, the multi-scale model is verified.

5.2.3 Experimental setup

Since the applied current and temperature used in the simulation are the actual measured current and temperature, the experimental setup for data collection is now explained.

Single-cell VRLA batteries were used in the current work to eliminate the effects of cell-to-cell variations. Eight 2 V batteries with absorbed glass mat (AGM) separator rated at 4.5 Ah over 20 hours (Graupner-793) were cycled to obtain the experimental data. The UBA5 from Vencon Technologies was used for charging and discharging at various rates while recording the terminal voltage, applied current and temperature. Upon receipt from the manufacturer, each battery was fully cycled at least twice using recommended rates to ensure all the batteries were more or less in the same state.

5.3 Elementary effects analysis using simulated cell voltage

The results of the previous sections are used to obtain a reduced set of input parameters which will be used in elementary effects analysis. The parameters $a_{\max}$ and $i_{0,\mathrm{ref}}$ occur as a product in the multi-scale electrochemical model's equations. This product ($a_{\max} i_{0,\mathrm{ref}}$) is the effective exchange current density and will be used as a model input parameter instead of the two separate parameters [92].

The complete set for elementary effects analysis has a total count of 18 uncertain parameters as shown in Table 5-7. At this point, the model input space consists of $k = 18$ dimensions. Exploring this space using a typical 2-level factorial design would result in $N = p^k = 2^{18} = 2.62144\mathrm{e}^5$ model evaluations with *p* the number of levels [107]. A screening method with a small number of model evaluations is required to determine the most influential parameters.

Table 5-7: Model input parameters for elementary effects analysis

Parameter	*Unit*	*Nominal*	*Interval*	*Count*
$a_{\max} i_{0,\mathrm{ref}}$	$\mathrm{A/cm^3}$	0.02	(0.01,0.1)	2
α_{a}	-	1	(0.4,1.6)	2
C_{dl}	$\mathrm{F/cm^2}$	$8\mathrm{e}^{-5}$	$(2\mathrm{e}^{-5}, 14\mathrm{e}^{-5})$	2
E_{A}	J/mol	$6\mathrm{e}^4$	$(5\mathrm{e}^4, 7\mathrm{e}^4)$	2
ex	-	1.5	(1.2,1.8)	3
exm	-	0.5	(0.4,0.6)	2
γ	-	1	(0,3)	2
$\sigma_{\mathrm{PbO_2}}$	S/cm	100	(50,200)	1
ζ	-	1.5	(0.1,3)	2
			Total:	**18**

5.3.1 The Morris method

The aim of elementary effects analysis (EEA) by Morris is to design a computationally inexpensive experiment requiring only a small number of model evaluations [88]. The results are of a qualitative nature and are used to fix the least influential parameters whilst obtaining a set of the most important parameters [86]. The most important parameters are then used in variance-based model sensitivity analysis.

The model input parameters are $X_1, X_2, \ldots, X_k = \mathbf{X}$ with k the dimensions of the input space wherein each X_i can assume values on the set $\{0, 1/(p-1), 2/(p-1), \ldots, 1\}$. The region of experimentation Ω is a k-dimensional p-level grid with a sample point in this region denoted by $\mathbf{x} = (x_1, x_2, \ldots, x_k)$. Actual parameter values for model evaluation are obtained by scaling the normalized values with a parameter's maximum and minimum bounds. The total number of model evaulations is denoted by N and the model output of an evaluation is denoted by $y(\mathbf{x})$ with $\mathbf{x}$ a sample point.

The Morris method for EEA is based on exploring the input space using multiple sample trajectories. Each trajectory contains $k+1$ sample points denoted by the following:

$$\mathbf{x}^{(1)}, \mathbf{x}^{(2)}, \ldots, \mathbf{x}^{(k+1)} \tag{5.5}$$

The model is evaluated at these sample points using an orientation matrix $\mathbf{B}^* : (k+1) \times k$. Consider the $k = 3$ parameter input space and a single sample trajectory in Figure 5-6. In this example, the total number of model evaluations is $N = k+1 = 4$ which is quite small. Of course, the input space is not even close to sufficiently explored using a single trajectory. Using multiple trajectories r results in:

$$N = r(k+1) \tag{5.6}$$

The number of model evaluations for the Morris method are linear in the number of input parameters. Morris suggests using a base value from which to randomly sample the starting point $\mathbf{x}^{(1)}$ of each trajectory. This base value $\mathbf{x}^*$ is also randomly sampled from Ω but it is never used for model evaluation.

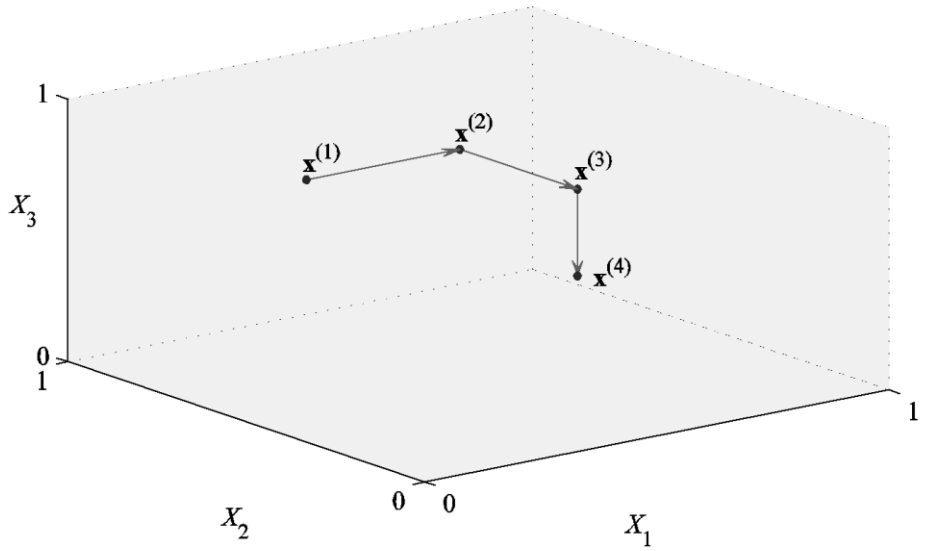

Figure 5-6: Single sample trajectory in parameter input space for Morris method

Elementary effects analysis using the Morris method can only be regarded as a global sensitivity analysis method if multiple trajectories $(r \geq 10)$ are used [87]. Other recommendations include setting the number of levels $p = 4$ and choosing a constant step magnitude Δ as:

$$\Delta = p/[2(p-1)] \tag{5.7}$$

with which to move from one sample point to the next in the input space. To obtain the second sample point $\mathbf{x}^{(2)}$ in a trajectory, $\mathbf{x}_k^{(1)}$ is used as given by:

$$\mathbf{x}^{(2)} = \left(x_1^{(1)},\ldots,x_{i-1}^{(1)},x_i^{(1)} \pm \Delta, x_{i+1}^{(1)},\ldots,x_k^{(1)}\right) = \left(\mathbf{x}_k^{(1)} \pm \mathbf{e}_i\Delta\right) \tag{5.8}$$

where $\mathbf{e}_i$ is a vector of zeros except for the *i*-th component, which is 1. For the $k = 3$ example in Figure 5-6, the orientation matrix $\mathbf{B}^* : (k+1)\times k$ for a single trajectory is shown in Table 5-8. Note that *i* was chosen as 1,2,3 for this example but should be selected randomly from the set $\{1,2,\ldots,k\}$.

Table 5-8: Orientation matrix for *k* = 3 of a single sample trajectory for Morris method

	x_1	x_2	x_3	*Step*
$\mathbf{x}^{(1)}$	0.00	1.00	1.00	-
$\mathbf{x}^{(2)}$	0.67	1.00	1.00	$x_1^{(1)} + \Delta$
$\mathbf{x}^{(3)}$	0.67	0.33	1.00	$x_2^{(2)} - \Delta$
$\mathbf{x}^{(4)}$	0.67	0.33	0.33	$x_3^{(3)} - \Delta$

The orientation matrix $\mathbf{B}^*$ is generated *r* times for a total of *r* different trajectories exploring the input space. Each $\mathbf{B}^*$ provides a single EE per input parameter. Further details on calculation and implementation of the Morris method can be found in [87].

As the model is evaluated at $k+1$ sample points, an elementary effect d_i for each parameter X_i is computed. Consider points $\mathbf{x}^{(l)}$ and $\mathbf{x}^{(l+1)}$ with *l* in the set $\{1,2,\ldots,k\}$ as two sample points differing only in their *i*-th component. If this difference is an increment of Δ, the elementary effect d_i for parameter X_i is calculated using:

$$d_i\left(\mathbf{x}^{(l)}\right) = \frac{\left[y\left(\mathbf{x}^{(l+1)}\right) - y\left(\mathbf{x}^{(l)}\right)\right]}{\Delta} \tag{5.9}$$

For a decrease by Δ, d_i is given by:

$$d_i\left(\mathbf{x}^{(l)}\right) = \frac{\left[y\left(\mathbf{x}^{(l)}\right) - y\left(\mathbf{x}^{(l+1)}\right)\right]}{\Delta} \tag{5.10}$$

with $y\left(\mathbf{x}^{(l)}\right)$ and $y\left(\mathbf{x}^{(l+1)}\right)$ the model outputs evaluated at sample points $\mathbf{x}^{(l)}$ and $\mathbf{x}^{(l+1)}$. The model output of interest during EEA is the simulated cell voltage, $v(t)$. Using the elementary effects (d_i), the first Morris sensitivity measure (μ) for parameter X_i is calculated as:

$$\mu = \sum_{i=1}^{r} d_i / r, \quad \mu^* = |\mu| \tag{5.11}$$

with μ called the overall effect of the parameter X_i on the model output. The second Morris sensitivity measure (σ) for parameter X_i is given by:

$$\sigma = \sqrt{\sum_{i=1}^{r} (d_i - \mu)^2 / r} \tag{5.12}$$

which is an indication of interaction and/or nonlinear effects. The absolute value of μ, denoted as μ^*, may be used by itself to obtain a ranking of the input parameters but μ and σ should always be used together to analyze elementary effects [87].

5.3.2 Results of EEA of the multi-scale model

For $k = 18$ input parameters and setting $p = 4$ and $r = 10$ in (5.6), the number of model evaluations are:

$$N = r(k+1) = 10 \cdot 19 = 190 \tag{5.13}$$

The orientation matrix $\mathbf{B}^*$ is generated $r = 10$ times in MATLAB® and the model evaluated using the sample points in COMSOL Multiphysics®. The simulated cell voltage, $v(t)$, during each of these evaluations is shown in Figure 5-7 along with the measured cell voltage, $v^*(t)$.

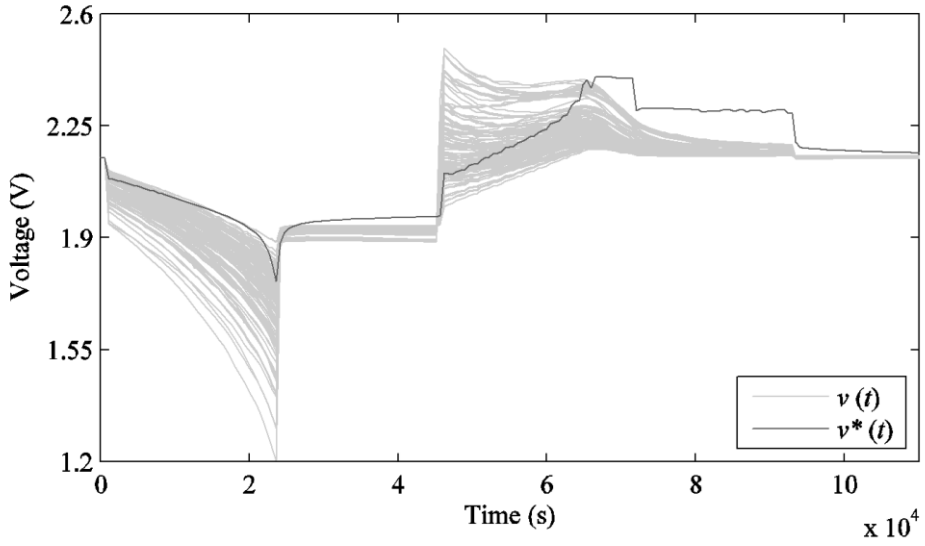

Figure 5-7: Simulated cell voltages of *N* = 190 for EEA using the Morris method

The simulated cell voltage was obtained using the multi-scale model with the current and temperature over time set equal to the measured current and temperature of the experimental voltage. Notice that the voltage profiles in Figure 5-7 contain the cell's behaviour for discharge, charge and multiple rest periods.

With the help of (5.9)-(5.12) programmed in MATLAB®, 10 elementary effects for each parameter were calculated. The elementary effects for each parameter X_i are shown in the box plot of Figure 5-8 and the mean of each set corresponds to the first Morris sensitivity measure, μ. The box plot seems to indicate that the parameters above ex for the positive electrode have the most significant effect on the multi-scale model's simulated cell voltage.

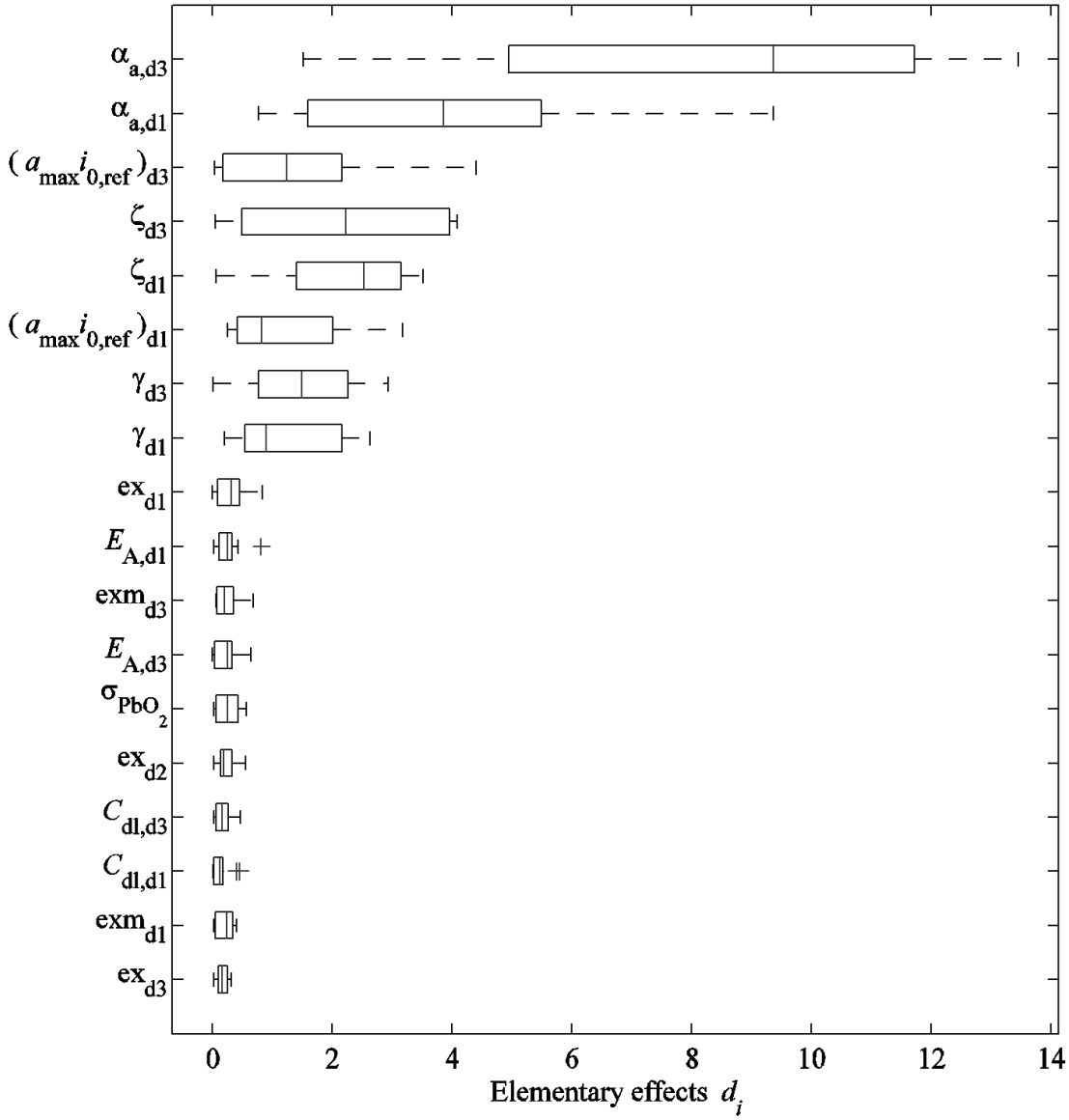

Figure 5-8: Box plot of elementary effects on the simulated cell voltage for *k* = 18 parameters

Because the multi-scale model does not rely on isothermal conditions, it was initially suspected that the activation energies for both the positive and negative electrode would have a bigger impact [60]. The results in Figure 5-8 indicate that their elementary effects are not significant at all. To verify this, the Morris sensitivity measures μ^* and σ for each parameter were also calculated because μ should never be used on its own to determine the rank of a parameter [87]. Figure 5-9 shows the resulting plot of both Morris measures.

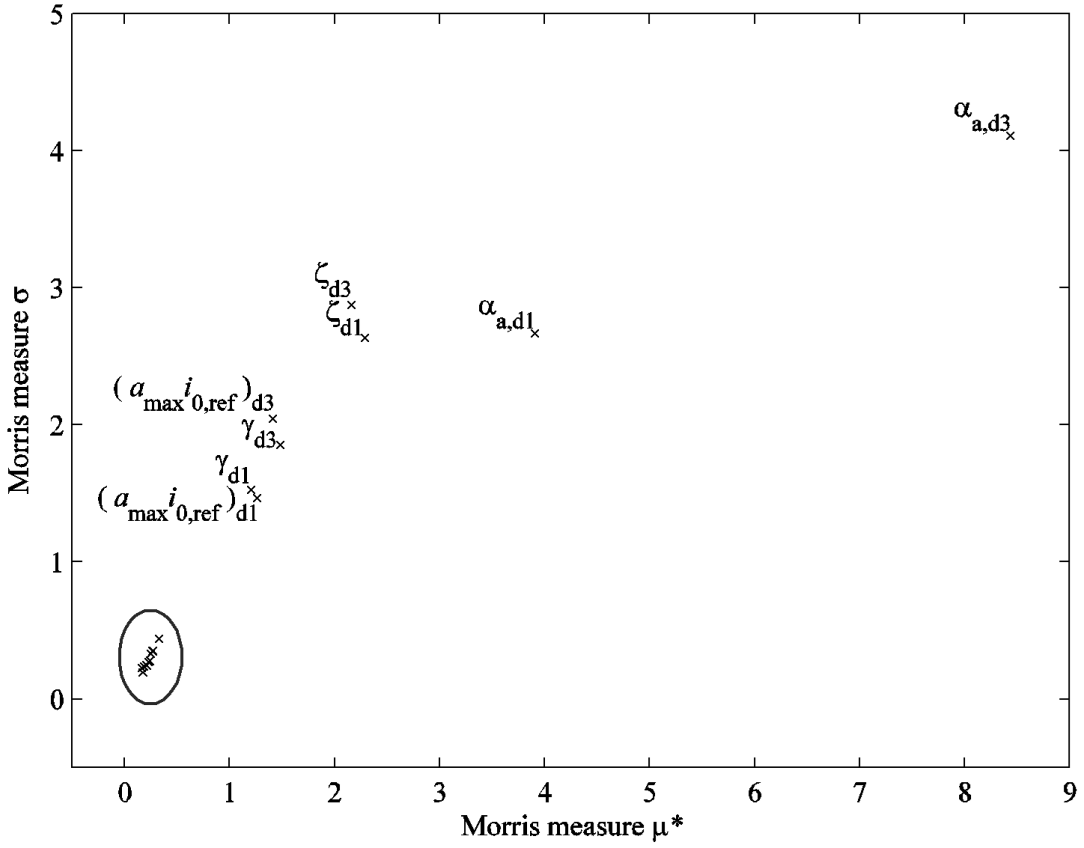

Figure 5-9: Morris sensitivity measures for elementary effects analysis

The least influential parameters have Morris measures spaced so close together that they are difficult to label in Figure 5-9. Instead, they are circled and suggest the same conclusion as Figure 5-8: parameters $\alpha_a, a_{max} i_{0,ref}$, γ and ζ are the most influential parameters. This set will now be explored in depth to obtain recommendations for parameter estimation [87].

5.4 Variance-based sensitivity analysis using experimental data

The major difference between elementary effects analysis and variance-based sensitivity analysis is in the nature of the results. EEA produces a qualitative impression of the importance of parameters but cannot indicate exactly how much more important one parameter is than another.

For screening purposes, EEA is a practical method due to the small number of model evaluations required. Variance-based sensitivity analysis (VBSA) is a more informative parametric analysis with quantitative results. Table 5-9 contains the most important parameters determined during EEA.

Table 5-9: Model input parameters for variance-based sensitivity analysis

Parameter	*Unit*	*Nominal*	*Interval*	*Count*
$a_{\max} i_{0,\mathrm{ref}}$	$\mathrm{A/cm^3}$	0.02	$(0.01, 0.1)$	2
α_{a}	-	1	$(0.4, 1.6)$	2
γ	-	1	$(0, 3)$	2
ζ	-	1.5	$(0.1, 3)$	2
			Total:	**8**

The dimensions of the input space at this point is $k = 8$ with the nominal values and interval of each parameter the same as during elementary effects analysis. A Monte Carlo experiment will be used to explore this much smaller input space. The resulting model evaluations are used to decompose the variance in the output of interest, using formulae with similarities in analysis-of-variance (ANOVA) techniques [108].

5.4.1 A Monte Carlo experiment and Jansen's formulae

The input space is sampled in a random manner for a typical Monte Carlo experiment. On the other hand, VBSA requires the input space to be sampled as uniformly as possible over a unit hypercube. Quasi-random (QR) number sequences are able to satisfy the requirements of a Monte Carlo experiment and VBSA.

In QR sampling, each point knows about the position of previous sample points and the aim is to fill the gaps between samples as efficiently as possible. QR sampling ensures a smaller number of model evaluations than pseudo-random sampling [90]. Combining QR sampling in a Monte Carlo experiment is sometimes called a quasi Monte Carlo approach [108].

The Monte Carlo experiment in this work therefore actually consists of Monte Carlo simulations using QR samples of the multi-scale model's input space. The input space under consideration in VBSA is smaller than the input space for EEA but it is more thoroughly explored. In the Monte Carlo experiment for VBSA, each parameter is sampled from its distribution.

For decomposition of the variance, Jansen's formulae [91] are used because they are recommended for the problem under consideration [108]. These formulae require a triplet of sample matrices denoted as $\mathbf{A}$, $\mathbf{B}$ and $\mathbf{A}_{\mathbf{B}}^{(i)}$ with I again in the set $\{1,2,\ldots,k\}$. The model output of interest is denoted as $\Upsilon = f(X_i)$ and may be a simulated variable or an objective function which compares the simulated variable with experimental data. The number of Monte Carlo simulations is denoted by N_{MC} and the total number of model evaluations is *N*.

A matrix $\mathbf{M}$ of size $N_{\mathrm{MC}} \times 2k$ contains parameter values randomly sampled from the region of experimentation, Ω. The left half of $\mathbf{M}$ is the matrix $\mathbf{A}$ with size $N_{\mathrm{MC}} \times k$ and the right half of $\mathbf{M}$ is matrix $\mathbf{B}$ with size $N_{\mathrm{MC}} \times k$. An element of **A** or **B** is denoted as a_{ji} or b_{ji} with *j* the row number and *I* the column number of matrix **A** or **B**. The row number will be in the set $\{1,2,\ldots,N_{\mathrm{MC}}\}$.

Finally, matrix $\mathbf{A}_{\mathbf{B}}^{(i)}$ is a matrix with all the columns from **A** except the *i*-th column, which is from **B**. The total number of model evaluations for the Monte Carlo experiment is calculated using:

$$N = N_{\mathrm{MC}}(1 + k/2) \tag{5.14}$$

with *k* the number of model input parameters [108]. The next step is to compute the model output of interest, Υ, at each of the samples in $\mathbf{A}$, $\mathbf{B}$ and $\mathbf{A}_{\mathbf{B}}^{(i)}$.

The variance-based first order effect for parameter X_i is calculated as:

$$\mathrm{var}_{X_i}\left[\mathrm{E}_{\mathbf{X}_{\sim i}}(\Upsilon \mid X_i)\right] = \mathrm{var}(\Upsilon) - \frac{1}{2N_{\mathrm{MC}}}\sum_{j=1}^{N_{\mathrm{MC}}}\left[f(\mathbf{B})_j - f\left(\mathbf{A}_{\mathbf{B}}^{(i)}\right)_j\right]^2 \tag{5.15}$$

with $\mathrm{var}(\cdot)$ the variance operator and $\mathrm{E}(\cdot)$ the expectation (mean) operator [91].

The notation $\mathbf{X}_{\sim i}$ is used to indicate all parameters but the *i*-th parameter. The inner mean calculation $\mathrm{E}_{\mathbf{X}_{\sim i}}(\Upsilon \mid X_i)$ is explained as the mean of the output over all possible parameter values of $\mathbf{X}_{\sim i}$ while keeping the *i*-th parameter fixed. The outer variance calculation $\mathrm{var}_{X_i}(\cdot)$ is explained as the variance of the argument taken over all possible values of the *i*-th parameter.

The model outputs used by the sum operator in (5.15) are:

$$f(\mathbf{B})_j = f(b_{j1}, b_{j2}, \ldots b_{jk}), \quad f\left(\mathbf{A}_{\mathbf{B}}^{(i)}\right)_j = f(a_{j1}, \ldots, b_{ji}, \ldots a_{jk}) \tag{5.16}$$

The first-order sensitivity coefficient for parameter X_i is calculated using:

$$S_i(\Upsilon) = \frac{\mathrm{var}_{X_i}\left[\mathrm{E}_{\mathbf{X}_{\sim i}}(\Upsilon \mid X_i)\right]}{\mathrm{var}(\Upsilon)} \tag{5.17}$$

wherein $\mathrm{var}(\Upsilon)$ is used for normalization of the value obtained from (5.15).

The variance-based sensitivitiy measure for the total effect of X_i is given by:

$$\mathrm{E}_{\mathbf{X}_{\sim i}}\left[\mathrm{var}_{X_i}\left(\Upsilon \mid \mathbf{X}_{\sim i}\right)\right] = \frac{1}{2N_{\mathrm{MC}}}\sum_{j=1}^{N_{\mathrm{MC}}}\left[f\left(\mathbf{A}\right)_j - f\left(\mathbf{A}_{\mathbf{B}}^{(i)}\right)_j \right]^2 \tag{5.18}$$

with the inner variance calculation $\mathrm{var}_{X_i}\left(\Upsilon \mid \mathbf{X}_{\sim i}\right)$ explained as the variance of the output over all possible parameter values of X_i while keeping the rest fixed [91]. The outer mean calculation $\mathrm{E}_{\mathbf{X}_{\sim i}}\left(\cdot\right)$ is explained as the mean of the argument taken over all possible parameter values of $\mathbf{X}_{\sim i}$.

The model outputs used by the sum operator in (5.18) are:

$$f\left(\mathbf{A}\right)_j = f\left(a_{j1}, a_{j2}, \ldots a_{jk}\right), \quad f\left(\mathbf{A}_{\mathbf{B}}^{(i)}\right)_j = f\left(a_{j1}, \ldots, b_{ji}, \ldots a_{jk}\right) \tag{5.19}$$

The total sensitivity coefficient for parameter X_i is given by:

$$S_{Ti}\left(\Upsilon\right) = \frac{\mathrm{E}_{\mathbf{X}_{\sim i}}\left[\mathrm{var}_{X_i}\left(\Upsilon \mid \mathbf{X}_{\sim i}\right)\right]}{\mathrm{var}\left(\Upsilon\right)} = 1 - \frac{\mathrm{var}_{\mathbf{X}_{\sim i}}\left[\mathrm{E}_{X_i}\left(\Upsilon \mid \mathbf{X}_{\sim i}\right)\right]}{\mathrm{var}\left(\Upsilon\right)} \tag{5.20}$$

wherein $\mathrm{var}\left(\Upsilon\right)$ is again used for normalizaiton of the value obtained from (5.18).

5.4.2 Results of VBSA

For $k = 8$ input parameters and setting $N_{\mathrm{MC}} = 60$ in (5.14), the total number of model evaluations are:

$$N = N_{\mathrm{MC}}\left(1 + k/2\right) = 60\left(1 + 8/2\right) = 300 \tag{5.21}$$

The triplet **A**, **B** and $\mathbf{A}_{\mathbf{B}}^{(i)}$ is generated in MATLAB® using the latin hypercube design which is a QR sampling method. The sample matrices are then used to evaluate the model in COMSOL Multiphysics®. A scatter plot of the model input parameter values from the triplet of sample matrices can be seen in Figure 5-10.

The output of interest for a single evaluation of the multi-scale model consists not only of $v(t)$ but also of the sum of the model error squared, *sse*(*t*). The sum of the model error squared is calculated as:

$$sse(t) = \sum_{g=1}^{t}\left[v^*(g) - v(g)\right]^2 \tag{5.22}$$

and will be denoted by f_{sse}. Similarly, $v(t)$ will be denoted as f_v. The resulting sensitivity coeffcients are then $S_i\left(f_v\right)$, $S_{Ti}\left(f_v\right)$ for the simulated cell voltage and $S_i\left(f_{sse}\right)$, $S_{Ti}\left(f_{sse}\right)$ for the sum of the model error squared.

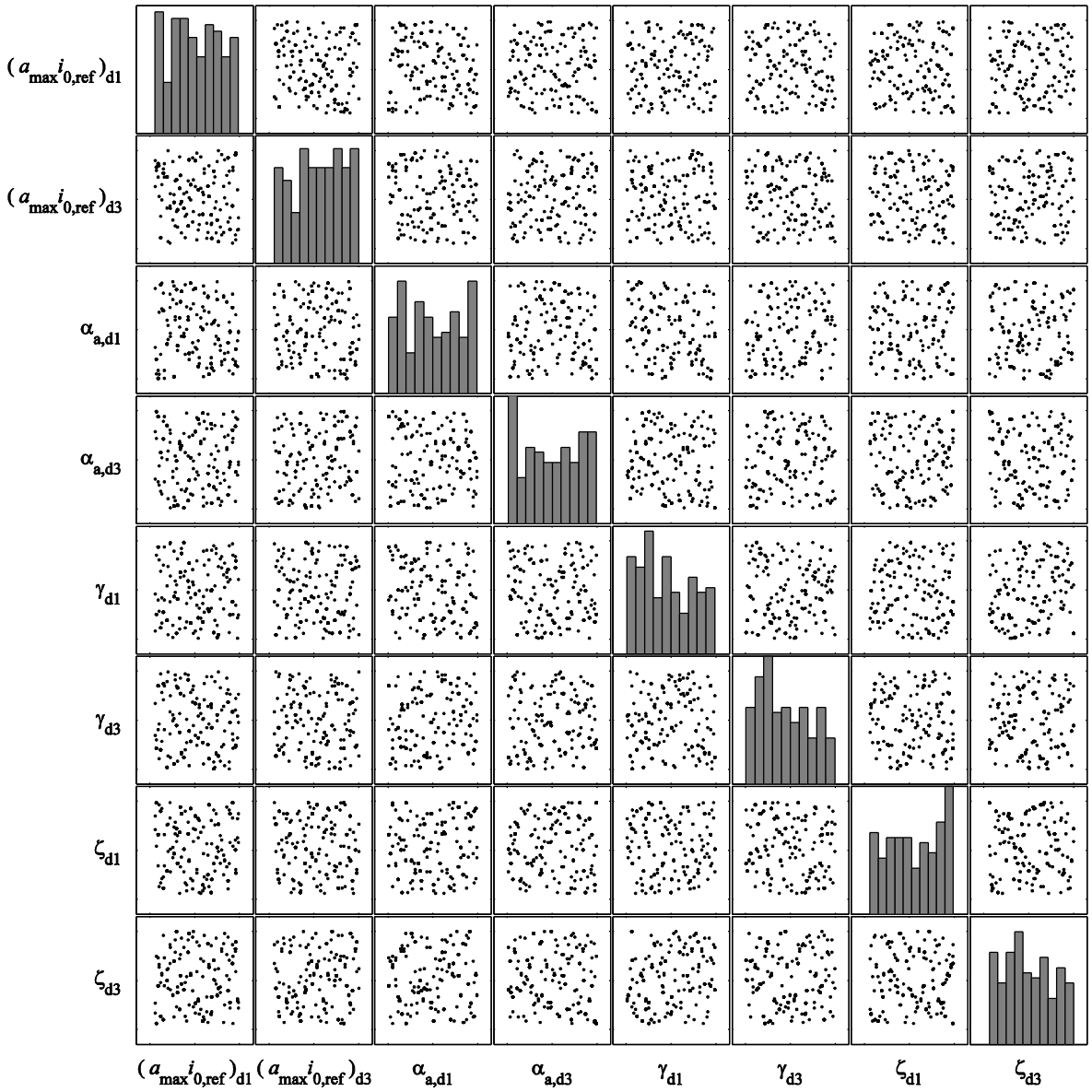

Figure 5-10: Scatter plot of QR samples in the input space for Monte Carlo experiment

The simulated cell voltage, $v(t)$, at time instant t = 120 s for $N = 300$ model evaluations against the sampled parameter values can be seen in Figure 5-11. A single instant in time of $v(t)$ is shown and it is not possible at this point to conclude anything useful in terms of parameter values.

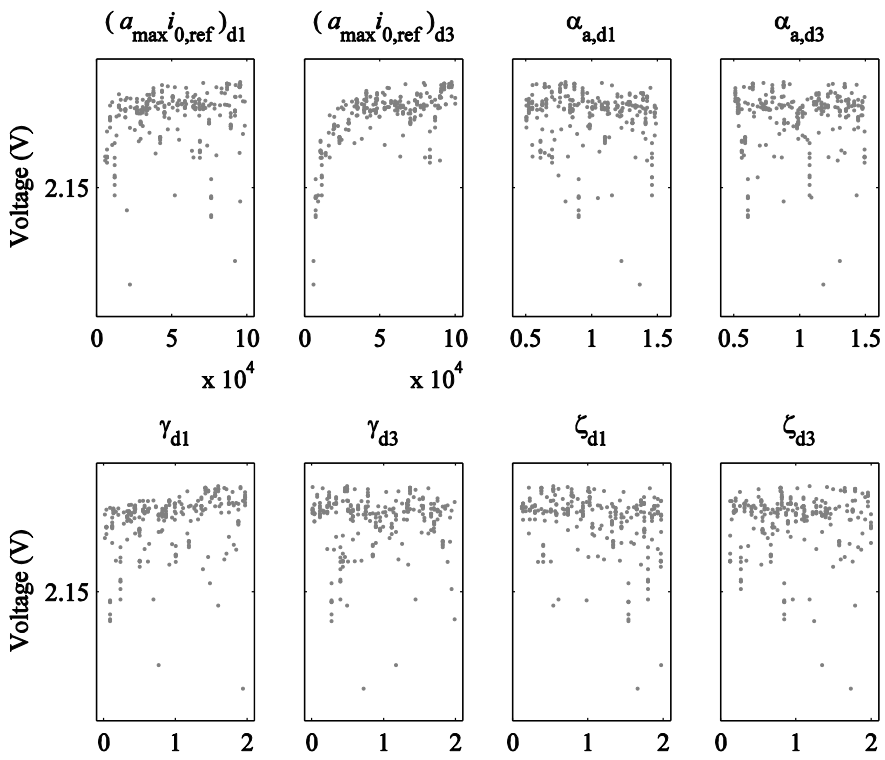

Figure 5-11: Simulated cell voltages at *t* = 120 s against sampled parameter values

The simulated cell voltage, $v(t)$, from the $N = 300$ model evaluations as well as the measured cell voltage, $v^*(t)$, can be seen in Figure 5-12. To make some sense of the relationship between the model's input parameters and its output, the sensistivity coefficients are calculated.

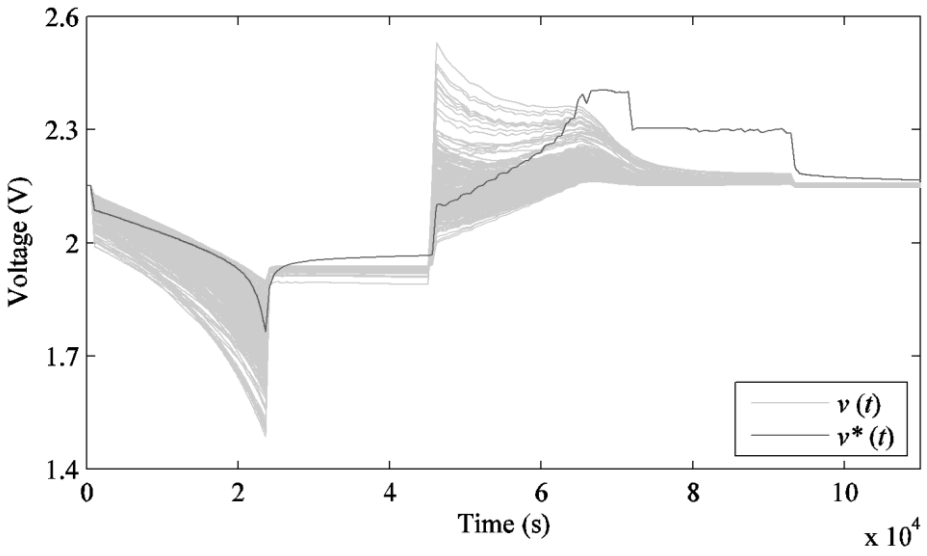

Figure 5-12: Simulated cell voltages from Monte Carlo experiment and measured cell voltage against time

The first calculation is the first-order sensitivity coefficients of the parameter effects on the simulated cell voltage, $S_i(f_v)$, using (5.17). Since this model output is a vector of the cell voltage as it changes, the first-order sensitivity is shown in Figure 5-13 against time.

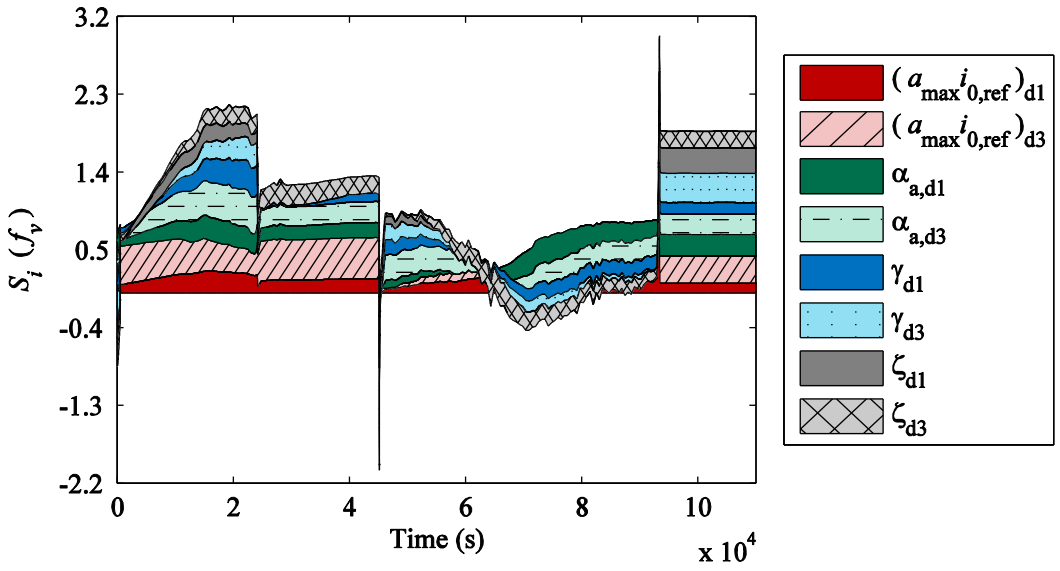

Figure 5-13: Area plot of the first-order sensitivity of simulated cell voltage over time

An interesting observation from Figure 5-13 is that no single parameter is the most influential all the time. During discharge, the effective exchange current density of the both electrodes and both anodic transfer coefficients are very influential. When discharge ends and the cell's voltage relaxes, the reaction order of both electrodes have almost no impact on the output. Figure 5-14 shows the period in time when discharge starts and the cell is not at rest any more.

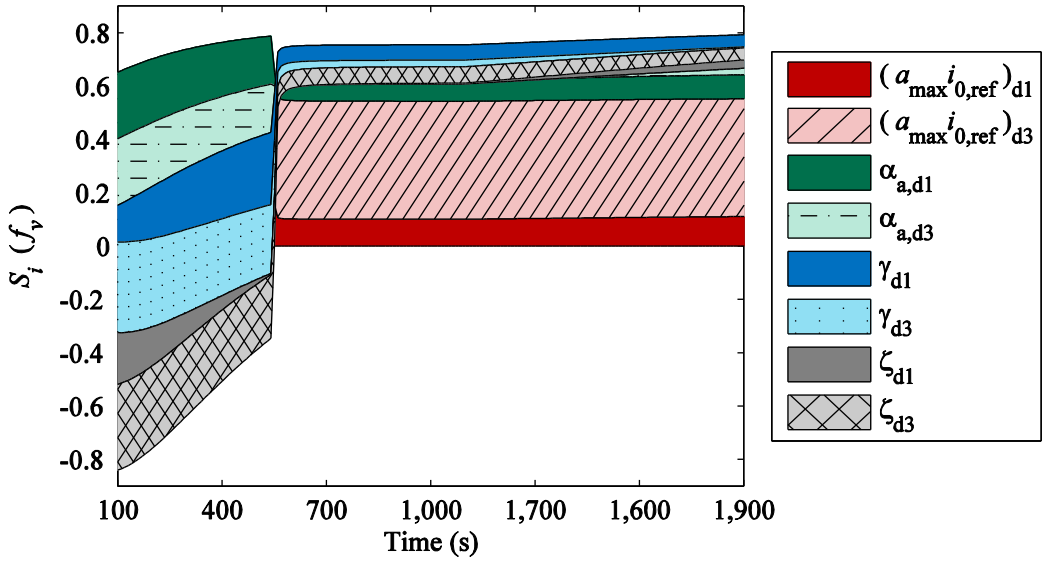

Figure 5-14: Area plot of the first-order sensitivity of the simulated voltage as discharge starts

Notice in from Figure 5-14 how the parameters defining the effective exchange current density take over from the other parameters as discharge starts. When discharge ends as shown in Figure 5-15, the morphology parameter for the negative electrode overshadows the effects of other parameters, but only for a short period.

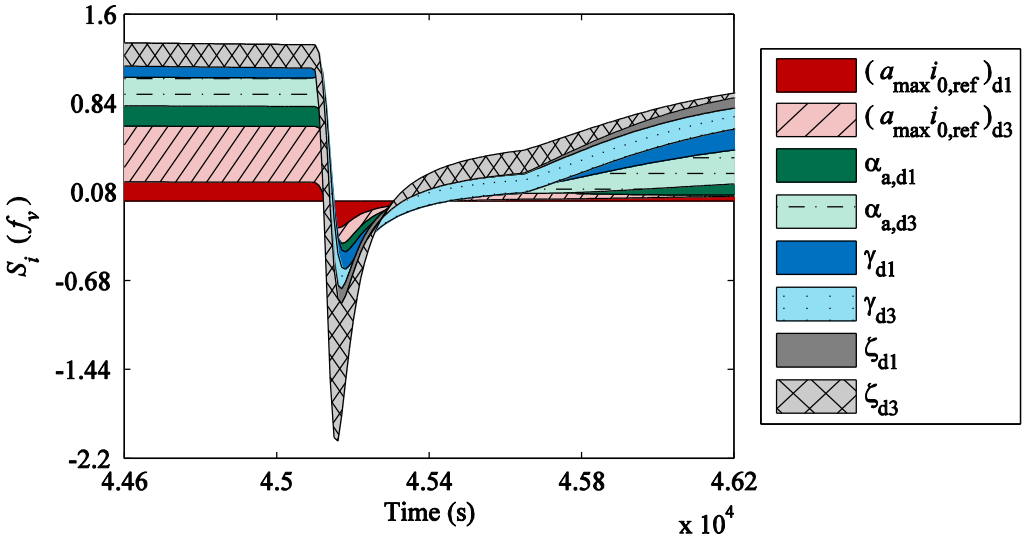

Figure 5-15: Area plot of the first-order sensitivity around the end of discharge

Figure 5-16 shows the first-order sensitivity of the simulated cell voltage when the cell transitions from float charging to rest. Once again, the morphology parameter for the negative electrode has a significant impact at this moment in time.

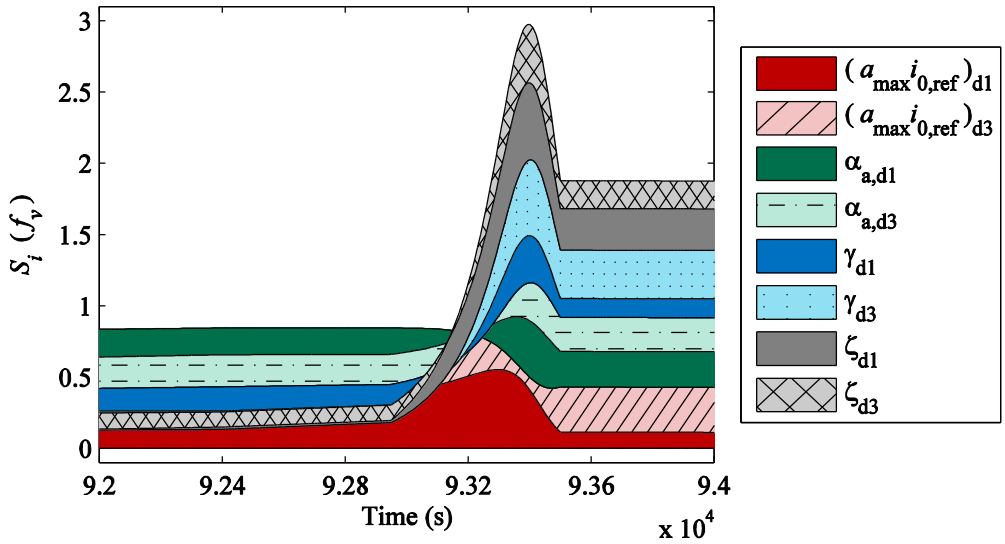

Figure 5-16: Area plot of the first-order sensitivity of simulated cell voltage around the transition from float charging to rest

The next calculation is the total sensitvity coefficients of the parameter effects on the simulated cell voltage, $S_{Ti}(f_v)$, using (5.20). The result is presented in Figure 5-17 over time and shows how important the effective exchange current densities of both electrodes are during constant-voltage charging.

The effective exchange current densities of both electrodes influence the cell voltage less and less as discharge continues because the active surface areas decrease. Their effects do remain somewhat constant when the cell is at rest because the active surface area does not change significantly during short periods at open-circuit. As the cell charges, the effective exchange current densities of both electrodes become more important again.

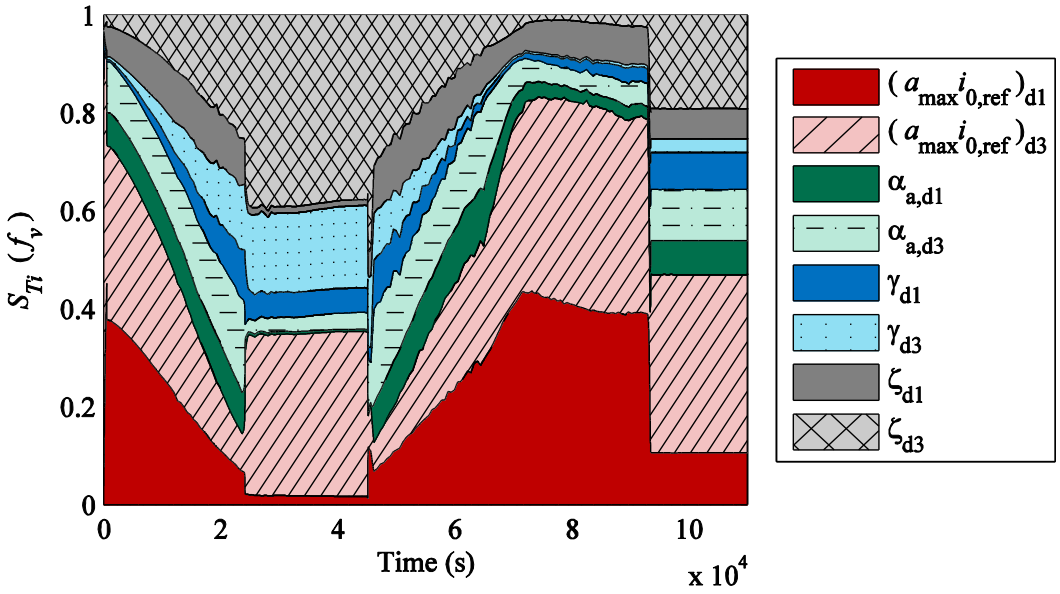

Figure 5-17: Area plot of the total sensitivity of simulated cell voltage over time

Another obeservation of note consists of the reaction order parameters – their total effects in the rest period between discharge and charge are much more significant than their first-order effects in Figure 5-13. The reaction orders are also much more influential as the electrolyte concentration decreases during discharge and vice-versa during charge.

The model error's total sensitivity over time $S_{Ti}(f_{sse})$ is calculated for each parameter using (5.20) and plotted with that of the simulated cell voltage $S_{Ti}(f_v)$ in Figure 5-18. The time periods where a parameter's total effect on the simulated voltage is highest correspond to the periods where the model error is most sensitive to that parameter.

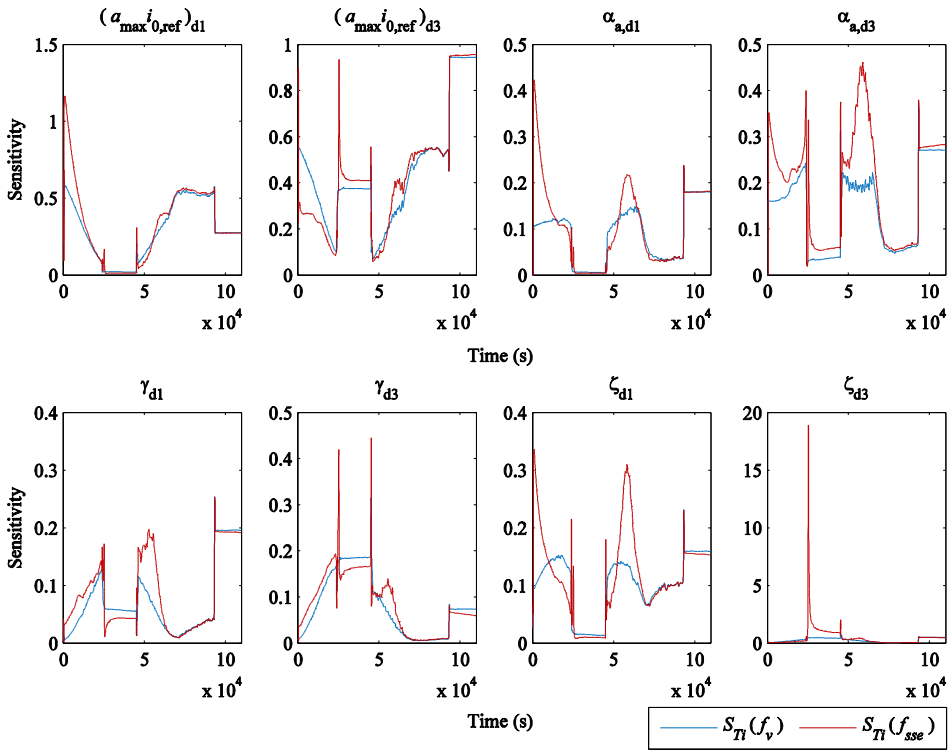

Figure 5-18: Total sensitivities of the simulated cell voltage and the model error over time

The final result of this chapter is presented in Figure 5-19. The total sensitivities of the simulated cell voltage and the model error to each parameter are compared using a bar chart.

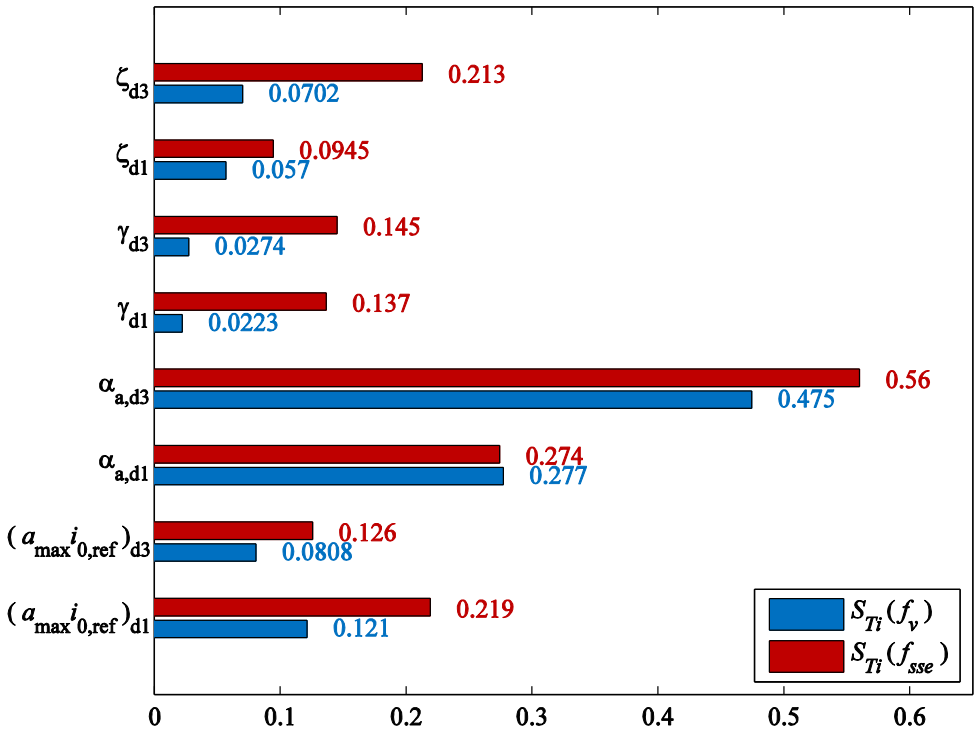

Figure 5-19: Bar chart of the total sensitivities of the simulated cell voltage and the model error

The total effects of the anodic transfer coefficients in Figure 5-19 are much larger than the rest of the parameter effects. This is due to the fact that a total sensitivity coefficient takes into account both first- and higher order parameter effects such as nonlinear combinations with other parameters [87].

5.5 Conclusions

A parameteric analysis was performed on the complete parameter input space of the multi-scale electrochemical model of a lead-acid cell. The majority of the input parameters were fixed using measured, calculated or theoretical values from open literature.

Before any analyses were performed, the multi-scale model's response during a discharge/charge cycle was verified using the available parameter values. The most uncertain parameters were then identified and ranked in elementary effects analysis (EEA) using the Morris method and the most important parameters were subjected to further analysis.

A quasi Monte Carlo approach to sufficiently explore the input space of the most uncertain model parameters, was presented. The results of the Monte Carlo experiment were used in variance-based sensitivity analysis (VBSA) with Jansen's formulae to obtain first-order and total sensitivity coefficients for each parameter. The sensitivities of both the simulated cell voltage and the sum of the model error squared to the most uncertain parameters were investigated.

The overall effect results from EEA and the total sensitivity results from VBSA suggest that the anodic transfer coefficients have the most significant effect on the simulated cell voltage. Even though substantially different samples of the input parameters were used in EEA than in VBSA, a parameter's overall effect in EEA is parallel to its total sensitivity coefficient from VBSA.

For each of the hundreds of model evaluations that were performed during this parameteric analysis, the sum of the model error with experimental data (squared) was calculated. The parameter values used in the model evaluation that resulted in the lowest model error will be used as the initial guess for parameter estimation in the following chapter.

6 MODEL VALIDATION AND INVESTIGATION OF IRREVERSIBLE SULPHATION

This chapter starts by explaining how the multi-scale model from Chapter 3 was validated using the results from parameteric analysis in Chapter 5 and experimental data. With an acceptably validated model, the active surface area of the positive electrode are simulated in partial state-of-charge (PSOC) conditions to investigate irreversible sulphation. The actual cell's internal resistance during the initial voltage drop (*coup de fouet*) from one discharge to the next is used as an indicator of sulphation.

6.1 Validation of the multi-scale model

6.1.1 Experimental data

The experimental data from various discharges using cell #3 are presented as the cell voltage versus Ah discharged in Figure 6-1. Various cut-off voltages were used to ensure that deep discharge behaviour would be exhibited.

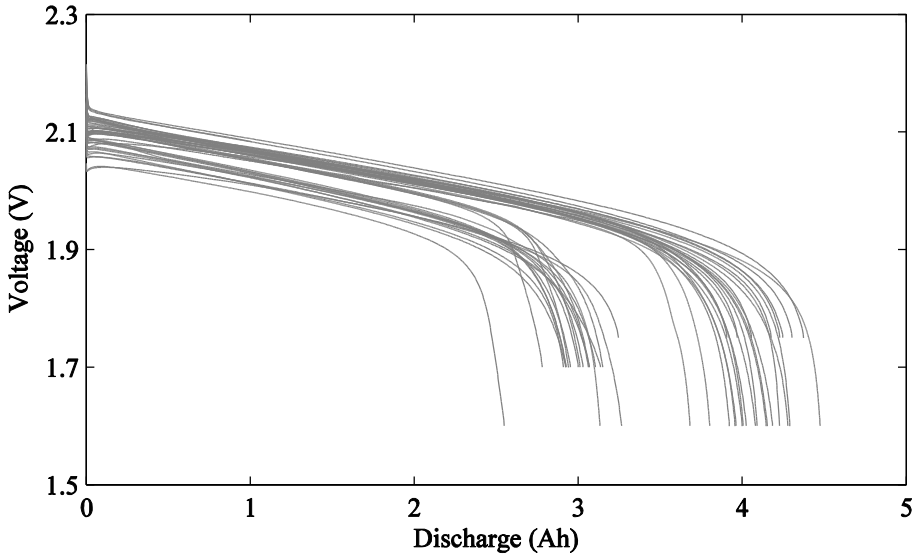

Figure 6-1: Discharge data from a single-cell VRLA battery with an AGM separator

Figure 6-2 presents the charge data, also from cell #3, using various rates. Similar sets of data from the other cells used for experimental data collection can be found in Appendix A.

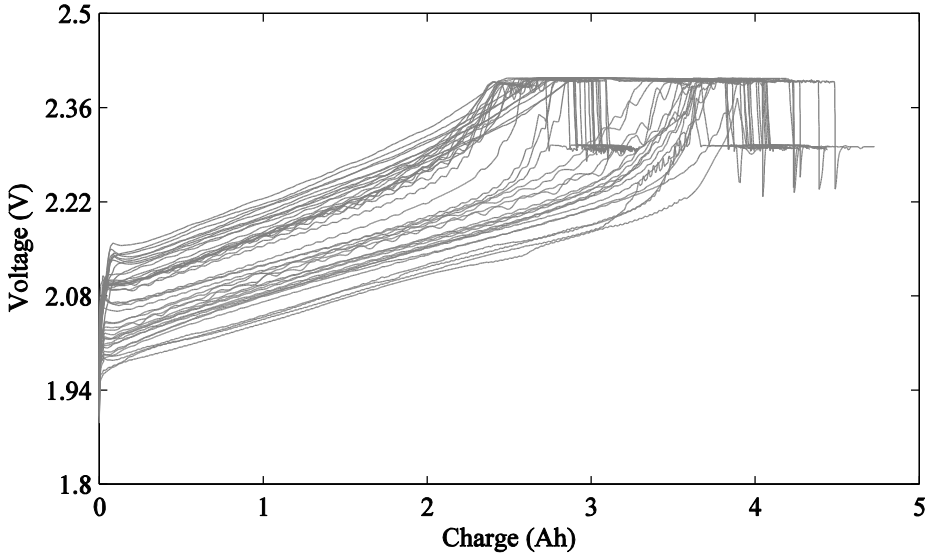

Figure 6-2: Charge data from a single-cell VRLA battery with an AGM separator

Multiple charge-discharge cycles are shown in Figure 6-3. OCV measurements that were used for EMF characterization as presented in Chapter 4 are also indicated by $E^*(t)$.

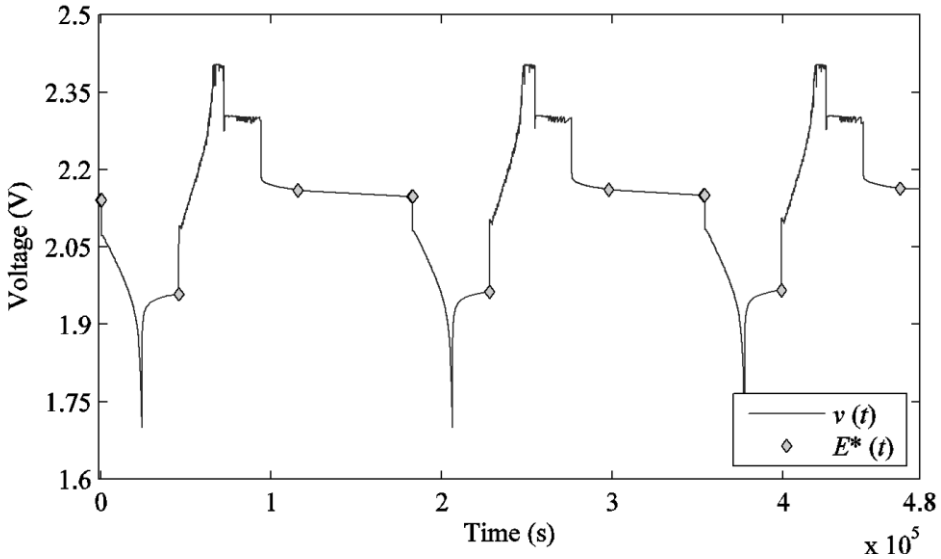

Figure 6-3: Multiple cycles of cell #3 with OCV measurements indicated

As mentioned previously, temperature variations are taken into account in the multi-scale model and temperature measurements can be seen in Figure 6-4. Temperature samples at the same time instants as the OCV measurements in Figure 6-3 are indicated in Figure 6-4.

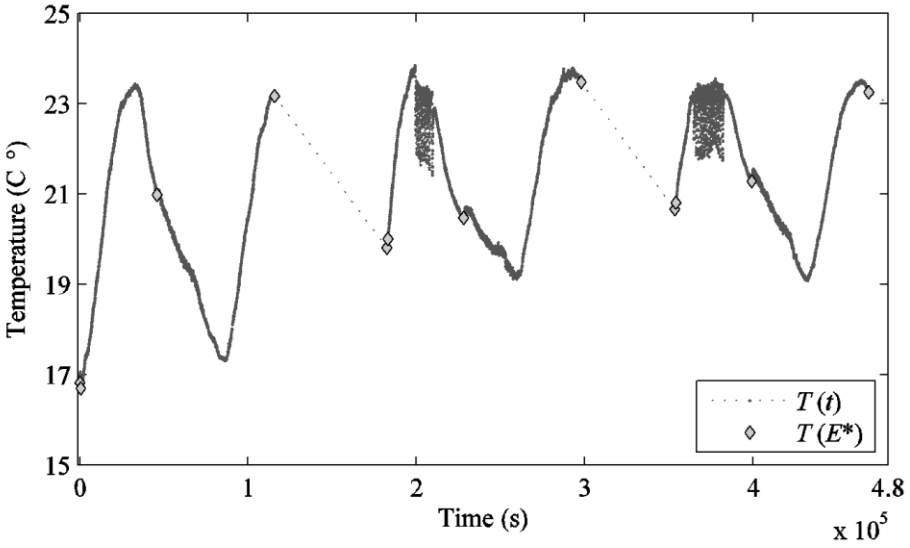

Figure 6-4: Various temperature conditions for cell #3 with OCV measurements

For full details of the steps in experimental data collection, refer to Section 4.3.1 and Section 5.2.3. Experimental data in the form of voltage, current and temperature measurements for all of the 8 VRLA cells used in this study, can be found in the digital supplement as stated in Appendix B.

6.1.2 Parameter estimation

The steps for parameter estimation are now explained and applied to the multi-scale model. Model parameter estimation typically consists of iteratively adjusting input parameters until the objective function reaches an acceptable optimum [109]. The objective function contains information used by an optimization algorithm that determines where to continue the search within the input space [110].

The objective function for parameter estimation of the multi-scale model consists of the squared sum of the difference between the predicted cell voltage (v) and the measured cell voltage (v^*). This error is called the model prediction error (sse) and is given by:

$$sse = \sum_{g=1}^{t} \left[v^*(g) - v(g) \right]^2 \tag{6.1}$$

In this study, the model prediction error is iteratively minimized until the predicted voltage displays acceptable agreement with the experimental data. With regard to the choice of an optimization algorithm, a few issues require consideration. A major challenge with the objective function in (6.1) entails the characteristics of the objective function over the range of parameters to be optimized. Without detailed knowledge of the objective function's behaviour, the choice of an optimization algorithm becomes limited [111].

If the characteristics of the objective function are unknown such that a local optimum might be mistaken for a global optimum, a global optimization algorithm is more appropriate than a local method [110].

Gradient-based optimization algorithms require the objective function to be differentiable with respect to the input parameters [112]. It cannot be assumed at this point that the objective function in (6.1) is differentiable. Results from variance-based sensitivity analysis of the model prediction error to input paramters indicate that the objective function is non-smooth. As such, a derivative-free optimization algorithm has to be used for parameter estimation of the multi-scale model's input parameters.

Parameter estimation in this chapter is further constrained by upper and lower bounds for the input parameters [112]. A global optimization algorithm that allows for parameter constraints within COMSOL Multiphysics® is the Monte Carlo solver in the Optimization Module. This solver does not get stuck in local minima, as other optimization solvers in COMSOL Multiphysics® do, but can take a long time to converge because the entire input space is explored.

Consider the objective function's landscape over the variation of the anodic transfer coefficients within their upper and lower bounds in Figure 6-5.

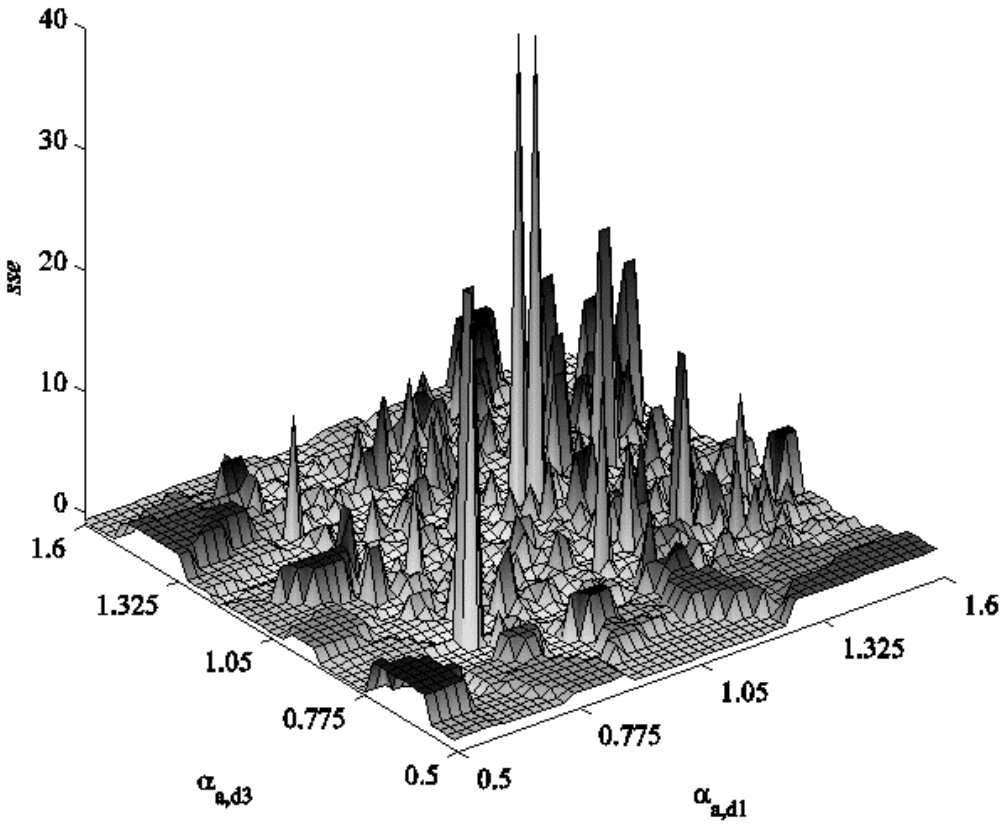

Figure 6-5: Objective function landscape for the anodic transfer coefficients

The error surface in Figure 6-5 consists of over 5,000 model evaluations during Monte Carlo optimization. Details of the numerical solution and model verification can be found in Section 5.2. The objective function landscape for the other parameters of the multi-scale model can be found in the digital supplement of this study as stated in Appendix B.

Note that the error surface in Figure 6-5 is not due to the effects of the anodic transfer coefficients alone because the multi-scale model is characterized by complex parameter interaction effects. Refer to Section 5.4 for more detail regarding the first-order and total effects of the most influential parameters in the multi-scale model.

Figure 6-5 is an illustration of how considerably non-smooth the objective function is. Derivative - based alogrithms would not have sufficed. Local derivative-free algorithms would have converged prematurely in one of the many local minima. Of course, the Monte Carlo solver utilized in this study for paramater estimation required an excessive amount of time to converge to an *sse* of 1.1779. The resulting set of optimized parameter values are shown in Table 6-1. The rest of the model input parameters were determined in Chapter 5 during an in-depth parametric analysis.

Table 6-1: Optimized parameters from a Monte Carlo optimization to be used in the multi-scale model for simulation of a lead-acid cell

Parameter	*Unit*	d_1	d_3
a_{max}	cm^2/cm^3	$1e^5$	$2.3e^4$
α_a	-	1.15	1.3
γ	-	0.3	$1e^{-4}$
$i_{0,ref}$	A/cm^2	$1e^{-7}$	$2e^{-6}$
ζ	-	0.1	1.0

6.1.3 Validation results

The multi-scale model with optimized parameters in Table 6-1 is used to simulate a complete cycle and the result is presented in Figure 6-6. The measured cell voltage is also shown. The model prediction error corresponds to an *sse* of 1.1779, an *mse* of 0.0012 and a percentage error of 1.1 %.

An in-depth parametric analysis was performed in chapter 5 but the focus was on parameters that were not easily obtainable from the relevant literature. Some of the electrode and electrolyte material properties taken from literature might be different for the single-cell VRLA battery under investigation. This could explain the deviation between the simulated and measured cell voltages in Figure 6-6.

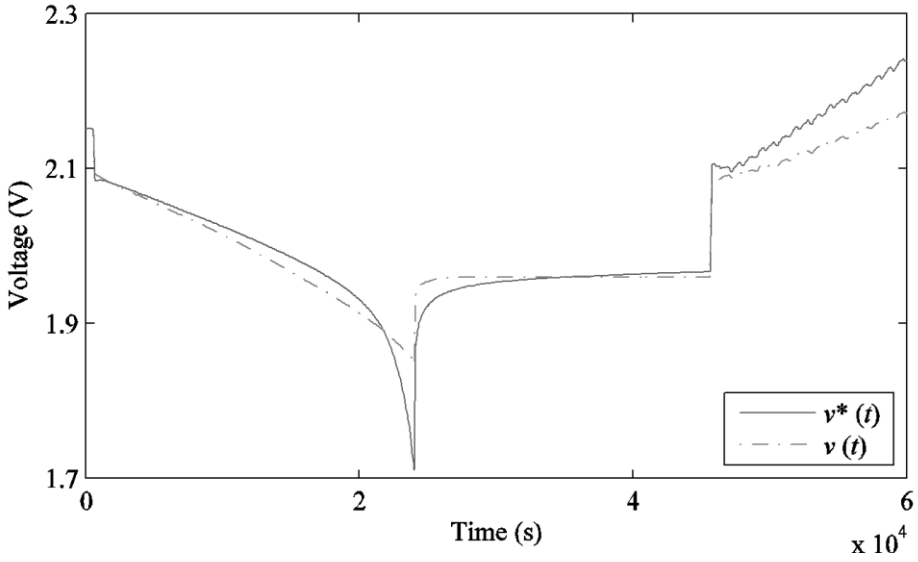

Figure 6-6: Model output compared to experimental data

Furthermore, the multi-scale model does not account for energy lost to side reactions and future work would have to include this. The exact amount of charge actually accepted by the battery, as well as the process of charge acceptance, is an active research area [113]–[116].

The results might also be improved by using a higher number of experimental measurements under various conditions. Parameter estimation could be repeated by allowing the optimization solver more time to explore the input space. The objective function in (6.1) might have to be expanded to include other model outputs but more objectives would require further experimental measurements.

The optimization solver is constrained by upper and lower bounds for each input parameter which means that the solver does not have complete freedom to explore the entire input space. Selecting a solver without these constraints might improve the agreement between the simulated and measured cell voltages.

With an optimal set of input parameters and an acceptably validated model, irreversible sulphation can now be investigated.

6.2 Investigation of irreversible sulphation

The aim of this section is to recreate the conditions in which a lead-acid cell would sustain damage from irreversible sulphation. Cell #3 experienced a few deep-discharges over its lifetime but it was always fully charged afterward by the UBA5 according to the manufacturer's specifications. Consider Figure 6-7 showing discharge-charge cycles #12 and #68 for cell #3 with a rate of 0.05C applied during both. The SOC was calculated by the charge controller using traditional Coulomb-counting.

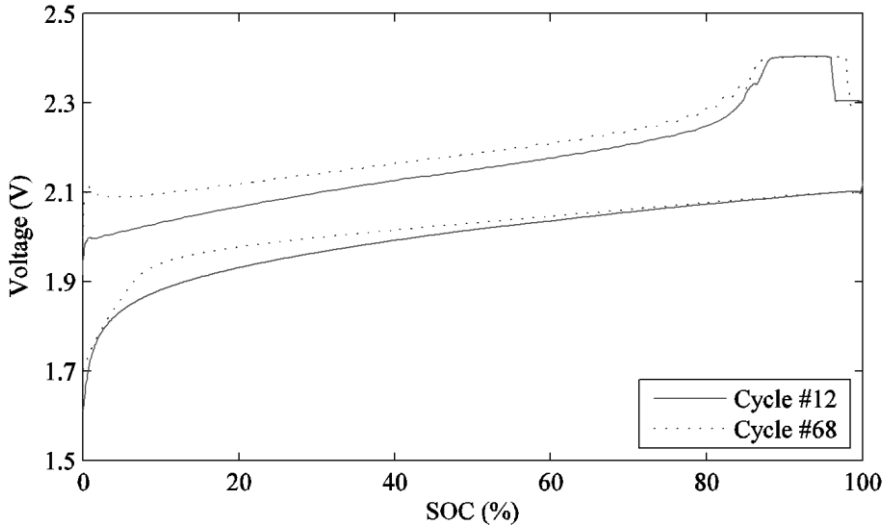

Figure 6-7: Cell voltage versus SOC for two cycles at the same rate of 0.05C

It should be clear that, according to the charge controller, the cell was fully recharged after both discharges in Figure 6-7. Only these two cycles are shown here for simplicity but the rest can be found in the digital supplement of this thesis. The cycles were selected to represent a relatively fresh cell and a somewhat older cell with irreversible sulphation. Now consider Figure 6-8 displaying the cell's voltage over time during each of these two cycles. The *coup de fouet* at the start of both discharges and charges are encircled. This phenomenon is a source of uncertainty in the LAB community and many possible explanations exist [117].

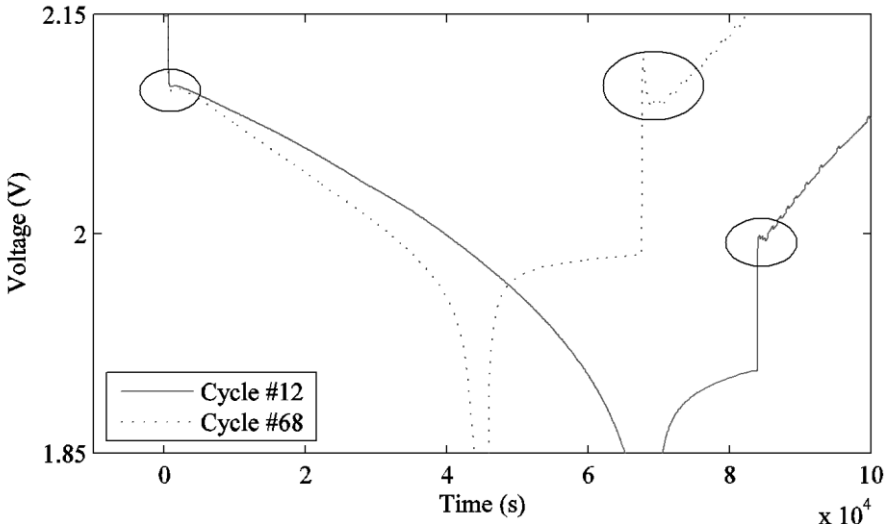

Figure 6-8: *Coup de fouet* early in a cell's lifetime in comparison with many cycles later

It is widely accepted theory that the *coup de fouet* at the beginning of discharge is due to a crystallization overpotential and corresponds to an energy gap that the cell has to overcome [98].

Figure 6-8 clearly shows that the energy gap has increased over the lifetime of the cell under consideration. As such, it is considered here to be an indication of irreversible sulphation and lowered electrolyte conductivity.

6.2.1 Simulation of partial state-of-charge (PSOC) conditions

PSOC conditions are recreated in simulation by decreasing the maximum active surface area of an electrode from its fully charged value [63]. This decrease represents the lack of a full charge during previous cycles. Gas evolution occurs earlier during high-rate charging and all of the lead-sulphate cannot be converted back into usable Pb and PbO_2. This PSOC condition could be due to operating requirements or an error in SOC indication.

In the simulations that follow all of the other model parameters remain exactly the same. Only the positive electrode's maximum active surface area is changed to 60% of the value for a fully charged cell. The positive electrode's porosity at this decreased active surface area is determined by a short discharge using COMSOL Multiphysics®. Simulations using the active surface area of a fully charged cell will represent a healthy or new lead-acid cell whereas the simulation with the decreased active surface area will be represent a cell damaged by irreversible sulphation.

Figure 6-9 shows the cell voltages of these two cells during a partial discharge at a rate of 0.1C. The simulation result in Figure 6-9 displays an initial voltage drop larger in magnitude for the damaged cell. As mentioned before, this is considered to be due to the increase in internal resistance from irreversible sulphation.

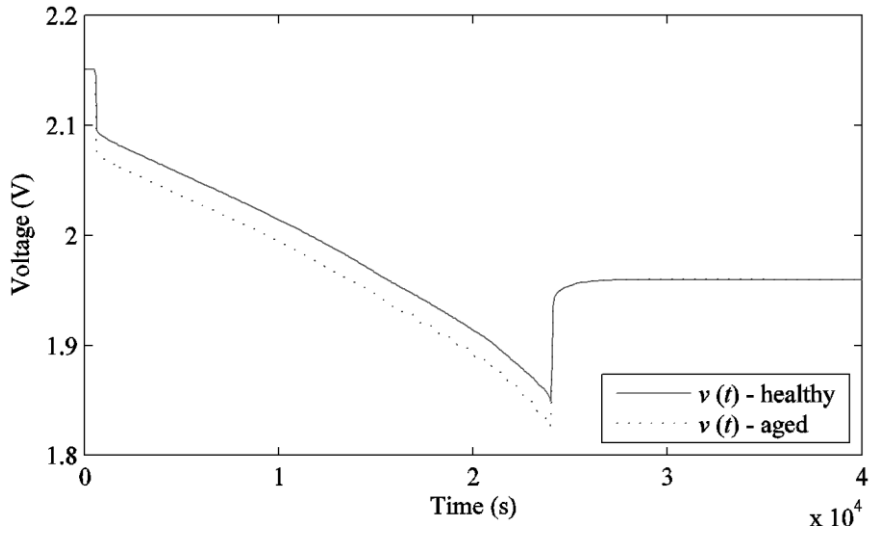

Figure 6-9: Simulated cell voltage of a healthy and a damaged lead-acid cell during a partial discharge and subsequent rest period

When comparing Figure 6-8 with Figure 6-9, it should be evident that the two simulated cycles show discharges of equal discharge time. The experimental data in Figure 6-8 show that the discharges continued until a specified COV with different discharge times. It would have been better to use experimental data from two discharges, both at the same rate, but using the same time until the end of discharge.

Consider now Figure 6-10 showing the positive electrode's active surface area as it decreases during the same partial discharge at a 0.1C rate. The damaged cell clearly starts with a lower active surface area than the healthy cell. The difference in magnitude of the initial voltage drops in Figure 6-9 is clearly due to the decrease in active surface area. It is thus concluded that minor errors in SOC indication can result in accidental PSOC operation and over time, irreversible sulphation.

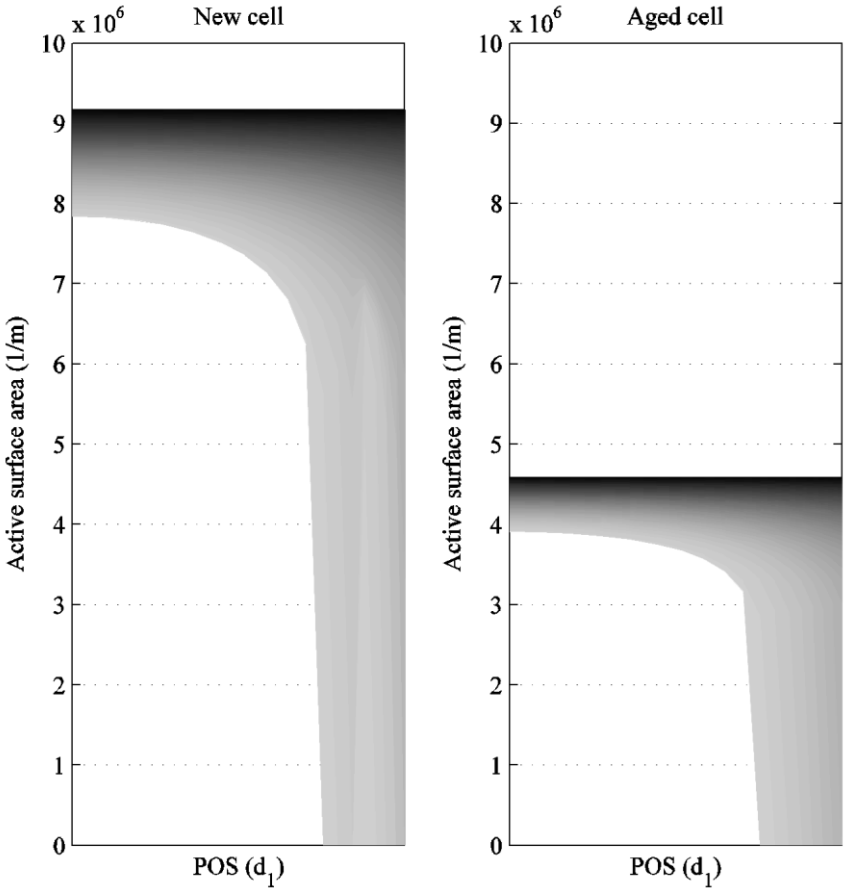

Figure 6-10: Simulated active surface area of the positive electrode region during discharge

Even though both porous electrodes undergo sulphation during discharge, irreversible sulphation is more commonly observed at the negative electrode. Since the aim here is to simulate PSOC conditions and observe changes in the surface of an electrode, the results of the positive electrode was arbitrarily selected. The simulation results of the negative electrode are very similar and do not add new information to the investigation.

6.3 Conclusions

Parameter estimation for the multi-scale model was presented and the choice for a derivative-free optimization algorithm motivated. The results from Chapter 5 proved helpful in defining the bounds of the input space and selecting a suitable initial guess for the optimization algorithm. Convergence of the Monte Carlo solver in COMSOL Multiphysics® required a significant amount of time because the objective function's landscape is littered with multiple local minima.

The multi-scale model was acceptably validated (1.1% error) using experimental data during discharge, charge and rest. A few suggestions to improve the agreement between the simulated and measured voltages were proposed. The model was then used to simulate PSOC conditions and investigate irreversible sulphation. The voltage measurements of an actual cell with and without irreversible sulphation were also presented. With the help of the multi-scale model, the positive electrode's active surface area was simulated to correspond to a healthy and a damaged cell.

The simulation results indicate that the active surface area suffers permanent decreases during PSOC operation. The active surface area is reduced due to sulphate crystal coverage [76]. Sulphation is easily remedied by regularly charging the cell until full, but with PSOC operation, all of the crystals do not dissolve and can harden over time. The hardening of these crystals are due to recrystallization.

Consecutive increases in the internal resistance of the cell were taken as an indication of hardened sulphate crystals that lower the conductivity of an electrode [118]. Furthermore, the electrolyte concentration is never able to recover to that of a full cell because some of its ions are trapped in the lead-sulphate crystals [20].

Irreversible sulphation after prolonged periods at a low SOC is due to the cell's natural tendency to self-discharge but this operating mode was not investigated. The sulphate crystals have ample time to recrystallize and harden during these prolonged periods. Subsequent charging cannot sufficiently dissolve all the crystals and the cell suffers a permanent decrease in capacity.

Even though the SOC is an indication of the cell's remaining capacity, it is concluded here that the SOC cannot be used to avoid battery damage from irreversible sulphation if it is inaccurate.

7 CONCLUSIONS

The final chapter completes this thesis with a summary of the work and relevant findings. The research contributions are substantiated and recommendations for future work are provided.

7.1 Summary

Irreversible sulphation remains a major contributor to premature capacity loss in VRLA batteries [20]. Two operating modes, prolonged periods at a low SOC and PSOC operation, are known to accelerate this damage mechanism. The usefulness of SOC indication in preventing irreversible sulphation was under investigation in this study.

A multi-scale electrochemical model of a VRLA cell with an immobile electrolyte was developed in Chapter 3 using the macro-homogeneous approach. Active surface area and porosity components were included to ensure coupling between the microscopic and macroscopic scales [79].

Convection in the separator's electrolyte is a model feature that has been included in the multi-scale model but not found in previous modelling efforts for VRLA designs with an immobile electrolyte (see Table 1-1). Additionally, the multi-scale model does not consider the cell to be isothermal and accounts for temperature effects on the cell voltage (see Sections 0 and 4.3.3).

The multi-scale model required verification and validation if it was to be used for any sort of investigation of irreversible sulphation. The model's response was successfully verified in Section 5.2.2 for discharge, rest and charge.

EMF characterization was chosen to obtain a curve representing the cell's actual behaviour. The existing characterization methods lacked in accuracy (Table 4-1) and applicability. The results indicated that linear interpolation and linear extrapolation inherit the errors associated with SOC calculation as explained in Section 2.2.1. An alternative concentration-based method was developed and a verified curve of the cell's experimental EMF against estimated molality was obtained (Figure 4-11). The concentration-based method proved superior to the existing methods most probably because it made use of known information regarding the shape of an EMF curve for a lead-acid cell.

An added advantage of the concentration-based method for EMF characterization is that it does not require a temperature-controlled environment during experimental work.

The representative EMF curve from the concentration-based method, in Figure 5-1, was used for model calibration during parameteric analysis of the multi-scale model in Chapter 5. Parameter estimation for a detailed electrochemical model is an ill-defined process and extremely challenging [63]. The several input parameters of the multi-scale model were subjected to a detailed parameteric analysis with the hope of obtaining insight for successful parameter estimation.

The analysis in Chapter 5 started by fixing the least uncertain parameters. The remaining set was subjected to elementary effects analysis with the Morris method to obtain a final set of only the most influential parameters. Using Figure 5-9, it was determined that the parameters for electrode kinetics in the Butler-Volmer equation are the most influential. These parameters were used for variance-based model sensitivity analysis in a Monte Carlo simulation with Jansen's formulae for the calculation of sensitivity coefficients.

Quantitative results from the variance-based sensitivity analysis confirmed that the parameters for electrode kinetics have the most significant effect on the simulated cell voltage (Figure 5-19). The results further revealed exceptionally complex interaction between input parameters in the multi-scale model. Detailed electrochemical modelling requires an in-depth understanding of the problem because this modelling approach is particularly difficult [119].

With some confidence in the initial guess for the values of the most influential parameters after parameteric analysis, parameter estimation proceeded. The relationship between the model prediction error and the input parameters is littered with local minima (see Section 6.1.2). The optimized parameter values were used in experimental model validation in Section 6.1.3. The model was acceptably validated (1.1% error) using experimental data from a lead-acid cell during discharge, rest and charge. The systematic approach toward resolving the uncertainty of value selection for the multi-scale model's input parameters presented in this thesis, proved helpful.

After experimental validation of the multi-scale model, it was used to simulate PSOC conditions. PSOC operation was modelled by a decrease in the maximum active surface area of the positive electrode. A decrease in this maximum area corresponds to a lack of full charge during previous cycles. The active surface area of the positive electrode was observed during these simulations, (Figure 6-10). It was concluded, after comparison with experimental data from a cell with and without irreversible sulphation, that the decrease in the active surface area causes an increase in internal resistance [120].

PSOC operation can occur unintentionally with slight errors in SOC indication and result in irreversible sulphation over time. It was thus concluded that irreversible sulphation cannot be prevented satisfactorily using SOC information because SOC is not indicative of this specific damage mechanism.

7.2 Contributions

The main contribution of this study is a multi-scale electrochemical model of a VRLA battery with an immobile electrolyte and its analysis. The relevant literature is brimming with VRLA modelling efforts but few are validated with experimental data [46]. Even less are validated for more than a single rate and for both discharge and charge [27]. The multi-scale model developed in this study was able to successfully simulate galvanostatic discharging, rest, as well as both galvanostatic and potentiostatic charging (Figure 5-12). To the best of the author's knowledge, it is the most comprehensive model of a VRLA battery with an immobile electrolyte.

The parameteric analysis of the multi-scale model produced quantitative sensitivity results regarding the complex effects of the parameters that define electrode kinetics (see section 5.4). This type of in-depth parametric analysis has not been seen before.

This model can be used to simulate more than just the operating modes that lead to irreversible sulphation. For example, the impact of long term operation on the surface areas and porosities of the electrodes can be studied. As stated before, the model's value as a research contribution is not based in its many equations but rather in its utility as an investigative tool.

Regarding battery damage from irreversible sulphation, the following was discovered:

- Slight errors in SOC indication can result in unintentional PSOC operation over time.
- SOC information is not sufficiently indicative of battery damage from irreversible sulphation. As such, SOC indication is not capable of preventing irreversible sulphation.
- For charge controllers to be able to prevent irreversible sulphation and the associated premature capacity loss, they will require reliable information regarding the cell's internal condition.
- A curve of the cell's EMF versus electrolyte concentration is much more descriptive of its internal state than a curve of the EMF versus SOC.

The time and complexity associated with parameter estimation for the multi-scale model were reduced somewhat by the results from an accurate EMF characterization method. This method, based on estimations of the electrolyte concentration, proved to be more accurate than the existing methods for EMF characterization. As such, it is regarded as a secondary contribution of this study.

7.3 Recommendations for future work

Future modelling efforts should include a thorough experimental validation of the multi-scale model using various rates. The authors in [63] mention how difficult parameter optimization for this type of model is and that they optimize the parameters in some other way. Unfortunately, they do not describe the exact steps used to do so.

This study has shown that charge controllers using more than SOC information are necessary for the prevention of irreversible sulphation. Future work could include the development and application of a charge control algorithm using the concentration-based EMF curve because it requires very basic measurement data.

The concentration-based method for EMF characterization requires further investigation because its resulting EMF curve displayed noteworthy promise in online concentration indication. The first step would consist of experimental measurements of electrolyte concentration and comparison with the estimated molality.

Convection in the separator electrolyte of a VRLA cell with an immobile electrolyte was modelled but its effects have yet to be examined. It was included in the multi-scale model for completeness of mass transport effects but might have added to the complexity experienced during parameter estimation.

More detailed equations of lead-sulphate crystal growth can be included in future modelling efforts. This will enable an investigation of irreversible sulphation involving not only the electrode active surface area but various sizes of crystals as well [23].

A final recommendation is to include the evolution and recombination of gases in the multi-scale model because these processes are responsible for improving but also complicating lead-acid battery technology. This inclusion would enable the simulation of gassing during overcharge of a VRLA battery and the associated water loss [41], [43], [121].

7.4 Closing

The aim of this study was to better understand microscopic processes in the EDL and observed macroscopic phenomena. This aim was achieved by investigating irreversible sulphation with a validated multi-scale model of a VRLA cell with an AGM separator.

With a thorough understanding of premature failure due to irreversible sulphation in VRLA batteries, charge controllers can be improved. This will ensure that the end-user has no opportunity for incorrect or abusive operation of the battery. Research contributions to the mature field of lead-acid batteries are, in essence, advances in energy storage technology. As such, this study is part of a global effort towards a sustainable energy future.

A EXPERIMENTAL DATA

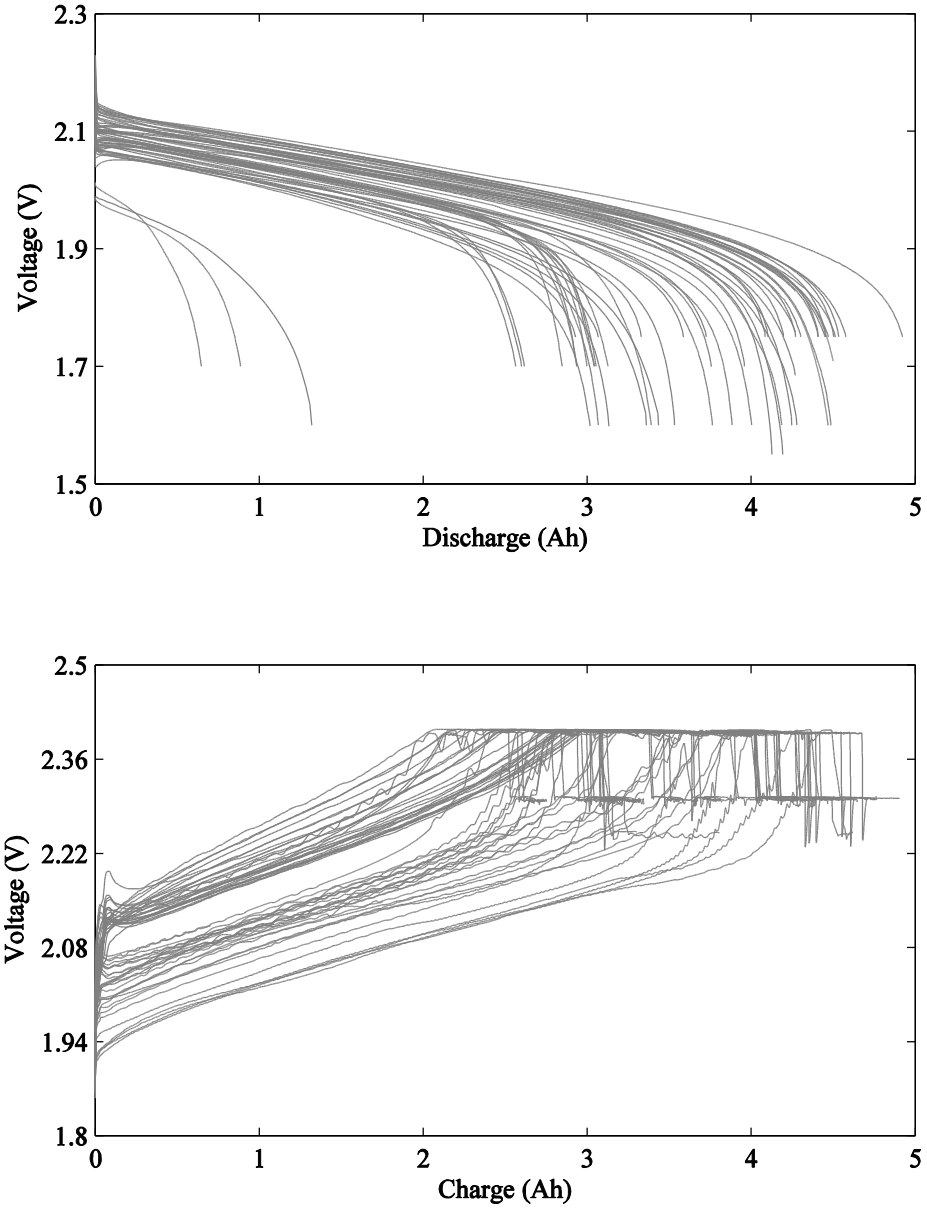

Figure A-1: Experimental cyling data of cell #1

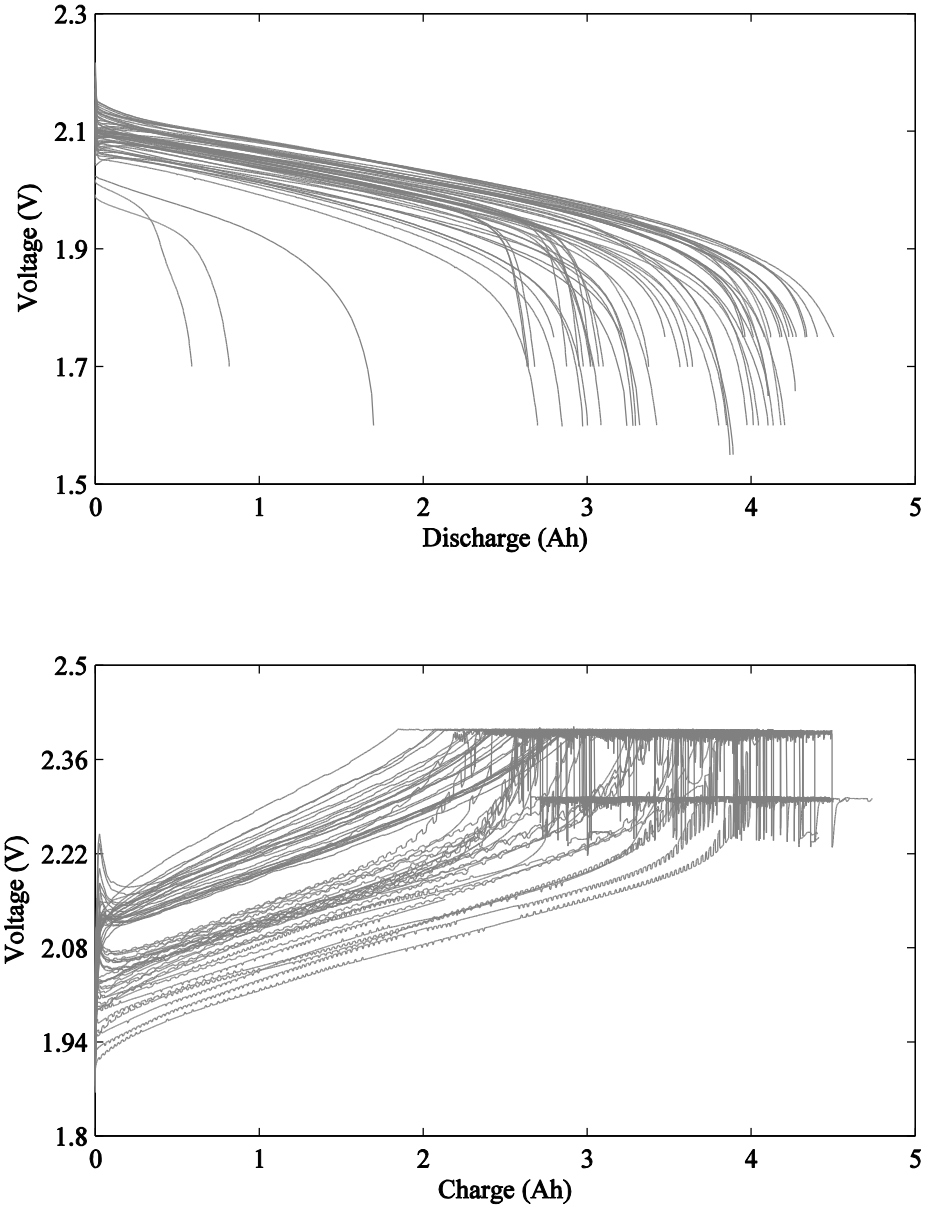

Figure A-2: Experimental cyling data of cell #2

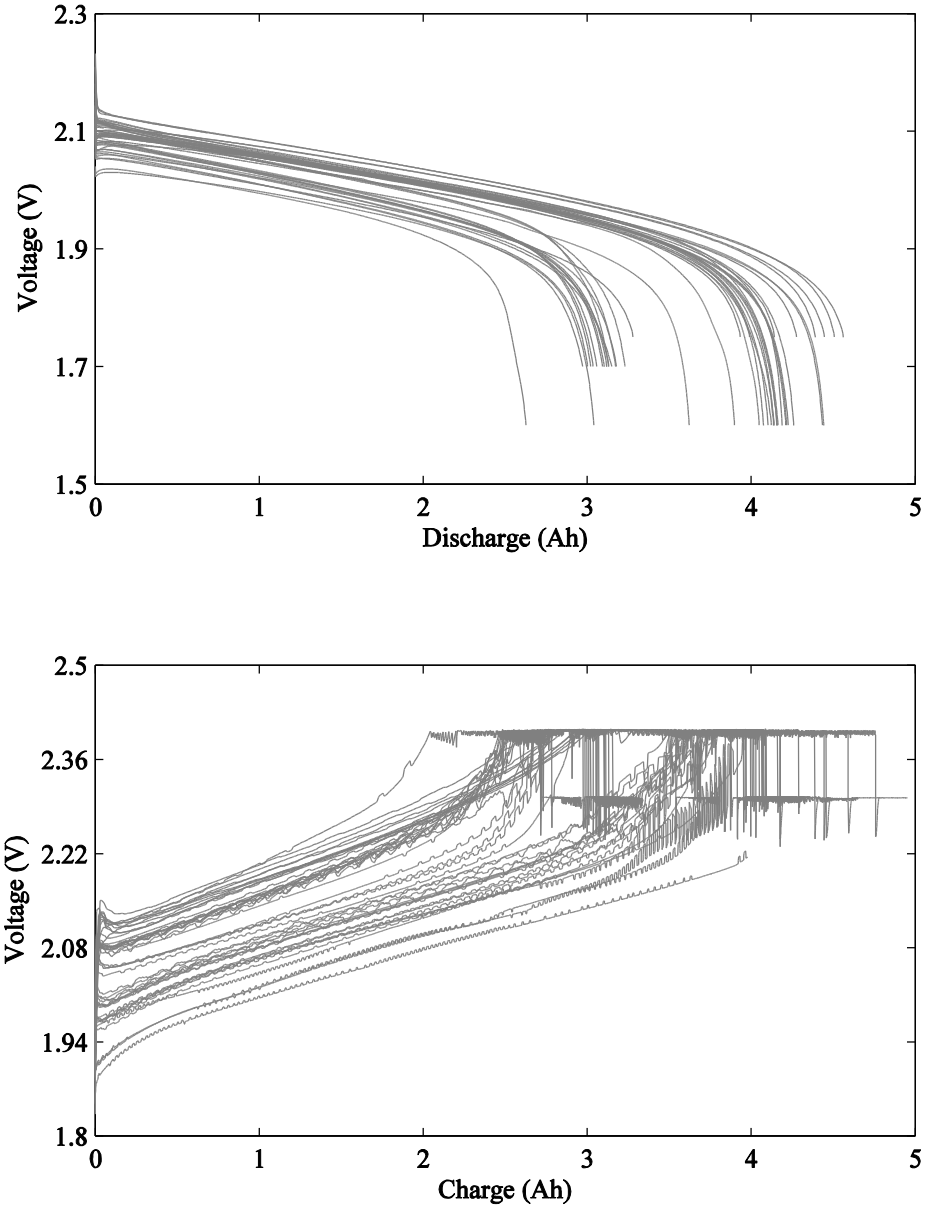

Figure A-3: Experimental cyling data of cell #4

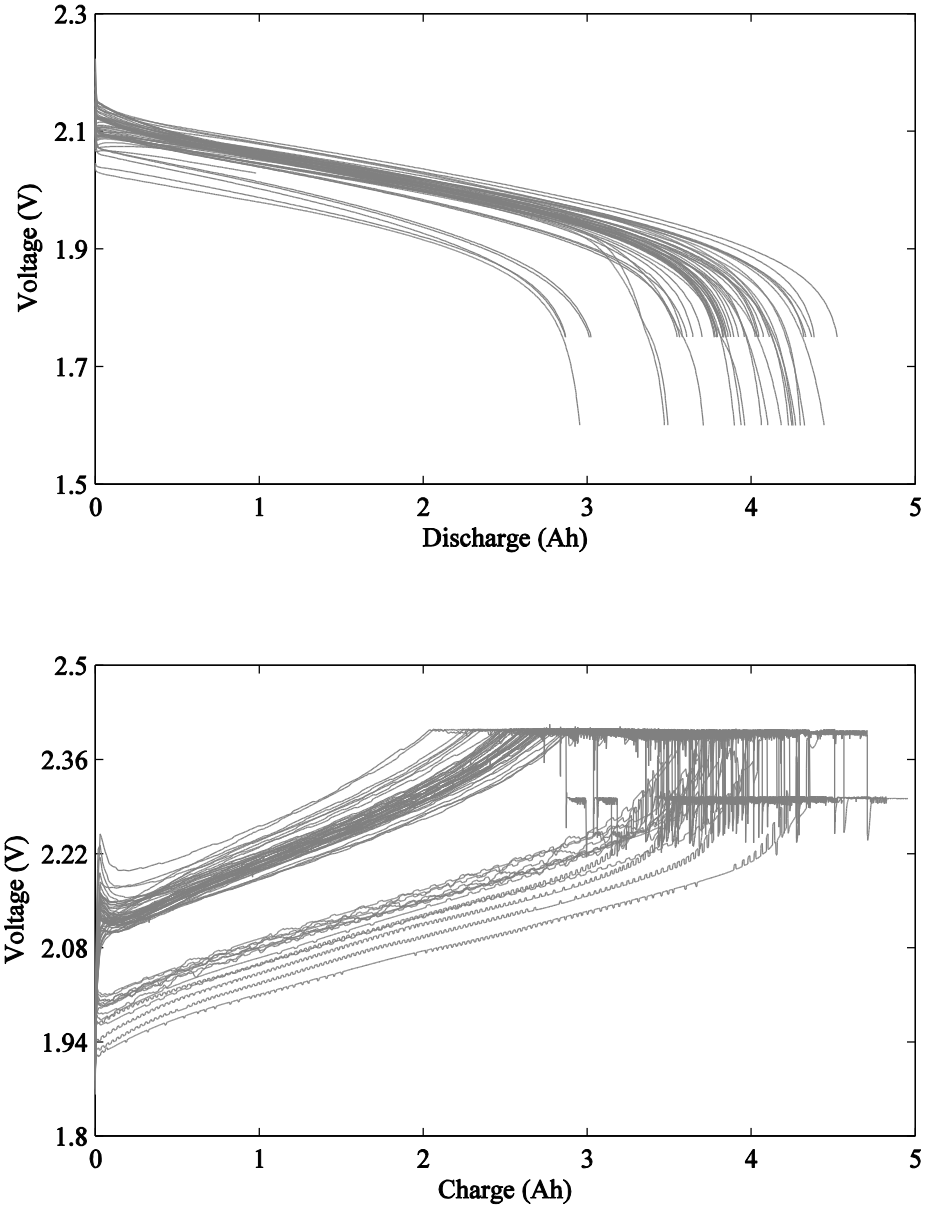

Figure A-4: Experimental cyling data of cell #7

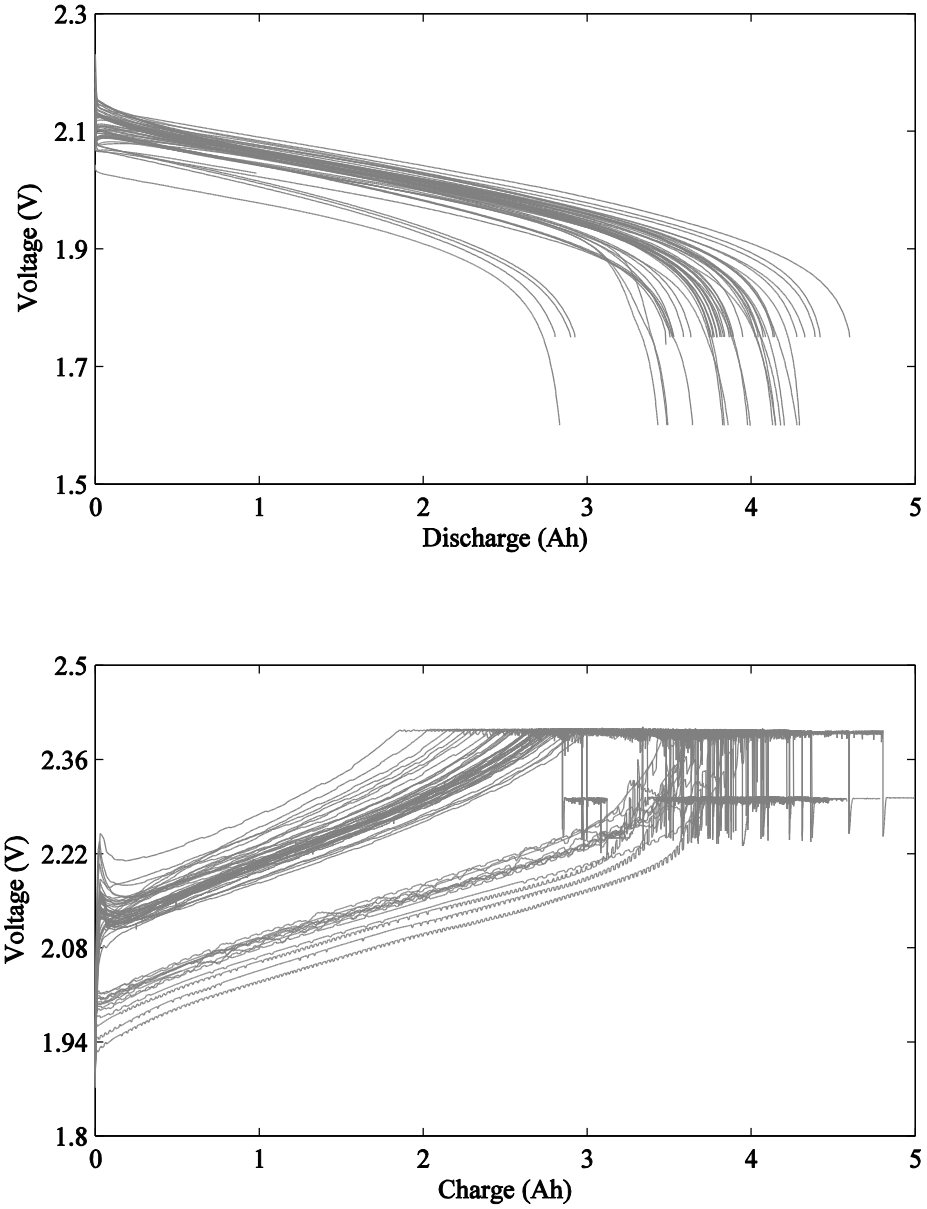

Figure A-5: Experimental cyling data of cell #8

B DIGITAL SUPPLEMENT

The digital supplement of this thesis contains folders with the following:

- Processed experimental data from all eight VRLA cells used for data collection.
- The multi-scale model as implemented in COMSOL Multiphysics®.
- The various m-files for EMF characterization and parameteric analysis in MATLAB®.
- A conference paper presented at the IFAC World Congress in 2014: A. Janse van Rensburg, G. van Schoor, and P. A. van Vuuren, "Active Surface Area Approximation in a Lead-Acid Cell for Optimal Performance in Renewable Energy Systems," in *IFAC World Congress*, 2014, vol. 19, no. 1, pp. 9450–9455.

REFERENCES

[1] J. B. Goodenough, H. Abruña, M. Buchanan, S. Visco, M. Whittingham, B. Dunn, Y. Gogotsi, A. Gewirth, D. Nocera, R. Kelley, and others, "Basic Research Needs for Electrical Energy Storage," *US Department of Energy Report*, 2007.

[2] J. Zhang, L. Zhang, H. Liu, A. Sun, and R. S. Liu, *Electrochemical Technologies for Energy Storage and Conversion*. Wiley-VCH, 2011.

[3] G. Coppez, S. Chowdhury, and S. Chowdhury, "The Importance of Energy Storage in Renewable Power Generation: A Review," in *45th International Universities Power Engineering Conference (UPEC)*, 2010, pp. 1–5.

[4] R. A. Kelly, *Global Issues: Energy Supply and Renewable Resources*. Infobase Publishing, 2007.

[5] P. T. Moseley and J. Garche, *Electrochemical Energy Storage for Renewable Sources and Grid Balancing*. Newnes, 2014.

[6] H. Ibrahim, A. Ilinca, and J. Perron, "Energy storage systems – Characteristics and comparisons," *Renewable and Sustainable Energy Reviews*, vol. 12, no. 5, pp. 1221–1250, 2008.

[7] N. K. C. Nair and N. Garimella, "Battery energy storage systems: Assessment for small-scale renewable energy integration," *Energy and Buildings*, vol. 42, no. 11, pp. 2124–2130, 2010.

[8] Z. Liu and H. Li, "Thermal modeling for vehicle battery system: A brief review," in *International Conference on System Science and Engineering (ICSSE)*, 2012, pp. 74–78.

[9] A. A. Pesaran, "Battery thermal models for hybrid vehicle simulations," *Journal of Power Sources*, vol. 110, no. 2, pp. 377–382, 2002.

[10] D. Pavlov, *Lead-Acid Batteries: Science and Technology*. Elsevier Science, 2011.

[11] R. Kaiser, "Optimized battery-management system to improve storage lifetime in renewable energy systems," *Journal of Power Sources*, vol. 168, no. 1, pp. 58–65, 2007.

[12] R. Dufo-López, J. M. Lujano-Rojas, and J. L. Bernal-Agustín, "Comparison of different lead–acid battery lifetime prediction models for use in simulation of stand-alone photovoltaic systems ," *Applied Energy* , vol. 115, pp. 242 – 253, 2014.

[13] K. Knehr, C. Eng, Y. K. Chen-Wiegart, J. Wang, and A. C. West, "In Situ Transmission X-Ray Microscopy of the Lead Sulfate Film Formation on Lead in Sulfuric Acid," *Journal of The Electrochemical Society*, vol. 162, no. 3, pp. A255–A261, 2015.

[14] Y. Shi, C. Ferone, C. Rao, and C. Rahn, "Nondestructive Forensic Pathology of Lead-Acid Batteries," in *American Control Conference (ACC)*, 2012.

[15] "Advanced Lead-Acid Batteries Will Surpass $18 Billion in Annual Market Value by 2020." [Online]. Available: http://www.navigantresearch.com/newsroom/advanced-lead-acid-batteries-will-surpass-18-billion-in-annual-market-value-by-2020. [Accessed: 14-Apr-2013].

[16] M. F. DeAnda, J. Miller, P. Moseley, and P. Butler, “Reliability of Valve-Regulated Lead-Acid Batteries for Stationary Applications,” 2004.

[17] R. Wagner, “Failure modes of valve-regulated lead/acid batteries in different applications,” *Journal of Power Sources*, vol. 53, no. 1, pp. 153–162, 1995.

[18] R. Kaiser, “Optimized battery-management system to improve storage lifetime in renewable energy systems,” *Journal of Power Sources*, vol. 168, no. 1, pp. 58–65, 2007.

[19] P. T. Moseley, “High rate partial-state-of-charge operation of VRLA batteries,” *Journal of Power Sources*, vol. 127, no. 1, pp. 27–32, 2004.

[20] Y. Shi, C. A. Ferone, and C. D. Rahn, “Identification and remediation of sulfation in lead-acid batteries using cell voltage and pressure sensing,” *Journal of Power Sources*, vol. 221, pp. 177–185, 2013.

[21] A. Andersson, “Battery Lifetime Modelling-Simulation model for improved battery lifetime for renewable based energy systems for rural areas,” *Risø-I-2440, Risø*, 2006.

[22] Z. He, G. Yang, H. Geng, N. Shen, and Z. Wang, “A Battery Modeling Method and Its Verification in Discharge Curves of Lead-Acid Batteries,” in *IEEE Vehicle Power and Propulsion Conference (VPPC)*, 2013, pp. 1–5.

[23] M. Huck, J. Badeda, and D. U. Sauer, “Modeling the crystal distribution of lead-sulfate in lead-acid batteries with 3D spatial resolution,” *Journal of Power Sources*, vol. 279, pp. 351–357, 2015.

[24] A. Pesaran, G. H. Kim, and K. Smith, “Accelerating Battery Design Using Computer-Aided Engineering Tools,” 2011.

[25] M. R. Jongerden and B. R. Haverkort, “Battery Modeling,” 2008.

[26] A. G. Kashkooli, S. Farhad, A. S. Fung, and Z. Chen, “Effect of Convective Mass Transfer on Lead-Acid Battery Performance,” *Electrochimica Acta*, 2013.

[27] M. Cugnet and B. Y. Liaw, “Effect of discharge rate on charging a lead-acid battery simulated by mathematical model,” *Journal of Power Sources*, vol. 196, no. 7, pp. 3414–3419, 2011.

[28] R. C. Harwood, V. S. Manoranjan, and D. B. Edwards, “Lead-Acid Battery Model Under Discharge With a Fast Splitting Method,” *IEEE Transactions on Energy Conversion*, vol. 26, no. 4, pp. 1109–1117, 2011.

[29] U. S. Kim, C. B. Shin, S. M. Chung, S. T. Kim, and B. W. Cho, “Modeling of the capacity loss of a 12V automotive lead-acid battery due to ageing and comparison with measurement data,” *Journal of Power Sources*, vol. 190, no. 1, pp. 184–188, 2009.

[30] J. Gou, A. Lee, and J. Pyko, “Modeling of the cranking and charging processes of conventional valve regulated lead acid (VRLA) batteries in micro-hybrid applications,” *Journal of Power Sources*, vol. 263, pp. 186–194, 2014.

[31] V. Boovaragavan, R. N. Methakar, V. Ramadesigan, and V. R. Subramanian, “A mathematical model of the lead-acid battery to address the effect of corrosion,” *Journal of The Electrochemical Society*, vol. 156, p. A854, 2009.

[32] D. M. Bernardi and M. K. Carpenter, “A Mathematical Model of the Oxygen-Recombination Lead-Acid Cell,” *Journal of The Electrochemical Society*, vol. 142, no. 8, pp. 2631–2642, 1995.

[33] J. Newman and W. Tiedemann, “Simulation of Recombinant Lead-Acid Batteries,” *Journal of the Electrochemical Society*, vol. 144, no. 9, pp. 3081–3091, 1997.

[34] T. Nguyen, R. E. White, and H. Gu, “The Effects of Separator Design on the Discharge Performance of a Starved Lead-Acid Cell,” *Journal of The Electrochemical Society*, vol. 137, no. 10, pp. 2998–3004, 1990.

[35] V. Srinivasan, G. Wang, and C. Wang, “Mathematical modeling of current-interrupt and pulse operation of valve-regulated lead acid cells,” *Journal of The Electrochemical Society*, vol. 150, no. 3, pp. A316–A325, 2003.

[36] W. Gu, C. Wang, and B. Liaw, “Numerical Modeling of Coupled Electrochemical and Transport Processes in Lead-Acid Batteries,” *Journal of the Electrochemical Society*, vol. 144, no. 6, pp. 2053–2061, 1997.

[37] W. Gu, G. Wang, and C. Wang, “Modeling the overcharge process of VRLA batteries,” *Journal of Power Sources*, vol. 108, no. 1, pp. 174–184, 2002.

[38] T. Nguyen and R. White, “A mathematical model of a hermetically sealed lead-acid cell,” *Electrochimica Acta*, vol. 38, no. 7, pp. 935–945, 1993.

[39] J. Landfors, D. Simonsson, and A. Sokirko, “Mathematical modelling of a lead/acid cell with immobilized electrolyte,” *Journal of Power Sources*, vol. 55, no. 2, pp. 217–230, 1995.

[40] K. Siniard, M. Xiao, and S. Y. Choe, “One-dimensional dynamic modeling and validation of maintenance-free lead-acid batteries emphasizing temperature effects,” *Journal of Power Sources*, vol. 195, no. 20, pp. 7102–7114, 2010.

[41] D. M. Bernardi, R. Y. Ying, and P. Watson, “Study of charge kinetics in valve-regulated lead-acid cells,” *Journal of The Electrochemical Society*, vol. 151, no. 1, pp. A85–A100, 2004.

[42] E. Karden, P. Mauracher, and F. Schöpe, “Electrochemical modelling of lead/acid batteries under operating conditions of electric vehicles,” *Journal of Power Sources*, vol. 64, no. 1, pp. 175–180, 1997.

[43] A. Tenno, R. Tenno, and T. Suntio, “Evaluation of VRLA battery under overcharging: model for battery testing,” *Journal of Power Sources*, vol. 111, no. 1, pp. 65–82, 2002.

[44] R. L. Cantrell, D. B. Edwards, and P. S. Gill, “Predicting lead-acid battery electrode performance using finite difference equations,” *Journal of Power Sources*, vol. 73, no. 2, pp. 204–215, 1998.

[45] D. Rand, P. Moseley, J. Garche, and C. Parker, *Valve-regulated Lead-Acid Batteries*. Elsevier, 2004.

[46] M. G. Cugnet, M. Dubarry, and B. Y. Liaw, “Peukert’s Law of a Lead-Acid Battery Simulated by a Mathematical Model,” *ECS Transactions*, vol. 25, no. 35, pp. 223–233, 2010.

[47] K. Divya and J. Østergaard, “Battery energy storage technology for power systems—An overview,” *Electric Power Systems Research*, vol. 79, no. 4, pp. 511–520, 2009.

[48] H. J. Bergveld, W. S. Kruijt, and P. H. L. Notten, *Battery Management Systems: Design by Modelling*. Philips Research/Springer Netherlands, 2002.

[49] H. Bindner, T. Cronin, P. Lundsager, J. F. Manwell, U. Abdulwahid, and I. Baring-Gould, "Lifetime Modelling of Lead Acid Batteries," 2005.

[50] D. Linden and T. B. Reddy, *Handbook of Batteries*. McGraw-Hill, 1995.

[51] J. C. Kotz, P. Treichel, and P. A. Harman, *Chemistry and Chemical Reactivity*. Thomson-Brooks/Cole, 2003.

[52] J. Newman and K. E. Thomas-Alyea, *Electrochemical Systems*. John Wiley & Sons, 2004.

[53] M. Cugnet, J. Sabatier, S. Laruelle, S. Grugeon, B. Sahut, A. Oustaloup, and J. M. Tarascon, "On lead-acid-battery resistance and cranking-capability estimation," *IEEE Transactions on Industrial Electronics*, vol. 57, no. 3, pp. 909–917, 2010.

[54] K. Brik and F. ben Ammar, "Causal tree analysis of depth degradation of the lead acid battery," *Journal of Power Sources*, 2012.

[55] V. Svoboda, H. Wenzl, R. Kaiser, A. Jossen, I. Baring-Gould, J. Manwell, P. Lundsager, H. Bindner, T. Cronin, P. Nørgård, and others, "Operating conditions of batteries in off-grid renewable energy systems," *Solar Energy*, vol. 81, no. 11, pp. 1409–1425, 2007.

[56] A. Kirchev, M. Perrin, E. Lemaire, F. Karoui, and F. Mattera, "Studies of the pulse charge of lead-acid batteries for PV applications: Part I. Factors influencing the mechanism of the pulse charge of the positive plate," *Journal of Power Sources*, vol. 177, no. 1, pp. 217–225, 2008.

[57] M. Thele, E. Karden, E. Surewaard, and D. Sauer, "Impedance-based overcharging and gassing model for VRLA/AGM batteries," *Journal of Power Sources*, vol. 158, no. 2, pp. 953–963, 2006.

[58] W. Waag and D. Sauer, "State-of-Charge/Health," in *Encyclopedia of Electrochemical Power Sources*, Elsevier, 2009, pp. 793–804.

[59] V. Pop, H. J. Bergveld, D. Danilov, P. P. Regtien, and P. H. Notten, *Battery Management Systems: Accurate State-of-Charge Indication for Battery-Powered Applications*. Springer Verlag, 2008.

[60] W. Gu and C. Wang, "Thermal-Electrochemical Modeling of Battery Systems," *Journal of The Electrochemical Society*, vol. 147, no. 8, pp. 2910–2922, 2000.

[61] M. G. Cugnet, J. Sabatier, S. Laruelle, S. Grugeon, I. Chanteur, B. Sahut, A. Oustaloup, and J.-M. Tarascon, "A solution for lead-acid battery global state estimation," *ECS Transactions*, vol. 19, no. 25, pp. 77–88, 2009.

[62] S. Wang, J. Wang, L. Vu, J. Purewal, S. Soukiazian, and J. Graetz, "On Line Battery Capacity Estimation Based on Half-Cell Open Circuit Voltages," *Journal of The Electrochemical Society*, vol. 161, no. 12, pp. A1788–A1793, 2014.

[63] M. Cugnet, S. Laruelle, S. Grugeon, B. Sahut, J. Sabatier, J.-M. Tarascon, and A. Oustaloup, "A Mathematical Model for the Simulation of New and Aged Automotive Lead-Acid Batteries," *Journal of The Electrochemical Society*, vol. 156, no. 12, pp. A974–A985, 2009.

[64] J. H. Aylor, A. Thieme, and B. Johnson, “A battery state-of-charge indicator for electric wheelchairs,” *IEEE Transactions on Industrial Electronics*, vol. 39, no. 5, pp. 398–409, 1992.

[65] M. Ecker, T. K. D. Tran, P. Dechent, S. Käbitz, A. Warnecke, and D. U. Sauer, “Parameterization of a Physico-Chemical Model of a Lithium-Ion Battery I. Determination of Parameters,” *Journal of The Electrochemical Society*, vol. 162, no. 9, pp. A1836–A1848, 2015.

[66] D. U. Sauer and H. Wenzl, “Comparison of different approaches for lifetime prediction of electrochemical systems-Using lead-acid batteries as example,” *Journal of Power Sources*, vol. 176, no. 2, pp. 534–546, 2008.

[67] C. Hanley, G. Peek, J. Boyes, G. Klise, J. Stein, D. Ton, and T. Duong, “Technology Development Needs for Integrated Grid-Connected PV Systems and Electric Energy Storage,” in *34th IEEE Photovoltaic Specialists Conference (PVSC)*, 2009, pp. 1832–1837.

[68] C. Wang and V. Srinivasan, “Computational battery dynamics (CBD)—electrochemical/thermal coupled modeling and multi-scale modeling,” *Journal of Power Sources*, vol. 110, no. 2, pp. 364–376, 2002.

[69] T. Kim, “A Hybrid Battery Model Capable of Capturing Dynamic Circuit Characteristics and Nonlinear Capacity Effects,” 2012.

[70] A. Aron, G. Girban, and S. Kilyeni, “A geometric approach of a battery mathematical model for on-line energy monitoring,” in *IEEE International Conference on Computer as a Tool (EUROCON)*, 2011, pp. 1–4.

[71] H. Gu, T. Nguyen, and R. E. White, “A Mathematical Model of a Lead-Acid Cell: Discharge, Rest, and Charge,” *Journal of the Electrochemical Society*, vol. 134, no. 12, pp. 2953–2960, 1987.

[72] E. C. Dimpault-Darcy, T. Nguyen, and R. E. White, “A Two-Dimensional Mathematical Model of a Porous Lead Dioxide Electrode in a Lead-Acid Cell,” *Journal of the Electrochemical Society*, vol. 135, no. 2, pp. 278–285, 1988.

[73] C. Lefrou, P. Fabry, and J. C. Poignet, *Electrochemistry: The Basics, with Examples*. Springer Berlin Heidelberg, 2012.

[74] D. Menshykau, “Computational electrochemistry,” 2010.

[75] A. J. Bard and L. R. Faulkner, *Electrochemical Methods: Fundamentals and Applications*. New York: John Wiley & Sons, Inc., 2001.

[76] C. Wang, W. Gu, and B. Liaw, “Micro-Macroscopic Coupled Modeling of Batteries and Fuel Cells I. Model Development,” *Journal of the Electrochemical Society*, vol. 145, no. 10, pp. 3407–3417, 1998.

[77] A. Tenno, R. Tenno, and T. Suntio, “Charge-discharge behaviour of VRLA batteries: model calibration and application for state estimation and failure detection,” *Journal of Power Sources*, vol. 103, no. 1, pp. 42–53, 2001.

[78] J. E. Mueller, D. Fantauzzi, and T. Jacob, “Multiscale Modeling of Electrochemical Systems,” *Electrocatalysis*, vol. 14, pp. 1–74, 2013.

[79] J. Koryta, J. Dvorak, and L. Kavan, *Principles of electrochemistry*. Wiley Chichester, 1993.

[80] J. Newman and W. Tiedemann, "Porous-Electrode Theory with Battery Applications," *AIChE Journal*, vol. 21, no. 1, pp. 25–41, 1975.

[81] L. Onsager, "Theories of Concentrated Electrolytes," *Chemical Reviews*, vol. 13, no. 1, pp. 73–89, 1933.

[82] S. Whitaker, "Advances in theory of fluid motion in porous media," *Industrial & Engineering Chemistry*, vol. 61, no. 12, pp. 14–28, 1969.

[83] V. Esfahanian, A. B. Ansari, and F. Torabi, "Simulation of lead-acid battery using model order reduction," *Journal of Power Sources*, vol. 279, pp. 294–305, 2015.

[84] M. Ecker, S. Käbitz, I. Laresgoiti, and D. U. Sauer, "Parameterization of a Physico-Chemical Model of a Lithium-Ion Battery II. Model Validation," *Journal of The Electrochemical Society*, vol. 162, no. 9, pp. A1849–A1857, 2015.

[85] U. Teutsch, "A Mathematical Model for Float Operation of Valve-Regulated Lead-Acid Batteries," in *1st IEEE International Telecommunications Energy Special Conference (TELESCON)*, 1994, pp. 89–96.

[86] B. Iooss and P. Lemaître, "A review on global sensitivity analysis methods," *Uncertainty Management in Simulation-Optimization of Complex Systems: Algorithms and Applications*, pp. 101–122, 2015.

[87] A. Saltelli, S. Tarantola, F. Campolongo, and M. Ratto, *Sensitivity analysis in practice: a guide to assessing scientific models*. John Wiley & Sons, 2004.

[88] F. Campolongo, J. Cariboni, and A. Saltelli, "An effective screening design for sensitivity analysis of large models," *Environmental modelling & software*, vol. 22, no. 10, pp. 1509–1518, 2007.

[89] A. Saltelli, M. Ratto, T. Andres, F. Campolongo, J. Cariboni, D. Gatelli, M. Saisana, and S. Tarantola, *Global sensitivity analysis: the primer*. John Wiley & Sons, 2008.

[90] I. M. Sobol, "Global sensitivity indices for nonlinear mathematical models and their Monte Carlo estimates," *Mathematics and computers in simulation*, vol. 55, no. 1, pp. 271–280, 2001.

[91] M. J. Jansen, "Analysis of variance designs for model output," *Computer Physics Communications*, vol. 117, no. 1, pp. 35–43, 1999.

[92] T. V. Nguyen, "Modeling and characterization of a lead-acid cell," 1988.

[93] L. Albright, *Albright's chemical engineering handbook*. CRC Press, 2008.

[94] R. B. Bird, W. E. Stewart, and E. N. Lightfoot, *Transport Phenomena*. Wiley, 2007.

[95] H. Bode, *Lead-Acid Batteries*. John Wiley & Sons, New York, 1977.

[96] "IEEE Recommended Practice for Maintenance, Testing, and Replacement of Valve-Regulated Lead-Acid (VRLA) Batteries for Stationary Applications," 2006.

[97] H. J. Bergveld, "Battery Management Systems: Design by Modelling," 2002.

[98] A. Delaille, M. Perrin, F. Huet, and L. Hernout, “Study of the ‘coup de fouet’ of lead-acid cells as a function of their state-of-charge and state-of-health,” *Journal of Power Sources*, vol. 158, no. 2, pp. 1019–1028, 2006.

[99] V. Pop, H. J. Bergveld, P. Notten, and P. P. Regtien, “State-of-the-art of battery state-of-charge determination,” *Measurement Science and Technology*, vol. 16, no. 12, p. R93, 2005.

[100] V. Pop, H. Bergveld, J. O. het Veld, P. Regtien, D. Danilov, and P. Notten, “Modeling battery behavior for accurate state-of-charge indication,” *Journal of The Electrochemical Society*, vol. 153, no. 11, pp. A2013–A2022, 2006.

[101] H. S. Harned and W. J. Hamer, “The Thermodynamics of Aqueous Sulfuric Acid Solutions from Electromotive Force Measurements,” *Journal of the American Chemical Society*, vol. 57, no. 1, pp. 27–33, 1935.

[102] H. S. Harned and W. J. Hamer, “The Molal Electrode Potentials and the Reversible Electromotive Forces of the Lead Accumulator from 0 to 60° Centigrade,” *Journal of the American Chemical Society*, vol. 57, no. 1, pp. 33–35, 1935.

[103] B. Pattipati, B. Balasingam, G. Avvari, K. Pattipati, and Y. Bar-Shalom, “Open circuit voltage characterization of lithium-ion batteries,” *Journal of Power Sources*, vol. 269, pp. 317–333, 2014.

[104] M. K. Carpenter, D. M. Bernardi, and J. A. Wertz, “The use of Hg/Hg2SO4 reference electrodes in valve-regulated lead/acid cells,” *Journal of Power Sources*, vol. 63, no. 1, pp. 15–22, 1996.

[105] A. I. Harrison, “The characteristics evolving from various VRLA battery designs,” in *17th IEEE International Telecommunications Energy Conference (INTELEC)*, 1995, pp. 346–352.

[106] U. B. Thomas, “The Electrical Conductivity of Lead Dioxide,” *Journal of The Electrochemical Society*, vol. 94, no. 2, pp. 42–49, 1948.

[107] D. C. Montgomery, G. C. Runger, and N. F. Hubele, *Engineering Statistics*, 5th ed. John Wiley & Sons, Incorporated, 2010.

[108] A. Saltelli, P. Annoni, I. Azzini, F. Campolongo, M. Ratto, and S. Tarantola, “Variance based sensitivity analysis of model output. Design and estimator for the total sensitivity index,” *Computer Physics Communications*, vol. 181, no. 2, pp. 259–270, 2010.

[109] S. C. Chapra and R. P. Canale, *Numerical Methods for Engineers*, 2nd ed. McGraw-Hill, 2012.

[110] T. Weise, *Global Optimization Algorithms - Theory and Application*. Self-Published, 2009.

[111] L. G. Birta and G. Arbez, *Modelling and Simulation: Exploring Dynamic System Behaviour*. Springer, 2007.

[112] A. R. Conn, K. Scheinberg, and L. N. Vicente, *Introduction to Derivative-Free Optimization*. SIAM, 2009.

[113] H. Budde-Meiwes, D. Schulte, J. Kowal, D. U. Sauer, R. Hecke, and E. Karden, “Dynamic charge acceptance of lead-acid batteries: Comparison of methods for conditioning and testing,” *Journal of Power Sources*, vol. 207, pp. 30–36, 2012.

[114] P. T. Moseley, D. A. Rand, and B. Monahov, “Designing lead-acid batteries to meet energy and power requirements of future automobiles,” *Journal of Power Sources*, vol. 219, pp. 75–79, 2012.

[115] Y. Zhang, H. Wang, L. Wang, and X. Zhao, “A method to extend fast charging lead-acid battery cycle life for electric vehicles,” in *Advances in Energy, Environment and Materials Science: Proceedings of the International Conference on Energy, Environment and Materials Science (EEMS 2015)*, 2016, p. 33.

[116] N. T. Fernandes, R. Demonti, J. de Andrade, P. F. de Melo, C. G. Bianchin, G. Pretko, A. R. Lemos, and others, “Control strategy for pulsed lead acid battery charger for stand alone photovoltaics,” in *13th IEEE Brazilian Power Electronics Conference and 1st Southern Power Electronics Conference (COBEP/SPEC)*, 2015, pp. 1–6.

[117] M. Perrin and A. Delaille, “Coup de Fouet,” in *Encyclopedia of Electrochemical Power Sources*, Elsevier, 2009, pp. 779–792.

[118] L. Lam, N. Haigh, C. Phyland, and A. Urban, “Failure mode of valve-regulated lead-acid batteries under high-rate partial-state-of-charge operation,” *Journal of Power Sources*, vol. 133, no. 1, pp. 126–134, 2004.

[119] M. Cugnet, M. Dubarry, and B. Liaw, “Encyclopedia of Electrochemical Power Sources,” Newnes, 2009, pp. 816–828.

[120] A. Jossen, J. Garche, and D. U. Sauer, “Operation conditions of batteries in PV applications,” *Solar Energy*, vol. 76, no. 6, pp. 759–769, 2004.

[121] H. Huang and T. V. Nguyen, “A Two-Dimensional Transient Thermal Model for Valve-Regulated Lead-Acid Batteries under Overcharge,” *Journal of The Electrochemical Society*, vol. 144, no. 6, pp. 2062–2068, 1997.